# OPTIMAL DEPLOYMENT OF ENERGY STORAGE TECHNOLOGIES FOR GRID SERVICE PROVISION AND MICROGRID FORMATION

YAHIA AHMED

A THESIS SUBMITTED TO THE FACULTY OF GRADUATE STUDIES IN PARTIAL FULFILLMENT OF THE REQUIREMENTS FOR THE DEGREE OF MASTER OF APPLIED SCIENCE

GRADUATE PROGRAM IN
ELECTRICAL ENGINEERING AND COMPUTER SCIENCE
YORK UNIVERSITY
TORONTO, ONTARIO

APRIL 2026

# Abstract

The global transition towards deep decarbonization and the widespread integration of renewable energy resources introduce unprecedented operational complexities within modern power systems. Managing these dynamics necessitates massive flexibility across both transmission and distribution networks, which can be achieved through Energy Storage (ES) and decentralized microgrid architectures. Despite the rapid advancement of these technologies, significant barriers remain in their effective integration into the power grid, including the complex modeling of emerging technologies, stringent market regulations, and the lack of electrically informed decentralization strategies.

This thesis presents comprehensive and novel optimization frameworks to address these critical gaps in the deployment of ES technologies for Grid Services (GSs) provision and the optimal formulation of sustainable microgrids. At the transmission level, a holistic techno-economic framework is proposed for the optimal sizing and multi-horizon scheduling of grid-connected Advanced Adiabatic Compressed Air Energy Storage (AA-CAES). By incorporating detailed thermodynamic constraints and diverse electricity pricing schemes, the model assesses AA-CAES participation across Energy Arbitrage (EA), Operating Reserve (OR), and Capacity Markets Demand Response (CMDR). Results indicate that while AA-CAES is economically viable for EA and OR primarily in high-variability markets, it remains highly profitable for CMDR across both stable and variable pricing markets.

At the consumer level, the research develops an optimal energy resource sizing and management framework for Large Energy Facilitys (LEFs) participating in CMDR. To overcome the severe computational complexities introduced by dynamic baseline evaluation rules, a novel convex relaxation of CMDR constraints is introduced. This approach reduces computation time from several hours to fractions of a second while ensuring global optimality with an optimality gap below 0.1%. The framework further demonstrates that aggregating short-duration (e.g., Battery Energy Storage (BES)) and long-duration (e.g., Hydrogen Energy Storage (HES) and

Compressed Air Energy Storage (CAES)) technologies maximizes cost savings and environmental sustainability through enhanced arbitrage, emissions-cutting peak-demand reduction, and sustained capacity market obligations.

At the distribution network level, a tri-stage optimization framework is designed to systematically decentralize Power Distribution Systems (PDSs) into self-sustaining microgrids. This framework introduces a hierarchical agglomerative clustering method based on electrical line impedance, followed by the stochastic planning of Distributed Energy Resources (DERs). A subsequent allocation strategy optimally places active and reactive power resources, significantly enhancing voltage regulation and reducing system losses under both islanded and cooperative operational modes.

These proposed frameworks provide robust, computationally tractable solutions to maximize the economic and operational benefits of ES and decentralized microgrids in modern power systems.

# Acknowledgements

First and foremost, I would like to sincerely thank my supervisor, Prof. Dr. Hany E. Z. Farag. About two years of continuous work with Prof. Dr. Hany E. Z. Farag has been a great and rewarding experience. I gained valuable insights into this field through him. He patiently directed my research and enlightened me with valuable advice and guidance, making this work possible.

I would like to express my gratitude to my committee members, Prof. Dr. John Lam and Prof. Dr. Mark Winfield, for their great feedback and valuable comments on this thesis.

I would also like to thank my colleagues Ahmed Elsayed and Abdallah El-Hamalawy, who patiently shared their experience and knowledge of tools with me, making this research possible. I am also grateful to my colleagues Ahmed Masry and Abdullah Tauqeer for their help and support throughout this journey. Furthermore, I want to thank Sebastian John Marmorato, the founder of the York University Run Club; I wish I could have had a similar club during my undergraduate studies.

Finally, I want to express my deepest gratitude to my parents and my family members, Ahmed and Mawada, for always providing me with continuous encouragement and motivation throughout the years and during the process of researching and writing this thesis.

# Table of Contents

# List of Tables

# List of Figures

# Acronyms

**AA-CAES** Advanced Adiabatic Compressed Air Energy Storage. ii, 2, 3, 5, 6, 9–13, 22, 23, 26–39, 41–49, 96, 97, 99

**AF** Adjustment Factor. 51, 53, 66

**BES** Battery Energy Storage. ii, 2, 4, 8, 10, 15–17, 19, 22, 52, 54, 56, 60, 62, 63, 67–73, 78–81, 83, 86, 89, 91, 92, 94, 98, 100

**C&I** Commercial and Industrial. 4, 13

**CAES** Compressed Air Energy Storage. iii, 2–4, 6, 8–12, 16, 50, 51, 53, 54, 56, 60, 63, 67–73, 98, 100

**CapEx** Capital Expenditure. 12, 26, 34, 41, 42, 44–48, 51, 60, 67, 70, 78, 81, 82, 97

**CHP** Combined Heat and Power. 4, 51, 53, 55, 56, 60, 61, 65, 66, 68, 71, 72

**CMDR** Capacity Markets Demand Response. ii, 2–4, 6, 12–16, 22–28, 31–34, 37, 41, 44–48, 54–57, 60, 61, 65–73, 96–100

**CMP** Capacity Market Participation. 6

**DER** Distributed Energy Resource. iii, 1–5, 7, 17, 18, 22, 23, 74–78, 80, 81, 83, 84, 92–95, 97, 98

**DR** Demand Response. 6, 13–16, 22, 50–52, 54, 55, 57–61, 65–73, 98

**DRP** Demand Response Program. 4, 6, 13–16, 23

**EA** Energy Arbitrage. ii, 2, 4, 6, 11–13, 16, 27–29, 31, 34, 41–48, 55, 57, 65, 68–72, 96–98, 100

**ES** Energy Storage. ii, iii, 1–8, 11, 16–18, 22, 23, 43, 55–57, 60, 61, 65, 67, 68, 70, 73, 74, 77, 78, 96, 97, 99, 100

**EV** Electric Vehicle. 17, 19

**GHG** Greenhouse Gas. 1, 5, 16–18, 52, 55, 60, 61, 65, 67–74

**GS** Grid Service. ii, 2, 3, 5, 6, 11–13, 23, 27–29, 39, 41, 48, 49, 99, 100

**HEP** Hourly Electricity Price. 57, 65, 71, 72

**HES** Hydrogen Energy Storage. ii, 2, 4, 8, 10, 16, 52, 54, 56, 60, 63, 67–71, 73, 98, 100

**HX** Heat Exchanger. 25, 26, 29, 54, 63, 64

**IESO** Independent Electricity System Operator. 13, 15, 40, 58

**LEF** Large Energy Facility. ii, 4, 6, 13, 16, 17, 23, 51, 53, 55–57, 60, 61, 65, 73, 96, 97, 99, 100

**LP** Linear Programming. 19

**MINLP** Mixed Integer Non-linear Programming. 18

**NYISO** New York Independent System Operator. 13, 15

**OpEx** Operational Expenditure. 12, 26, 34, 41, 42, 44–48, 51, 60, 61, 78, 82

**OR** Operating Reserve. ii, 2, 3, 6, 11–13, 22, 24, 26–28, 31, 34, 37, 41, 43, 44, 47, 48, 96, 97, 100

**PCS** Power Conversion Systems. 57, 60, 62, 68, 71, 78–81, 83, 92, 94

**PDS** Power Distribution System. iii, 5, 7, 17–23, 75–78, 81, 82, 84, 92–94, 97–99

**PHS** Pumped Hydro Storage. 2, 8–10

**PSO** Power System Operator. 11, 15, 32, 58

**PV** Photovoltaic. 14, 17, 52, 54–57, 60–62, 67, 70–73, 77–81, 83, 86, 89, 91–94, 98

**SoC** State-of-Charge. 62, 63, 71, 78, 80, 83, 89, 90

**TES** Thermal Energy Storage. 10, 29, 30, 63

**V2G** Vehicle-to-Grid. 19

**VPP** Virtual Power Plant. 13–15

# Chapter 1

# Introduction

## 1.1 Motivation

The global energy sector is currently undergoing a profound structural transformation driven by the intersecting imperatives of deep decarbonization, energy security, and rapid technological advancement. Global electricity demand is experiencing accelerated growth propelled by the widespread electrification of end use sectors [1]. Concurrently, to meet this rising demand while mitigating Greenhouse Gas (GHG) emissions, the exponential deployment of DER and large scale renewable generation is breaking historical records [2].

While the displacement of fossil fuel generation is vital for climate goals, it introduces unprecedented operational complexities. Unlike traditional thermal power plants, solar and wind resources are highly stochastic. This intermittency fundamentally alters the power grid net load profile [3]. The growing misalignment between peak generation and peak demand has led to severe net load variability, creating steep ramping requirements [4]. Consequently, modern power systems require massive amounts of operational flexibility to reliably and rapidly balance supply and demand under high uncertainty [3]. As conventional baseload generation retires, ES is increasingly required as the paramount flexibility resource to absorb surplus generation, provide dispatchable power, and support reliable system operation across all levels of the grid [5].

Energy storage plays a critical multidimensional role at both transmission and distribution levels of modern power systems [5]. Unlike traditional generation, ES systems are entirely bidirectional, allowing them to act as dispatchable loads during periods of overgeneration and as dispatchable generators during supply deficits [5]. At the transmission level, ES supports bulk system wide operations by providing a suite of wholesale GSs. The primary mechanisms through which ES provides value include EA by time shifting energy, charging during low cost off peak hours and discharging during high priced peak hours. Furthermore, fast responding ES excels in providing crucial ancillary services, such as OR, which are necessary to arrest frequency deviations in low inertia grids [6]. Additionally, ES participates in CMDR, where resources are financially compensated for committing to be available to deliver firm power during stressed grid conditions [7]. At the distribution level, the proliferation of DERs and localized electrification has transformed networks into active bidirectional power exchanges, where ES helps balance local generation and demand, significantly mitigating grid congestion and reducing the need for costly infrastructure upgrades [8], [9].

Widely studied ES technologies include Pumped Hydro Storage (PHS), BES, HES, and CAES. These technologies differ significantly in their duration capability, energy and power ratings, scalability, and deployment constraints. Although BES has demonstrated immense maturity and dominates the short duration market due to its high round trip efficiency and modularity, it is generally more suitable for small capacity applications as well as short duration high power services due to prohibitive capital costs at extended durations. HES offers exceptional long duration and seasonal storage capabilities but suffers from profound thermodynamic conversion losses, yielding a low round trip efficiency [10]. While PHS is the most widely deployed large scale storage technology globally, its applicability is severely limited by geographic and topological constraints [11]. For long duration applications at the transmission level, CAES offers one of the lowest installed energy capacity costs among grid scale storage technologies [12]. To overcome the emission issues of conventional diabatic CAES, AA-CAES has attracted increasing attention. AA-CAES captures the heat generated during the air compression phase. This heat is subsequently used to preheat the air during expansion, entirely eliminating fossil fuel combustion. This configuration yields a high energy conversion efficiency, long operational lifetime, flexible configuration, and low environmental impact [13].

Although integrating ES and decentralized microgrids mitigates the operational complexities of modern grids, maximizing their potential requires overcoming specific system integration hurdles. At the transmission level, it is necessary to navigate the complex modelling of emerging technologies (e.g., AA-CAES), the stringent market regulations governing GSs, and the synergistic operation of hybrid storage systems with diverse duration and capacity ratings. At the distribution level, critical questions remain regarding how the network is decentralized, what the required capacity of ES and DERs is to achieve sustainability, and where these resources should be placed. Addressing these challenges motivates a deeper investigation into the limitations of existing research to develop more resilient and economically feasible power systems.

## 1.2 Problem Statement and Research Gaps

Despite the rapid advancement of ES and decentralized grid architectures, significant barriers remain in effectively integrating these technologies into modern transmission and distribution power systems.

As power grids evolve to accommodate massive renewable penetration, alongside increasing electricity demand and its associated uncertainties, AA-CAES has emerged as a highly promising solution for bulk, long duration energy management [12], [13]. While the deployment of CAES technologies for mitigating grid congestion and participating in GSs is widely recognized, current system planning and integration models predominantly focus on conventional systems and fail to incorporate recently developed AA-CAES technologies [14]–[17]. Furthermore, there is a systemic reliance on simplified, linear energy representations that fail to capture the complex thermodynamic realities of the AA-CAES [18]. The nonlinear interdependencies among compressed air temperature, transient pressure dynamics, and mass flow rates directly dictate the performance and efficiency of the turbomachinery [19]. When physical constraints are ignored, sizing and dispatch solutions become technically infeasible or economically suboptimal. Moreover, operational scheduling is often restricted to short term [14]–[21], fundamentally neglecting the inherent long duration and seasonal storage capabilities that give AA-CAES its competitive edge [22], [23]. Compounding these technical oversimplifications is a narrow operational focus [24]; single service provision is frequently evaluated under static pricing schemes, failing to capture the synergistic economic potential of simultaneous participation in GSs (e.g., OR and CMDR) under highly volatile, real time pricing [18]–[21]. Furthermore, the economic viability of these systems heavily depends on the electricity pricing scheme such as fixed rate versus highly variable markets which has not been comprehensively analyzed alongside multi service provision. Consequently, a significant gap remains in developing a holistic, computationally tractable framework that cooptimizes both the physical component sizing and the multi horizon (daily, weekly, and monthly), multi market scheduling of AA-CAES to assess its performance in various GSs.

Beyond bulk transmission storage, immense operational flexibility resides at the consumer level through Demand Response Programs (DRPs) [25]–[28]. Current DRPs can be broadly classified into two main categories: 1) price-based and 2) incentive-based [29]. Price-based DRPs rely on time-varying electricity prices to encourage customers to adjust their consumption behavior. However, their widespread adoption has been limited by the lack of direct dispatch capability, uncertainty associated with real-time pricing that may expose participants to financial losses, and technical challenges related to smart meter deployment [30], [31]. To address these limitations, incentive-based DRPs have emerged as an alternative that improves grid reliability while offering greater operational flexibility and reduced financial risk for participants. In incentive-based DRPs, participants are encouraged to modify their electricity usage through explicit financial incentives or contractual compensation mechanisms. While various incentive-based demand response mechanisms, such as demand bidding [32], [33], load curtailment [34], [35], and direct load control [36], are commonly utilized, CMDR remains the most lucrative and widely adopted framework [29]. However, even though LEFs such as Commercial and Industrial (C&I) facilities contribute the vast majority of this capacity due to their substantial and controllable baseloads [37], optimal facility planning and energy resource sizing for CMDR participation still lack comprehensive analytical integration. The primary barrier lies in the stringent regulatory evaluation procedures utilized by grid operators, which rely on dynamically calculated historical baselines to verify performance [38]–[40]. Accurately embedding these dynamic market rules such as historic load sorting and fractional adjustment factors into energy management models introduces severe mathematical complexities. This transforms the optimization into a highly nonconvex problem that renders real time operational scheduling computationally prohibitive. Consequently, current market participants are exposed to significant financial penalties due to overestimating their committed capacity or failing to incorporate the existing market rules [41]–[43]. A critical need exists for mathematical techniques, such as convex relaxation, to transform these rules into reliable lower bounds that drastically reduce computation times while ensuring global optimality. To mitigate the risk of underperformance penalties and ensure that these strict capacity commitments are reliably met, integrating ES technologies is essential [44]; furthermore, while single ES deployments are frequently utilized, there is a distinct lack of comprehensive frameworks investigating how hybrid combinations of short duration (e.g., BES) and long duration (e.g., HES and CAES) storage can be synergistically managed alongside onsite generation (e.g., DERs and Combined Heat and Power (CHP)) [10], [13], [45]. Such frameworks must satisfy continuous EA opportunities, minimize facility peak demand charges, and sustain capacity market obligations, while concurrently minimizing real time GHG emissions.

At the distribution level, the paradigm is shifting rapidly from centralized, top down control toward decentralized networks of self-sustaining microgrids [46]. While various methodologies exist to size DERs and ES for these localized systems, a fundamental challenge remains in determining how to systematically decompose a large, interconnected PDS into these smaller, sustainable entities. Current decentralization efforts often model microgrids as simplified entities or rely on basic topological clustering methods rather than electrically informed partitioning [47]–[56]. These approaches lack a rigorous foundation in the actual electrical characteristics of the network, such as line impedance, which is vital for enabling effective decentralized control and ensuring long term sustainable operation [57]. Moreover, current planning frameworks frequently isolate the stochastic sizing of DERs from their physical allocation [58]–[61]. Operating interconnected microgrids without a coordinated strategy for the optimal placement of both active DERs and reactive power support devices leads to severe equipment oversizing, suboptimal power sharing, and degraded voltage stability [62]. Additionally, there is a lack of flexible frameworks capable of evaluating these allocations across different operational modes, including fully islanded, cooperative multi microgrid, and grid connected states [63]. Therefore, a critical need exists for a unified, electrically grounded tri stage framework that seamlessly bridges network clustering, resource sizing, and optimal component allocation to achieve true multi microgrid self-sustaining.

## 1.3 Thesis Objectives

Addressing the identified gaps is essential for clarifying the role of ES in supporting reliable and efficient operation across both transmission and distribution systems. The central goal of this research is to enhance the integration of ES technologies within modern power systems. This involves the following specific objectives:

- Accurate modeling of AA-CAES that captures its thermodynamic characteristics while remaining tractable for large scale optimization;
- Accurate modeling of GSs, translating well established capacity market rules and baseline evaluation procedures into complex, yet optimization friendly convex constraints;

- Assessment of AA-CAES techno economic performance in providing GSs, with particular emphasis on long duration ES capability and market dependent operational behavior;
- Study of the synergistic operation of different ES technologies to investigate how differences in storage duration, energy capacity, and power rating enable complementary system operation across hybrid configurations;
- Design of a decentralization approach for distribution systems that supports economically feasible storage sizing and optimal resource allocation for network sustainability.

## 1.4 Thesis Outline

The remainder of this thesis is organized into the following chapters to systematically address the stated objectives:

- **Chapter 2** provides an overview of the evolution and techno-economic viability of prominent grid-scale ES technologies. Building on this foundation, it provides a comprehensive literature review of CAES and AA-CAES modelling, with emphasis on their participation in various GSs and DRPs. It also surveys existing work on DRPs, highlighting the importance of CMDR while outlining the relevant market rules and evaluation requirements. In addition, the chapter reviews decentralization approaches for distribution systems that support economically feasible storage sizing and optimal resource allocation for sustainability. The literature review identifies key gaps and limitations in the existing work and highlights the potential research contributions
- **Chapter 3** presents the optimal deployment framework for AA-CAES in diverse electricity markets. It develops a detailed thermodynamic system model integrated with power grid constraints. The chapter assesses the techno–economic performance of AA-CAES under varying scheduling horizons while providing EA, OR, and Capacity Market Participation (CMP) services.
- **Chapter 4** proposes an optimal energy resource sizing and management framework for LEFs participating in capacity market based Demand Response (DR). It outlines the commercial electricity billing structure, introduces a novel convex relaxation of complex DR capacity market rules, and evaluates the financial and environmental impacts of hybrid ES operation.

- **Chapter 5** presents a tri–stage optimization framework for the optimal clustering of PDSs into self-sustaining microgrids. This includes the formulation of a hierarchical agglomerative clustering algorithm based on electrical distance, the stochastic planning of microgrid DERs, and the subsequent topological allocation of active and reactive power resources to ensure voltage stability.

- **Chapter 6** concludes the thesis by summarizing the primary findings on the optimal deployment of ES and decentralized microgrids across modern power systems. It highlights the core contributions at the transmission, consumer, and distribution levels, , identifies research limitations, and outlines potential avenues for future research.

# Chapter 2

# Literature Survey

## 2.1 The Evolution and Techno-Economic Viability of Grid-Scale Energy Storage Technologies

The transition toward deeply decarbonized power grids strictly demands the deployment of bulk-scale energy storage to mitigate the intermittency of renewable energy sources. Widely studied ES technologies include PHS, BES, HES, and CAES. These technologies differ significantly in their duration capability, energy and power ratings, scalability, and deployment constraints.

BES, predominantly utilizing lithium-ion architectures, has demonstrated immense maturity and dominates the short-duration market due to its high round-trip efficiency, typically between 85% and 90%, and its inherent modularity. However, BES is generally more suitable for small capacity applications and short-duration, high-power services such as frequency regulation. This is due to prohibitive power capital costs, which range from $900 to $4,000 per kilowatt, making extended bulk-duration applications economically unviable [12],[64]. Furthermore, electrochemical systems suffer from unavoidable cycling fatigue and calendar aging, restricting their operational lifespan to approximately 5 to 15 years before requiring costly replacements. To bridge the gap toward inter-seasonal storage, HES offers exceptional long-duration capabilities by completely decoupling power capacity from energy capacity [65]. Despite its theoretical potential to store energy over months without degradation, HES remains largely in the research and early commercialization phase. This delay is primarily due to profound thermodynamic conversion losses during the power-to-gas-to-power cycle, which currently yield a low round-trip efficiency of 25%

to 58%, alongside the need for massive, centralized electrolysis infrastructure [64], [65].

In the absence of cost-effective long-duration batteries and highly efficient hydrogen infrastructure, PHS has historically served as the unchallenged backbone of grid-scale energy storage. PHS operates on the fundamental principle of gravitational potential energy, shifting massive volumes of water between reservoirs at different elevations. It is the most widely deployed large-scale storage technology globally, boasting massive power ratings ranging from 100 MW to 5,000 MW and operational lifespans of 40 to 60 years [66], [67]. Despite these overwhelming advantages, the future expansion of PHS is severely curtailed by rigid geographic and topological constraints. It requires highly specific hydrological conditions, immense localized water availability, and significant natural elevation differentials. The scarcity of unexploited, topographically suitable sites severely limits further global deployment, underscoring the urgent need for location-flexible mechanical storage alternatives for bulk grid-scale applications [66], [67].

For long-duration applications at the transmission level, CAES offers one of the lowest installed energy capacity costs among grid-scale storage technologies. CAES serves as a geographically flexible alternative to PHS by utilizing massive underground geological formations, such as salt caverns or porous aquifers, to achieve economic viability at scale [68]. The core mechanism of CAES involves using surplus electricity during periods of low demand to power compressors that pressurize ambient air, which is then stored in these underground reservoirs. When electricity demand is high, the stored compressed air is released, heated, and expanded through turbines coupled to a generator to produce electricity. The thermodynamic handling of the heat of compression strictly dictates the classification, efficiency, and environmental footprint of these systems. In traditional Diabatic CAES, the intense thermal energy generated during air compression is considered parasitic and is rejected directly to the atmosphere via cooling systems. When the stored air is later extracted for generation, it must be rapidly reheated to prevent turbine freezing and to provide necessary enthalpy. Diabatic CAES achieves this by mixing the expanding air with fossil fuels, predominantly natural gas, in a combustion chamber. This reliance on fossil fuel combustion limits the thermodynamic cycle efficiency to around 40% to 55% and generates greenhouse gas emissions, making it less aligned with modern grid decarbonization goals [68], [69]. Table 2.1 presents a comparative overview of the efficiency, lifespan, and capital costs across prominent energy storage technologies.

To overcome the emission issues of conventional diabatic systems, AA-CAES has attracted increasing attention and represents the contemporary evolutionary leap for mechanical storage.

Table 2.1: Comparison of energy storage technologies.

| **Technology** | **Efficiency (%)** | **Lifespan (Years)** | **Power Capital Cost ($/kW)** | **Typical Discharge Time** |
|---|---|---|---|---|
| BES (Li-ion) | 85-90 | 5-15 | 900-4000 | Minutes to Hours |
| HES | 25-58 | 5-20+ | 500-10000 | Seconds to 24+ Hours |
| PHS | 75-85 | 40-60 | 2000-4300 | 1 to 24+ Hours |
| CAES | 70-89 | 20-40 | 400-1000 | 1 to 24+ Hours |

AA-CAES integrates a sophisticated Thermal Energy Storage (TES) subsystem [70]. It captures the heat generated during the air compression phase and transfers it to a TES medium. This stored heat is subsequently used to preheat the air during expansion, entirely eliminating the need for natural gas combustion. This regenerative configuration yields a high energy conversion efficiency, reliably boosting round-trip efficiency to between 70% and 89%, while ensuring a long operational lifetime of 20 to 40 years [70], [71]. Overall, AA-CAES offers flexible configuration and maintains a low environmental impact.

The theoretical viability of both traditional and advanced CAES is substantiated by a historical track record of diabatic plants and a rapidly accelerating pipeline of next-generation adiabatic mega-projects. The commercial viability of grid-scale CAES was initially established by two pioneering diabatic CAES facilities. Commissioned in 1978 in Germany, the Huntorf Plant operates within salt domes with a generation capacity of 321 MW, but it operates without exhaust heat recuperation. Operational since 1991, the McIntosh Plant in Alabama, USA, possesses a 110 MW generation capacity and includes a recuperator that captures waste heat from the turbine exhaust to preheat incoming air, significantly improving its overall efficiency [68], [72].

Despite the success of these legacy plants, the contemporary global market is increasingly dominated by zero-emission AA-CAES projects. Commissioned in 2019, the Goderich AA-CAES Facility in Ontario, Canada, serves as the world's first commercially contracted AA-CAES plant, successfully proving dynamic responsiveness and commercial viability without emissions. Simultaneously, China's rapid expansion of renewable energy has propelled the commercialization of massive AA-CAES infrastructure [12]. The Jintan CAES Facility in Jiangsu Province represents a landmark 60 MW deployment utilizing a subterranean salt cavern to achieve high efficiency without supplementary fossil fuel firing. Furthermore, the Zhangjiakou 100 MW AA-CAES project in Hebei Province represents one of the world's most extensive operational advanced adiabatic systems, utilizing above-ground air tanks and advanced thermal handling to serve as a global benchmark for emission-free mechanical storage [72].

## 2.2 CAES/AA-CAES Modeling and Participation in GSs

GSs are essential to the operation of modern power grids, safeguarding stability and reliability by balancing generation and demand. In today's competitive electricity markets, Power System Operators (PSOs) are encouraging market participants to provide GSs. ES is widely recognized as a key enabler of these services, providing the dispatchable power required to support the grid. For long-duration grid-scale applications, CAES offers the lowest installed energy capacity cost [12]. Recently, AA-CAES has emerged as the most extensively studied CAES technology, owing to its high energy conversion efficiency, strong reliability, flexible layout, long lifetime, and negligible environmental impact [13]. Demonstrations of 100 MW and 300 MW AA-CAES plants integrated into power grids in Zhangjiakou, China, and Goderich, Canada, highlight their technological maturity and have attracted significant investment [13],[45]. Consequently, techno-economic models assessing AA-CAES participation in GSs are receiving substantial attention, with a steadily increasing number of projects being developed worldwide.

Many efforts have been devoted to studying the economic and reliable participation of CAES/AA-CAES in GSs. In [14], the operation of CAES for congestion relief is presented. The proposed framework exploits electricity price arbitrage opportunities in the day-ahead market while concurrently preparing the CAES to enhance its effectiveness in alleviating congestion. The work in [15] develops a mixed-integer linear programming model to optimize CAES dispatch, enabling it to provide both OR and EA in various U.S. electricity markets. However, these studies [14],[15] employ simplified energy-based CAES models that overlook its thermodynamic characteristics, such as the interdependence among compressed air temperature, pressure, and flow, as well as their effects on the compressor and turbine charging and discharging behaviors. In [16], the authors aim to maximize the CAES profit by optimizing its operation across EA, OR, and regulation GSs, while accounting for the air compression and expansion constraints. The work in [17] formulates a bi-level program, where the outer level determines the optimal sizing and the inner level determines the optimal dispatch of CAES, underscoring the importance of integrating the optimal sizing with the optimal dispatch. Yet, the studies in [14]–[17] focus on the sizing and operational optimization of conventional CAES systems and do not assess the economic feasibility of the recently developed AA-CAES technology.

The study in [18] proposes a self-scheduling approach for AA-CAES participation in energy and reactive power markets, aiming to maximize the expected net income while accounting for air flow compression and expansion constraints. The authors in [19] incorporate an AA-CAES system to minimize operational costs and wind curtailment within an integrated electricity and heating system, employing a detailed AA-CAES model. However, the studies in [18], [19] focus solely on the optimal operation of AA-CAES and, therefore, its Operational Expenditure (OpEx), without considering the optimization of system sizing or the associated investment costs, i.e., Capital Expenditure (CapEx). It is reported in [24] that AA-CAES CapEx can account for up to 25% of total system expenditures. Consequently, conclusions regarding profitability or cost-effectiveness based solely on optimizing the AA-CAES operation may be misleading or overly optimistic.

In contrast to relying on predefined sizes and focusing only on OpEx, as in [18],[19], the study in [20] investigates the optimal sizing of AA-CAES to maximize profits from EA, employing a detailed model that accounts for air flow dynamics. The authors conclude that electricity prices are the primary determinant of profitability, motivating further investigation into how participation in GSs under varying market conditions influences sizing decisions. The work in [21] develops a computationally feasible high-fidelity AA-CAES model to minimize wind curtailment, while incorporating grid integration requirements into the optimization problem.

However, the studies in [18]–[21] do not evaluate the economic feasibility of grid-connected AA-CAES systems utilizing CMDR and OR to provide GSs. Further, since electricity price has been identified as one of the primary determinants of AA-CAES profitability [20], it is essential to revisit the optimal sizing and scheduling of AA-CAES systems under different electricity pricing schemes (i.e., fixed, low hourly variability, and high hourly variability pricing schemes). Additionally, all the studies in [14]–[21] have a common shortfall in terms of their reliance on relatively short scheduling horizons, which may not align with the long- or seasonal-term operational characteristics of CAES and AA-CAES systems. For instance, the studies in [14], [15], [20] consider a daily scheduling horizon, while [16] extends the analysis to a weekly horizon. Yet, as reported in [22], [23], the compressed air storage type and configuration largely determine the capability of CAES and AA-CAES systems to function as long-duration or even seasonal storage, with potential discharge durations of up to two months. Therefore, the relatively short horizons used in previous works limit the exploration of the whole decision space associated with AA-CAES optimal sizing and scheduling.

Based on the above discussions, existing techno-economic studies on AA-CAES exhibit critical limitations that hinder their real-world applicability. First, most of these studies focus on short-term horizons, overlooking long-term and seasonal operational dynamics, which significantly affect profitability. Second, prior studies fail to consider multi-service participation, limiting analysis to EA while ignoring valuable roles in OR and CMDR. Third, models introduced in these studies assume simplified or fixed electricity pricing, failing to capture diverse structures such as real-time market pricing, which drive optimal decisions. Fourth, sizing and scheduling are often treated independently, neglecting their interdependence, leading to technically feasible but economically suboptimal solutions. Finally, existing works lack detailed yet computationally efficient thermodynamic modeling that captures the interdependence among compressed air temperature, pressure, and flow dynamics while accounting for power grid constraints. To address these gaps, Chapter 3 of this thesis proposes a holistic optimization framework for AA-CAES, jointly determining sizing and scheduling to maximize net revenue across energy and GSs markets under realistic market pricing and extended horizons.

## 2.3 LEFs Participation in DRPs, with a Focus on Capacity Markets: Rules and Evaluation Requirements

DR has changed how supply and demand are balanced by shifting some of the power system's operational flexibility from generation to demand. By encouraging customers to adjust their electricity usage, DRPs improve supply–demand coordination, enhance energy efficiency, and contribute to emissions reduction [25]. For example, in 2024, the New York Independent System Operator (NYISO) secured 1,490 MW of peak capacity through DRPs [26]. Similarly, in 2025, the Ontario Independent Electricity System Operator (IESO) obtained 3,022 MW from these programs [27], [28]. While DRPs are implemented across different scales (e.g., residential units and workplaces), LEFs, which aggregate resources such as C&I facilities, microgrids, and Virtual Power Plants (VPPs), are often the most suitable participants. These facilities contribute more than 70% of the total DRPs capacity due to their substantial energy consumption and centralized operational structure, which enable significant and reliable demand reductions [37]. However, their participation potential hings on compliance with existing electricity market rules, since failure to meet these requirements can result in substantial penalties [41]. Consequently, effective DR implementation requires that these DR participants be planned and managed in strict alignment with regulatory constraints to maximize economic returns and reduce $CO_2$

emissions during grid peak hours, highlighting the need for accurate design and management frameworks that explicitly account for market rules and regulations.

Current DRPs can be broadly classified into two main categories: 1) price-based and 2) incentive-based [29]. Price-based DRPs rely on time-varying electricity prices to encourage customers to adjust their consumption behavior. However, their widespread adoption has been limited by the lack of direct dispatch capability, uncertainty associated with real-time pricing that may expose participants to financial losses, and technical challenges related to smart meter deployment [30], [31]. To address these limitations, incentive-based DRPs have emerged as an alternative that improves grid reliability while offering greater operational flexibility and reduced financial risk for participants. In incentive-based DRPs, participants are encouraged to modify their electricity usage through explicit financial incentives or contractual compensation mechanisms.

Previous studies have explored several forms of incentive-based DRPs, including demand bidding [32],[33], load curtailment [34],[35], direct load control [36], and participation in CMDR [73]. In demand bidding mechanisms, participants submit bids representing either surplus energy or energy shortfalls to be balanced by other market participants. In this context, the study in [32] presents a bi-level framework for a price-maker VPP aimed at mitigating discrepancies between the day-ahead and real-time markets. By acquiring external DR through demand bidding, the VPP reduces excess energy settled in the real-time market and increases its expected profit. Similarly, the authors in [33] proposed a VPP operational strategy that employs demand bidding to compensate for Photovoltaic (PV) forecasting errors using a mixed-integer linear programming scheduling framework. Their findings indicate that bidding surplus or deficient PV energy effectively reduces forecasting deviations and enhances profitability in the day-ahead market.

Another incentive-based approach is load curtailment, which provides financial incentives for participants to reduce their electricity demand during peak periods. In this context, the work in [34] proposed a hybrid dynamic incentive strategy for microgrid energy management using the pelican optimization algorithm, where incentives are adjusted in real time based on peak-hour conditions to encourage greater demand reduction, rather than relying on fixed-curtailment fixed-price schedules. In parallel, the study in [35] developed a theoretic contract DR mechanism in which the grid operator designs rewards and penalties based on participant demand reduction levels to promote truthful reporting under incomplete information about users' consumption behavior. To enhance scalability, a convex relaxation was introduced, enabling the operator to derive profit-maximizing contracts that satisfy both incentive compatibility and individual rationality. To move beyond purely incentive-based encouragement mechanisms, direct control approaches allow the PSO to directly modify load patterns during peak hours in exchange for predefined incentives. This approach provides greater reliability to the grid by reducing uncertainty associated with participants' voluntary responses and behavioral intentions. In this regard, the work in [36] proposed a model-free, data-driven resource planning framework for a VPP that jointly optimizes BES sizing and the selection of customers for a thermal load control program. By integrating the dynamic energy management of BES with customer load flexibility, the proposed approach improves VPP operational flexibility and increases profitability in both the day-ahead and real-time electricity markets.

Although demand bidding, load curtailment, and direct load control have received significant attention from both academia and power utilities, CMDR participation contributes the most to DRPs [29]. For example, in 2024, CMDR participation accounted for over 97% of NYISO's total MW-DR capacity, while in Ontario it represented more than 70% in 2025. Under this mechanism, participants commit to reducing their load or utilizing qualified local generation in exchange for capacity payments, with contractual penalties imposed for non-compliance [42]. Compliance is then verified using a baseline derived from historical consumption, which allows participants to measure their reductions locally in real time without requiring advanced monitoring infrastructure, relying instead on established market rules and evaluation procedures [38]–[40]. Despite this streamlined approach, only 59% of participants passed the 2024 IESO performance evaluation, primarily due to overestimating their committed capacity [43]. This underscores a critical gap: in the absence of a robust planning and management framework, participants struggle with (1) accurately estimating the achievable demand reduction capacity, and (2) effectively managing onsite resources during DR events to meet the committed reductions. An early attempt to address these challenges was proposed in [73], which introduced an optimal planning and contracting framework for equitable participation of building and electric vehicle owners in vehicle-to-building CMDR. While this framework incorporates existing market rules, it does not account for the uncertainty introduced by baseline-based performance evaluation. This omission can expose participants to penalties and lost revenue while potentially undermining the grid operator's reliability expectations.

Furthermore, load forecasting errors and baseline uncertainties expose participants to significant risk when they fail to meet committed demand reductions [32]. To mitigate these risks, integrating ES technologies is essential, particularly in dynamic market environments where real-time prices fluctuate, grid peak hours do not align with LEF peaks, and participants are required to deliver their committed DR capacity [44]. These considerations motivate the need to determine the optimal combination and allocation of ES systems across short and long term horizons to enable real-time price arbitrage, facility peak reduction, and CMDR participation, while reducing grid peaks and GHG emission. For instance, BES is highly effective for short-term applications such as EA and facility peak reduction due to its high round-trip efficiency and rapid cycling capability. However, its effectiveness in CMDR participation is limited because sustained energy availability and high-power delivery over extended periods are required, conditions better suited to long-term storage [36]. In this context, technologies such as HES and CAES offer high energy density and multi-hour discharge capability, albeit at the expense of lower round-trip efficiency [10], [13], [45]. These complementary characteristics motivate the exploration of hybrid ES solutions, where fast-cycling BES is combined with long-term technologies like HES or CAES to enable participants to meet both short-term arbitrage opportunities and CMDR obligations.

Based on the above discussions, the key research gaps in the existing literature on DRPs are summarized as follows. 1) Although several studies have investigated different forms of incentive-based DRPs, CMDR participation has received limited attention. Based on the available literature, no prior work has fully integrated the CMDR market rules and regulatory constraints into an optimal sizing and management framework for LEFs, either to accurately estimate their achievable DR capacity or to coordinate onsite resources during DR events to meet committed reductions. 2) Most existing studies focus on a single ES technology and do not examine how hybrid short and long terms ES systems can jointly enhance EA, facility peak reduction, and compliance with committed demand reductions in dynamic electricity markets. 3) Most DRP studies lack multi-objective optimization frameworks that jointly consider economic and environment metrics.

To address these gaps, Chapter 4 of this thesis presents an optimal sizing and management framework for LEFs with onsite generation and ES resources participating in CMDR. The proposed framework enables facility operators to accurately estimate obligated demand reduction under dynamic market regulations. It explicitly incorporates commercial electricity bill components, including EA and peak demand charges, CMDR rules, and the environmental impacts associated with grid GHG emissions. To ensure computational efficiency in the presence of highly nonlinear and nonconvex market constraints, a convex relaxation is introduced that allows facility operators to determine a conservative lower bound on achievable demand reduction. This bound represents the level of reduction that the LEF can reliably deliver under worst-case conditions while guaranteeing global optimality. In addition, the framework supports the optimal sizing of hybrid short and long terms ES systems to jointly maximize economic returns and environmental benefits.

## 2.4 Decentralization Approaches for Sustainable PDSs

The continuous growth in electricity demand from the residential and commercial sectors, which together account for nearly 40% of total energy consumption, combined with the accelerating electrification of other energy domains such as Electric Vehicles (EVs), has imposed significant pressure on power systems to satisfy rising demand while maintaining system reliability and avoiding costly infrastructure expansion [74], [75]. Moreover, the requirement to achieve net-zero GHG emissions in the electricity sector has introduced a new operational paradigm for PDSs, increasingly dependent on DERs, including distributed generation technologies such as PV systems and distributed storage solutions such as BES [76]. The integration of DERs into medium- and low-voltage PDSs has significantly increased the complexity of centralized system operation. This added complexity has driven the emergence of microgrids as an effective framework for managing localized generation and demand. Accordingly, there is a growing need to adopt decentralized and sustainable energy solutions capable of meeting rising electricity demand while simultaneously fulfilling environmental net-zero objectives [46].

In this context, microgrids are defined as medium- or low-voltage PDSs equipped with on-site distributed generation and ES resources to supply local demand. Microgrids can operate either in grid-connected mode, where the main grid supports local demand, or in islanded mode, where they function independently and rely solely on on-site DERs to satisfy their energy requirements [77]. The technical and economic feasibility of operating such microgrids in complete isolation has been extensively validated in recent literature. Studies demonstrate that with the optimal sizing of hybrid DERs and BES , isolated microgrids can robustly maintain a supply and demand balance without grid reliance. For instance, fully sustainable isolated systems have proven highly viable, utilizing diverse energy mixes such as solar, wind, and biomass to achieve economical and resilient power delivery independently of the main grid [78], [79]. Furthermore, the integration of demand management and flexible load regulation, including the utilization of mobile energy storage, significantly enhances dynamic supply and demand matching during such isolated operation [80]. The optimal sizing and management of on-site DERs within microgrids play a critical role in ensuring demand satisfaction without load curtailment, particularly during islanded operation or main grid failure. However, operating PDSs as a collection of fully independent microgrids may result in oversizing DER capacity to satisfy islanded operation requirements, leading to under-utilization during grid-connected operation. Conversely, sizing on-site DERs based solely on grid-connected assumptions may reduce capacity but risk failing to meet demand during islanded conditions [63]. Therefore, it is essential to establish a framework that enables PDSs to be clustered into groups of sustainable microgrids capable of collaborating during islanded operation. Such a framework should identify microgrids with similar electrical characteristics and within feasible operational distances, optimize their resources in a coordinated manner to prevent unnecessary oversizing, and allocate resources across the network buses, including reactive power support devices such as Shunt VAR compensators, to ensure voltage stability and minimize system losses [62].

The optimal planning and management of microgrids have been extensively investigated in previous studies, primarily focusing on estimating DER capacity and ensuring efficient real-time operation [81]. In this context, the interaction between microgrids and PDSs is commonly represented in two forms: 1) microgrids are allocated at a single bus within the PDSs, typically modeled as a DER or fixable load at the point of coupling, and 2) microgrids are structured as a group of interconnected PDSs buses that share common DERs and a coordinated control system.

In the first form, microgrids host on-site distributed generation, ES, and loads that are jointly controlled to create a bus within the PDSs capable of exhibiting flexible generation or load behavior, thereby enhancing overall system flexibility and operational performance [58]. Within this context, Chenjia Gu et al. [59] proposed a Mixed Integer Non-linear Programming (MINLP) framework for the optimal planning of DERs in hydrogen-based microgrids. To promote reduced GHG emissions, the accumulated carbon intensity is explicitly modeled, penalized in the objective function, and constrained by an upper limit. The hydrogen-based microgrids, together with DERs across the PDSs, are then optimally coordinated to minimize GHG emissions while improving hydrogen profitability and overall system efficiency. Similarly, the study in [60] introduced a two-stage stochastic rolling planning framework for microgrids. The proposed approach adopts a collaborative decentralized structure in which each microgrid manages its own resources while a centralized coordinator facilitates energy exchange among microgrids, allowing them to share surplus energy or request support from neighboring microgrids for energy trading among microgrids while excluding support from the main grid.

In a similar vein, Atazadegan et al. [61] investigated the effects of islanded, non-cooperative, and cooperative strategies on microgrid generation expansion planning. The findings indicate that enabling energy trading among microgrids can significantly enhance economic performance, yielding an improvement of approximately 18% in financial outcomes. To address the operational complexity of cooperative microgrids, the study in [82] proposed a master–slave game-based scheduling approach for a group of microgrids sharing a common BES. In the first stage of the two-stage framework, the capacity allocation share of the BES for the microgrid groups and the PDS is determined, along with the optimal scheduling of charge and discharge power. In the second stage, power interactions among the microgrids are coordinated under a cooperative alliance to ensure reliable demand satisfaction. However, these efforts predominantly model microgrids as single-bus entities (e.g., individual facilities or aggregated loads), which limits the representation of their physical and electrical interactions with the PDSs. Such simplifications often overlook the spatial distribution of resources, network constraints, and power flow impacts across multiple buses. Moreover, limited attention is given to how cooperative coordination among microgrids can be systematically leveraged to enhance overall PDSs performance, particularly in terms of voltage regulation, reactive power support, and network loss minimization.

On the other hand, the second form partitions the PDS electric buses into clusters of microgrids, where each microgrid is represented by a set of electrically interconnected and collaborative buses operating under distributed control frameworks [47]. The primary objective of this structure is to ensure reliable demand supply in the absence of main grid support or, alternatively, to minimize dependence on the main grid by maximizing the utilization of local resources. An early study in [48] addressed the resilience of PDSs against natural disasters by clustering the network into isolated spatial zones. Within this framework, distributed generation units were optimally planned and allocated across the PDSs under worst-case scenarios to minimize demand outages and enhance system resilience. Similarly, Habib et al. [49] proposed a Linear Programming (LP) planning framework for PDSs that considers clustering into four microgrids. The objective was to reduce overall operational costs while accounting for uncertainties associated with renewable energy and EVs integration, through the adoption of smart prosumers, Vehicle-to-Grid (V2G), and BES, thereby improving demand management and the controllability of clustered microgrids.

Zhao et al. [50], on the other hand, utilized hydrogen refueling stations to enhance the resilience of PDSs during main grid failures, where hydrogen transportation among stations is explicitly modeled through a spatial transportation network that accounts for geographical locations. Information gap decision theory is employed to achieve robust planning under uncertainties in demand and renewable energy generation. Likewise, the study in [51] proposed a microgrid formation and scheduling framework to support real-time system restoration during natural disasters while minimizing the number of load outages. The proposed two-stage framework first determines the optimal microgrid formation and subsequently performs the optimal scheduling of the formed microgrids. Although these studies account for PDSs interaction and represent microgrids as clusters of buses, the clustering process is often arbitrary or primarily driven by low-probability contingency events. Consequently, such approaches do not provide PDSs operators with a systematic method to classify the network based on its electrical characteristics, which is essential for enabling effective decentralized control and ensuring long-term sustainable operation of clustered microgrids. Recent advancements in microgrid planning have explored complex multi-level optimization structures to manage operational uncertainties. For instance, a tri-level robust optimization model was recently developed for planning bi-directional converter interconnections among predefined hybrid AC/DC microgrids [83]. This approach addresses dynamic converter efficiency and renewable energy uncertainty via a data-correlated uncertainty set formulated within a min-max-min mathematical structure. While highly effective for ensuring robust component sizing and operation against worst-case scenarios, such frameworks typically assume fixed, pre-existing microgrid boundaries.

In another line of research, several clustering techniques have been proposed for partitioning PDSs. In [53], a cooperative increment-based strategy is introduced, which relies on prior individual planning of each microgrid before the clustering process, thereby limiting its flexibility when microgrid planning is still evolving. In [54], a graph theory-based method is presented that offers computational efficiency but primarily focuses on topological uniformity and employs fixed cluster size thresholds based on the number of buses, with limited consideration of electrical characteristics. Among existing approaches, hierarchical clustering has attracted considerable attention for PDS applications due to its interpretability and adaptability. The method initially treats each node as an independent cluster and iteratively merges the most similar clusters according to a predefined proximity metric until a stopping criterion, such as a desired number of clusters, is satisfied. A crucial element in this process is the definition of electrical distance, which measures the similarity between nodes based on their electrical behavior. Electrical distance can be quantified using different metrics, including geographical distance, line impedance, voltage magnitude sensitivity, phase angle sensitivity [55], and power flow distribution factors [56]. These metrics capture diverse aspects of electrical interactions and facilitate the construction of distance matrices that better represent the intrinsic electrical structure of the network. Nevertheless, some of these formulations [55], [56] become computationally intensive for large-scale systems. Although the approach in [52] integrates spectral clustering with electrical distance matrices, its performance is highly dependent on the accuracy of the sensitivity matrix and it still entails considerable computational burden when applied to large distribution networks. Recent advancements in microgrid planning have explored complex multi-level optimization structures to manage operational uncertainties. For instance, a tri-level robust optimization model was recently developed for planning bi-directional converter interconnections among predefined hybrid AC/DC microgrids [83]. This approach addresses dynamic converter efficiency and renewable energy uncertainty via a data-correlated uncertainty set formulated within a min-max-min mathematical structure. While highly effective for ensuring robust component sizing and operation against worst-case scenarios, such frameworks typically assume fixed, pre-existing microgrid boundaries.

Despite the extensive body of literature on microgrid planning, clustering, and cooperative operation, existing frameworks largely address specific aspects of the problem in isolation and lack a holistic perspective tailored to PDSs. In particular, several key research gaps can be identified. Most studies model microgrids as single-bus or aggregated entities, neglecting their multi-bus electrical interactions within PDSs and limiting the accuracy of system-level representation. Additionally, existing clustering approaches often rely on arbitrary partitioning, topological metrics, or contingency-driven designs, rather than electrically informed and accurate clustering that reflects true network characteristics. Furthermore, limited attention is given to the resources allocation within PDS buses, including both active and reactive power support, to enhance voltage regulation, loss minimization, and operational efficiency. Finally, most approaches do not provide a unified operational structure that enables flexible modes, such as cooperative energy sharing among clustered microgrids, or islanded operation from the main grid. Consequently, none of the existing frameworks ensure accurate microgrid clustering within PDSs for long-term sustainability, while simultaneously supporting adaptive resource planning, scalable expansion, and coordinated allocation of resources across interconnected microgrids.

To address the aforementioned research gaps, Chapter 5 of this thesis proposes a hierarchical tri-stage optimization framework for clustering PDSs into sustainable and cooperative micro-

Table 2.2: Summary of literature review and comparison with the proposed model.

| Ref | Decentralization | Planning | Management | Op. Modes | Resource Allocation |
|---|---|---|---|---|---|
| [59], [60], [83] | × | ✓ | ✓ | × | × |
| [61], [82] | × | ✓ | ✓ | ✓ | × |
| [47] | ✓ | ✓ | × | × | × |
| [48] | ✓ | ✓ | ✓ | × | ✓ |
| [49] | × | × | ✓ | × | × |
| [53], [57] | ✓ | ✓ | ✓ | × | × |
| [52], [54], [56] | ✓ | × | × | × | × |
| [50], [51], [55] | ✓ | × | ✓ | × | × |
| **Proposed Model** | ✓ | ✓ | ✓ | ✓ | ✓ |

grids. In the first stage, a simple yet effective hierarchical agglomerative clustering method is developed based on an electrical distance matrix constructed from the impedance characteristics of distribution lines, enabling electrically meaningful partitioning of the network. In the second stage, the DERs of the formed microgrids are optimally planned, where renewable generation and BES capacities are designed to ensure resilient operation with minimal dependence on the main grid, including the capability for fully isolated operation when required. In the third stage, the planned DER capacities are optimally allocated across the PDS buses, together with reactive power support resources, to enhance voltage stability and minimize network power losses while ensuring coordinated operation of the clustered microgrids. A comparative summary of the discussed literature and the proposed framework is presented in Table 2.2.

## 2.5 Chapter Summary

This chapter provides a comprehensive review of the existing literature surrounding ES integration, DR mechanisms, and distribution network decentralization, identifying critical research gaps that motivate the proposed frameworks in this thesis. Current techno-economic studies on AA-CAES frequently overlook long-term and seasonal operational dynamics, multi-service participation (such as OR and CMDR), and real-time market pricing. Furthermore, they often decouple system sizing from operational scheduling and rely on simplified thermodynamic models. To bridge these gaps, this thesis introduces a holistic optimization framework that jointly determines the optimal sizing and scheduling of AA-CAES systems to maximize revenue across diverse GSs markets under realistic pricing and physical constraints.

Shifting the focus from grid-scale storage to consumer-side flexibility, the existing literature on DRPs lacks a comprehensive integration of CMDR regulatory rules into the optimal sizing and management of LEFs. Previous studies also fail to adequately explore the synergistic use of hybrid short- and long-term ES systems, or to incorporate multi-objective economic and environmental metrics. Consequently, this thesis proposes an optimal planning framework that explicitly integrates dynamic market regulations through convex relaxation, enabling the reliable dispatch of hybrid storage systems while maximizing both financial returns and decarbonization efforts.

At the distribution network level, current decentralization approaches for PDSs often rely on arbitrary topological clustering or contingency-driven designs, frequently modeling microgrids as oversimplified single-bus entities. These methods typically neglect the true electrical characteristics of the network and lack coordinated strategies for active and reactive power resource allocation. Addressing these limitations, this thesis develops a hierarchical tri-stage optimization framework that accurately partitions PDSs based on electrical distance, optimizes the stochastic planning of DERs, and strategically allocates these resources across interconnected microgrids to enhance voltage stability, minimize power losses, and support flexible operational modes.

# Chapter 3

# Optimal Deployment of AA-CAES for GS Provision in Diverse Electricity Markets

## 3.1 Nomenclature

### 3.1.1 Indices and Sets

| | |
|---|---|
| $t$ | Index of time interval. |
| $n^c$, $n^{tr}$ | Indices of compressors and turbines. |
| $b$, $q$ | Indices of buses. |
| $\mathbb{T}$ | Set of optimization time steps. |
| $\mathbb{T}^{OR}_{Rmp}$ | Ramping period of OR. |
| $\mathbb{T}^{CMDR}$, $\mathbb{T}^{CMDR}_{start}$ | Sets of time steps and start times for CMDR activation windows. |
| $\mathbb{T}^{STD}$ | Set of time steps defining standard baseline periods prior to CMDR activation. |

### 3.1.2 Parameters

| | |
|---|---|
| $\Delta t$ | Simulation time step (hour). |

| | |
|---|---|
| $\Delta t^{STD}$ | Duration of standard baseline period (hours). |
| $\lvert\mathbb{T}_e^{CMDR}\rvert$ | Duration of a CMDR activation event. |
| $B$ | Total number of buses. |
| $\gamma$, $R$ | Specific heat ratio, and gas constant (J/kg·K). |
| $N^c$, $N^{tr}$ | Number of compressors and turbines. |
| $\eta^m$, $\eta^g$ | Efficiency of electric motor and generator. |
| $\eta^c$, $\eta^{tr}$ | Efficiency of compressors and turbines. |
| $r_c$, $r_{tr}$ | Compression and expansion ratio. |
| $C_p^a$, $C_p^w$ | Specific heat capacity of air and water (J/kg·K). |
| $\underline{p^r}$, $\overline{p^r}$ | Pressure limits of the air reservoir (bar). |
| $\underline{m^a}$, $\overline{m^a}$ | Stored air mass limits in the air reservoir (kg). |
| $T^r$, $V^r$ | Air reservoir temperature and volume (K, m$^3$). |
| $p^r_{init}$, $m^a_{init}$ | Initial reservoir pressure and air mass (bar, kg). |
| $T_{amb}$ | Ambient air temperature (K). |
| $T^c_{in,n^c}$ | Inlet air temperature of $(n^c)^{th}$ compressor (K). |
| $T^c_{out,n^c}$ | Outlet air temperature of $(n^c)^{th}$ compressor (K). |
| $T^{tr}_{in,n^{tr}}$ | Inlet air temperature of $\left(n^{tr}\right)^{th}$ turbine (K). |
| $T^{tr}_{out,n^{tr}}$ | Outlet air temperature of $\left(n^{tr}\right)^{th}$ turbine (K). |
| $\dot{m}^a_{HX^c_{n^c}}$ | Air mass flow rate in compressor-side Heat Exchangers (HXs) (kg/s). |
| $\dot{m}^w_{HX^c_{n^c}}$ | Water mass flow rate in compressor-side HXs (kg/s). |
| $\dot{m}^a_{HX^{tr}_{n^{tr}}}$ | Air mass flow rate in turbine-side HXs (kg/s). |
| $\dot{m}^w_{HX^{tr}_{n^{tr}}}$ | Water mass flow rate in turbine-side HXs (kg/s). |
| $T^a_{HX^c_{n^c}}$ | Air temperature of compressor-side HXs (K). |

$T^{w}_{HX^{c}_{n^c}}$ Water temperature of compressor-side HXs (K).

$T^{a}_{HX^{tr}_{n^{tr}}}$ Air temperature of turbine-side HXs (K).

$T^{w}_{HX^{tr}_{n^{tr}}}$ Water temperature of turbine-side HXs (K).

$U(r,\tau)$ Capital recovery factor.

$r$, $\tau^{s}$ Interest rate (%), and unit s lifetime (years).

$C^{c}$, $C^{tr}$ CapEx of compressors and turbines ($/MW).

$O^{c}$, $O^{tr}$ OpEx of compressors and turbines ($/MWh).

$e^{Pr}_{t}$ Market electricity price at time $t$ ($/MWh).

$OR^{Pr}_{t}$ OR market price at time $t$ ($/MWh).

$RR$ Maximum ramp rate of compressors and turbines (MW/min).

$C^{CMDR}$ Awarded CMDR price ($/MW-day).

$n^{BD}$ Number of business days eligible for CMDR.

$T^{tr}_{icing}$ Minimum turbine outlet temperature to prevent icing (K).

$t^{CMDR}_{prep,\min}$ Minimum preparation time required before CMDR activation window (hours).

$\delta^{CMDR}$ Permissible deviation margin from committed capacity during CMDR activation (%).

$\underline{V^{b}}$, $\overline{V^{b}}$ Voltage limits at bus $b$ (p.u.).

$\overline{S^{b}}$ Maximum apparent power limit of the branch connected to bus $b$ (p.u.).

$Y^{b,q}$, $\theta^{b,q}$ Magnitude and phase angle of admittance between buses $b$ and $q$ (p.u.).

### 3.1.3 Variables

$P^{ch}_{t}$, $P^{dch}_{t}$ Charging and discharging power of AA-CAES at time $t$ (MW).

$P^{OR,ch}_{t}$ Portion of charging power allocated to OR at time $t$ (MW).

$P^{OR,dch}_{t}$ Portion of discharging power allocated to OR at time $t$ (MW).

| | |
|---|---|
| $P_t^{EA,ch}$ | Portion of charging power allocated to EA at time $t$ (MW). |
| $P_t^{EA,dch}$ | Portion of discharging power allocated to EA at time $t$ (MW). |
| $C_t$, $D_t$ | Charging and discharging status of AA-CAES at time $t$. |
| $S^c$, $S^{tr}$ | Rated power of compressors and turbines (MW). |
| $\dot{m}_t^c$, $\dot{m}_t^{tr}$ | Air mass flow rate of compressors and turbines at time $t$ (kg/s). |
| $p_t^{in}$, $p_t^{de}$ | Air pressure increase and decrease in air reservoir at time $t$ (bar). |
| $p_t^r$, $m_t^a$ | Pressure and mass of air in the reservoir at time $t$ (bar, kg). |
| $P^{CMDR}$ | Committed discharge capacity for CMDR (MW). |
| $P^{STD}$ | Standard baseline limit during the designated standard period for CMDR (MW). |
| $V_t^b$, $\delta_t^b$ | Voltage magnitude and phase angle at bus $b$ at time $t$ (p.u.). |
| $S_t^b$ | Apparent flow through branch connected to bus $b$ at time $t$ (p.u.). |
| $P_t^{b,g}$, $Q_t^{b,g}$ | Active and reactive power generation at bus $b$ at time $t$ (p.u.). |
| $P_t^{b,d}$, $Q_t^{b,d}$ | Active and reactive power demand at bus $b$ at time $t$ (p.u.). |
| $P_{t,\exp}^{b^*,\max}$ | Maximum export power limit at the point of connection, bus $b^*$ (MW). |
| $P_{t,}^{b^*,\max}$ | Maximum import power limit at the point of connection, bus $b^*$ (MW). |

## 3.2 Introduction

This chapter presents a novel framework to optimize the deployment of grid-connected AA-CAES considering its participation in GSs across diverse electricity markets. The proposed framework determines the component sizing of an AA-CAES facility and its operational scheduling across multiple timescales, including short-term (daily), long-term (weekly), and seasonal (monthly to yearly), by utilizing flexible dispatch horizons. The proposed framework aims to minimize capital and operational costs of the facility while maximizing GSs revenues, i.e., OR and CMDR. The developed framework accounts for the AA-CAES thermodynamic constraints and power grid capacity and voltage limits. The optimization framework yields the optimal sizes of AA-CAES components; the hourly optimal power imports and exports; and the hourly power participation in each GS. The proposed framework is validated using the IEEE 30-bus benchmark system and real historical data across three different electricity markets, each employing a distinct electricity pricing scheme. The results show that AA-CAES is economically feasible for CMDR across all markets, while being more suitable for EA and OR provision in markets characterized by high price variability. The results also indicate that extending the scheduling horizon increases revenue, thereby demonstrating the viability of AA-CAES as a long- and seasonal-term storage technology. The main contributions of this work are summarized as follows:

- The proposed optimization framework for techno-economic analysis employs a detailed yet computationally efficient thermodynamic AA-CAES model, accurately capturing the interdependence among compressed air temperature, pressure, and flow dynamics. This ensures realistic performance representation while maintaining tractability for large-scale optimization.
- It integrates multiple electricity markets with diverse pricing schemes, i.e., fixed, low variability, and high hourly variability, while evaluating AA-CAES participation in GSs. This feature enables robust revenue maximization strategies across EA and GSs markets under varying economic scenarios.
- The framework supports adjustable scheduling horizons, allowing assessment AA-CAES feasibility across short-, long-, and seasonal-term operations. This multi-scale approach provides strategic insights for investment planning and operational flexibility, ensuring profitability under dynamic market and seasonal conditions.

The remaining sections of the chapter are organized as follows: Section 3.3 presents the mathematical model of the AA-CAES and provides a comprehensive explanation of the associated GSs. Then, Section 3.4 outlines the formulation of the proposed sizing and operation optimization model. In Section 3.5, the results of the numerical analysis are discussed. Finally, this chapter is concluded in Section 3.6.

## 3.3 System Description

This section presents the modeling of the AA-CAES and illustrates its participation in GSs. Fig. 3.1 shows a schematic diagram of a grid-connected AA-CAES. As depicted, AA-CAES

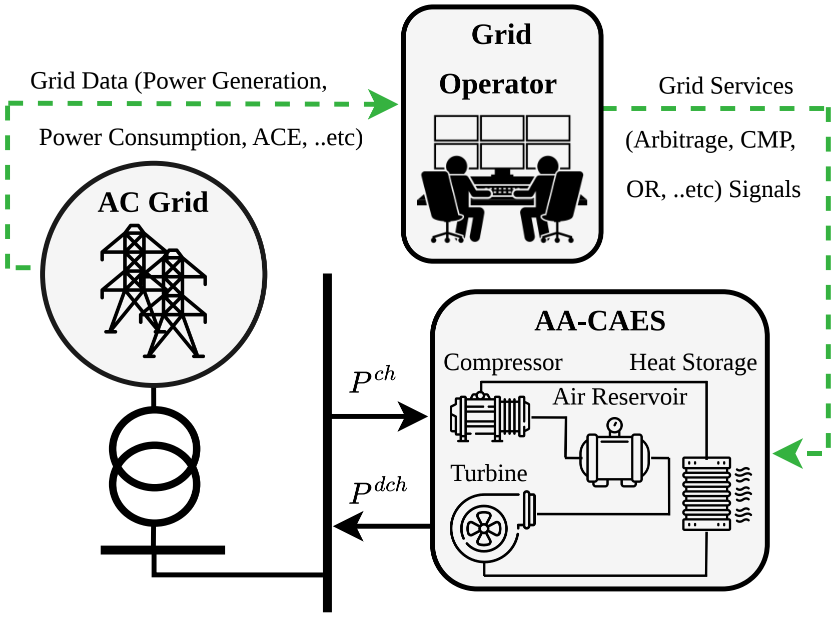


Figure 3.1: AA-CAES–grid operator interaction for GSs provision.

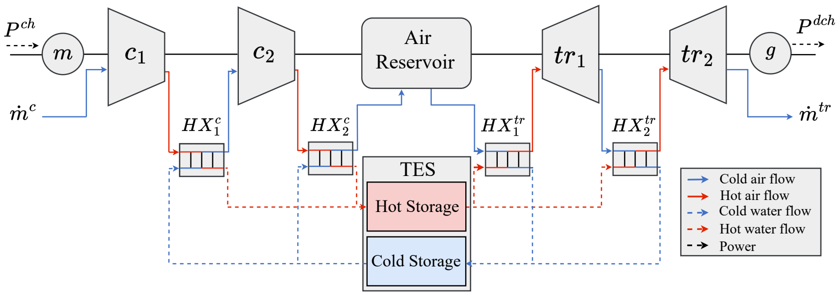


Figure 3.2: Schematic diagram of the AA-CAES.

receives communication signals from the grid operator based on grid data to manage its EA and participation in GSs. By responding to operator signals and incorporating market data, the AA-CAES optimally manages its charging and discharging to maximize its revenue.

### 3.3.1 AA-CAES Modeling

Fig. 3.2 presents a schematic diagram of the AA-CAES. As depicted, the AA-CAES comprises a motor, multi-stage compressors, an air reservoir, multi-stage turbines, a generator, HXs , and a TES unit. During the charging phase, electrical energy is used to power the motor, which drives the compressors. As air is compressed, its pressure and temperature increase. The thermal energy generated during compression is extracted using the compressor-side HXs and stored in the TES. The resulting cooled, pressurized air is then stored in the air reservoir.

During the discharging phase, the recovered thermal energy from compression is used to enhance the overall energy conversion efficiency. This is achieved by preheating either the stored pressurized air or the cold air exiting intermediate turbine stages as a result of expansion. The preheated air is then expanded through the turbines, where it drives the generator to produce electricity.

The AA-CAES is modeled based on the following assumptions [84], [85]: air obeys ideal gas law, the air reservoir is treated as isothermal, and the TES is adiabatic.

#### 3.3.1.1 Compressors and Turbines

The charging and discharging powers of the compressors and turbines, respectively, are calculated as follows:

$$P_t^C = \frac{1}{\eta^m \eta^c} C_p^a \sum_{n^c \in N^c} \left( r_c^{\frac{\gamma-1}{\gamma}} - 1 \right) T_t^{n^c,in} \cdot \dot{m}_t^c, \ \forall t \in \mathbb{T}_m \tag{3.1}$$

$$P_t^T = \eta^g \eta^{tr} C_p^a \sum_{n^{tr} \in N^{tr}} \left( 1 - r_{tr}^{\frac{1-\gamma}{\gamma}} \right) T_t^{n^{tr},in} \cdot \dot{m}_t^{tr}, \ \forall t \in \mathbb{T}_m \tag{3.2}$$

Where the efficiencies of the compressors $\eta^c$ and turbines $\eta^t$ are calculated using empirical correlations [86], given by:

$$\eta^c = 0.91 - \frac{r_c - 1}{300} \tag{3.3}$$

$$\eta^{tr} = 0.90 - \frac{r_{tr} - 1}{250} \tag{3.4}$$

#### 3.3.1.2 Air Reservoir

The rate of pressure increase due to compressors charging can be calculated by:

$$p_t^{in} = \frac{RT^r}{V^r} \cdot \dot{m}_t^c \quad \forall t \in \mathbb{T} \tag{3.5}$$

Similarly, the pressure decrease due to turbines discharging is given by:

$$p_t^{de} = \frac{RT^r}{V^r} \cdot \dot{m}_t^{tr} \quad \forall t \in \mathbb{T} \tag{3.6}$$

The total reservoir pressure $p_t^r$ is updated recursively based on the net effect of charging and discharging flows at each time step [19]:

$$p_t^r = p_{t-1}^r + \left( C_t \cdot p_t^{in} - D_t \cdot p_t^{de} \right) \cdot \Delta t \quad \forall t \in \mathbb{T} \tag{3.7}$$

The air mass stored in the reservoir is updated according to the following relation:

$$m_t^a = m_{t-1}^a + \left(C_t \cdot \dot{m}_t^c - D_t \cdot \dot{m}_t^{tr}\right) \cdot \Delta t \quad \forall t \in \mathbb{T} \tag{3.8}$$

#### 3.3.1.3 TES and HXs

The outlet air temperatures of the $(n^c)^{th}$ compressor and the $\left(n^{tr}\right)^{th}$ turbine are defined by the following expressions, respectively [19]:

$$T_{out,n^c}^c = T_{in,n^c}^c \left[1 + \frac{1}{\eta^c}\left(r_c^{\frac{\gamma-1}{\gamma}} - 1\right)\right] \tag{3.9}$$

$$T_{out,n^{tr}}^{tr} = T_{in,n^{tr}}^{tr} \left[1 - \left(1 - r_{tr}^{\frac{1-\gamma}{\gamma}}\right)\eta^{tr}\right] \tag{3.10}$$

The heat exchange between the air and the heat storage medium on the compression side is governed by an energy balance in $HX_1^c$ and $HX_2^c$, as follows [21]:

$$\begin{aligned} &\dot{m}_{HX_{n^c}^c}^a C_p^a \left(T_{out,n^c}^c - T_{HX_{n^c}^c,out}^a\right) = \\ &\dot{m}_{HX_{n^c}^c}^w C_p^w \left(T_{HX_{n^c}^c,out}^w - T_{HX_{n^c}^c,in}^w\right) \end{aligned} \tag{3.11}$$

On the expansion side, the corresponding heat exchange in $HX_1^{tr}$ and $HX_2^{tr}$ follows [21]:

$$\begin{aligned} &\dot{m}_{HX_{n^{tr}}^{tr}}^a C_p^a \left(T_{in,n^{tr}}^{tr} - T_{HX_{n^{tr}}^{tr},in}^a\right) = \\ &\dot{m}_{HX_{n^{tr}}^{tr}}^w C_p^w \left(T_{HX_{n^{tr}}^{tr},out}^w - T_{HX_{n^{tr}}^{tr},in}^w\right) \end{aligned} \tag{3.12}$$

### 3.3.2 AA-CAES Participation in GSs

EA refers to the profits obtained by strategically charging the AA-CAES during periods of low electricity prices and discharging during periods of high prices, in response to market fluctuations. In the OR service, participants receive activation signals to increase their power output and are compensated for each megawatt-hour imported/exported from the grid [15]. Upon receiving the activation signal, the participant must reach the requested power output within the allowed ramping period, $\mathbb{T}_{Rmp}^{OR}$, which typically spans a few minutes [87]. CMDR can take various forms–one of which requires participants to commit to maintaining a specified discharge capacity during predefined availability windows. In this arrangement, participants receive compensation for their readiness, regardless of whether activation is ultimately required [87]. The payment is determined by the awarded price and the committed capacity. To determine this compensation, system operators implement a structured market process. The CMDR

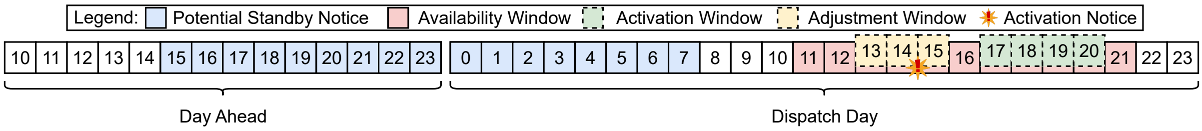


Figure 3.3: CMDR key milestones and time windows.

process begins with the obligation period, during which participants submit their available capacity in MW along with the associated bid price in \$/MW. Subsequently, the PSO publishes the final list of CMDR providers and the corresponding market clearing price. During activation events, the selected providers are obligated to deliver the committed capacity in accordance with established market guidelines and operational rules.

Fig. 3.3 illustrates the key milestones and associated time windows of a typical CMDR event. As shown, the grid operator issues a standby notice either on the preceding day or during the early morning of the event day. CMDR activation may commence at any point within the availability window, with the actual activation time window representing the period during which providers are obligated to maintain their committed capacity. There should be an interval between the end of the standby notice period and the start of the availability window, which represents the minimum preparation time $t^{CMDR}_{prep,min}$. This can reflect a worst-case scenario in which the AA-CAES may begin from its minimum allowable pressure and must complete charging within this limited period to ensure readiness for activation. It is worth noting that the timing and duration of the availability and activation windows may vary across seasons, and that activations are restricted to business days only [87].

CMDR performance is evaluated against a standard baseline; only the portion of power exceeding this baseline is recognized as eligible. To comply with this requirement, the AA-CAES is restricted from exceeding the baseline power $P^{STD}$ during designated standard periods, which are defined as time intervals preceding each CMDR activation. Specifically, for every activation start time $t \in \mathbb{T}^{CMDR}_{start}$, the corresponding standard period is defined as a fixed-length window that spans from $t - \Delta t^{STD}$ to $t$.

$$\mathbb{T}^{STD} = \big[t - \Delta t^{STD},\, t\big) \quad \forall\ t \in \mathbb{T}^{CMDR}_{start} \tag{3.13}$$

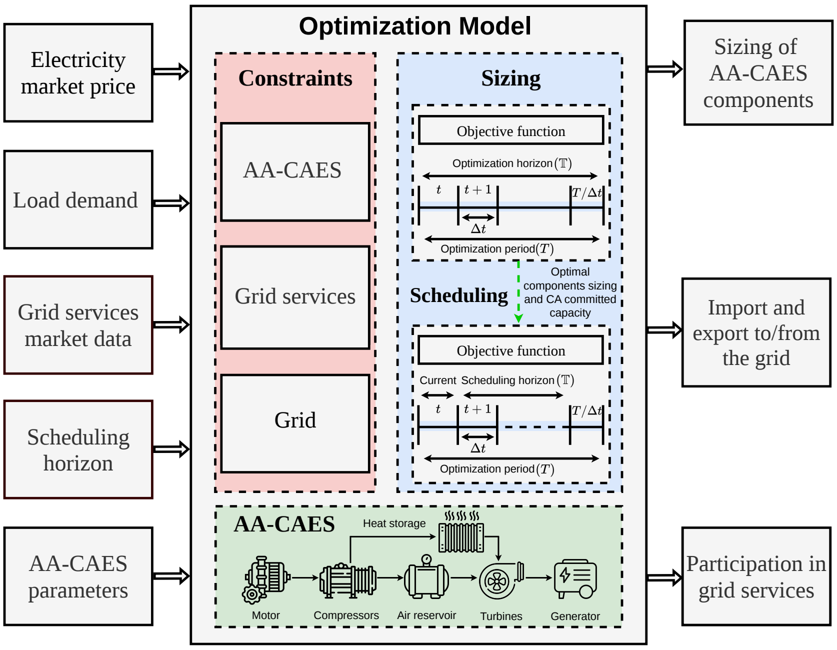


Figure 3.4: Outline of the proposed optimization framework.

## 3.4 Problem Formulation

This section provides the mathematical formulation of the proposed optimization framework. Fig. 3.4 illustrates the outline of this formulation. As shown in the figure, the formulation comprises two interdependent stages: component sizing and operational scheduling. In the sizing stage, the model determines the optimal compressor and turbine subsystem sizes for system design, as well as the CMDR contract obligation capacity, which are subsequently used as fixed inputs in the operation stage. The sizing stage is performed for the entire optimization period to capture the long- and seasonal-term storage capabilities, while the operation stage employs adjustable scheduling horizons, allowing the assessment of AA-CAES feasibility across short-, long-, and seasonal-term operations. The following subsections present the detailed mathematical formulation of the proposed optimization framework's objective function and constraints as described hereunder.

### 3.4.1 Objective Function

The objective function considers five system cost components (i.e., CapEx, OpEx, EA, CMDR, and OR revenues) with the aim of maximizing the net profit as provided below:

$$\min \sum_{t \in T} CapEx + OpEx - Rev^{EA} - Rev^{OR} - Rev^{CMDR} \tag{3.14}$$

The consideration of CapEx in the objective function aims to optimally determine the sizes of the compressor $S^c$ and turbine $S^{tr}$ subsystems. The investment cost is dominated by the turbomachinery, which accounts for 85% of the total CapEx [88].

$$CapEx = U(r, \tau^c) \cdot C^c \cdot S^c + U(r, \tau^{tr}) \cdot C^{tr} \cdot S^{tr} \tag{3.15}$$

Here it is worth noting that the CapEx of each system unit in (3.15) captures the time value of money by using the annuity factor formula with $r$ interest rate for a period of $\tau$ years, given as [89]:

$$U(r, \tau) = \frac{r(1+r)^{\tau}}{(1+r)^{\tau} - 1} \cdot \frac{1}{8760} \tag{3.16}$$

In addition to investment-related costs, the objective function incorporates OpEx (3.17), which represents the costs associated with operating and maintaining the AA-CAES compressors and turbines during charging and discharging over the dispatch horizon.

$$OpEx = \left(P_t^{ch} \cdot O^c + P_t^{dch} \cdot O^{tr}\right) \cdot \Delta t \quad \forall t \in \mathbb{T} \tag{3.17}$$

The revenue expression in (3.18) quantifies the financial gains associated with EA by computing the net profit resulting from the time-shifted operation of the AA-CAES, based on market electricity prices $e_t^{Pr}$ and the corresponding charging and discharging schedules.

$$Rev^{EA} = e_t^{Pr} \cdot \left(P_t^{EA,dch} - P_t^{EA,ch}\right) \cdot \Delta t \quad \forall t \in \mathbb{T} \tag{3.18}$$

The revenue from participation in the OR market is computed using (3.19) as the product of the OR market price $OR_t^{Pr}$ and the portion of the AA-CAES power allocated to OR provision, at each time step.

$$Rev^{OR} = OR_t^{Pr} \cdot (P_t^{OR,dch} + P_t^{OR,ch}) \cdot \Delta t \quad \forall t \in \mathbb{T} \tag{3.19}$$

The revenue associated with CMDR is represented in (3.20) as the product of the awarded price $C^{CMDR}$, the committed discharge capacity $P^{CMDR}$, and the number of eligible business days $n^{BD}$ during which the service is offered.

$$Rev^{CMDR} = P^{CMDR} \cdot C^{CMDR} \cdot n^{BD} \tag{3.20}$$

Where the committed $P^{CMDR}$ capacity is defined as the excess turbines capacity available above the baseline, expressed as:

$$P^{CMDR} = S^{tr} - P^{STD} \tag{3.21}$$

This encourages to select a turbines rating that enables profitable market participation while satisfying baseline-based eligibility rules.

The objective function in (3.14) is subject to a set of constraints arising from the AA-CAES operational characteristics, its participation in grid services, and interactions with the grid, as explained in the following subsections.

### 3.4.2 AA-CAES Constraints

Given the detailed model of the AA-CAES presented in (4.27)–(3.12), the following constraints are imposed:

#### 3.4.2.1 Compressors and Turbines

The compressors and turbines are constrained to operate within their respective rated power, as follows:

$$0 \leq P_t^{ch} \leq C_t \cdot S^c \quad \forall t \in \mathbb{T} \tag{3.22a}$$

$$\text{where,} \quad P_t^{ch} = P_t^{EA,ch} + P_t^{OR,ch} \tag{3.22b}$$

$$0 \leq P_t^{dch} \leq D_t \cdot S^{tr} \quad \forall t \in \mathbb{T} \tag{3.23a}$$

$$\text{where,} \quad P_t^{dch} = P_t^{EA,dch} + P_t^{OR,dch} \tag{3.23b}$$

To prevent simultaneous charging and discharging, a mutual exclusivity condition is enforced through:

$$C_t + D_t \leq 1 \quad \forall t \in \mathbb{T} \tag{3.24}$$

#### 3.4.2.2 Air Reservoir

The pressure increase and decrease within the air reservoir are bound to comply with the simulation's hourly resolution by limiting the duration of air mass transfer. These operational limits are captured by the following constraints:

$$\frac{p_t^{in} V^r}{R T^r \dot{m}_t^c} \leq 3600 \quad \forall t \in \mathbb{T} \tag{3.25}$$

$$\frac{p_t^{de} V^r}{R T^r \dot{m}_t^{tr}} \leq 3600 \quad \forall t \in \mathbb{T} \tag{3.26}$$

The reservoir pressure and stored air mass at the initial time step are initialized using the known initial values, $p_{init}^r$ and $m_{init}^a$, with adjustments that account for whether the AA-CAES begins in charging or discharging mode. These initialization rules are expressed as follows:

$$p_1^r = p_{init}^r + \left( C_t \cdot p_1^{in} - D_1 \cdot p_1^{de} \right) \cdot \Delta t \tag{3.27}$$

$$m_1^a = m_{init}^a + \left( C_1 \cdot \dot{m}_1^c - D_1 \cdot \dot{m}_1^{tr} \right) \cdot \Delta t \tag{3.28}$$

For the scheduling stage, the initial reservoir pressure and stored air mass at the beginning of each new scheduling horizon are set equal to the stored values from the preceding horizon.

The air reservoir pressure, as defined in (4.39) and (3.27), is subject to the following operational limits:

$$\underline{p^r} \leq p_t^r \leq \overline{p^r} \quad \forall t \in \mathbb{T} \tag{3.29}$$

Similarly, the stored air mass, defined in (3.8) and (3.28), is constrained by the following operational limits:

$$\underline{m^a} \leq m_t^a \leq \overline{m^a} \quad \forall t \in \mathbb{T} \tag{3.30}$$

#### 3.4.2.3 TES and HX

Mechanical reliability of the turbine is ensured by maintaining the outlet air temperature (3.10) above the icing threshold:

$$T_{out,n^{tr}}^{tr} \geq T_{icing}^{tr} \tag{3.31}$$

Considering that the air mass flow rate through the heat exchangers, $\dot{m}_{HX}^a$, is four times the water mass flow rate, $\dot{m}_{HX}^w$, a comparable temperature change between the two fluids can be achieved. Consequently, the following temperature relationships hold:

$$T_{in,n^c}^c = T_{amb}, \qquad T_{in,n^{tr}}^{tr} = T_{out,n^c}^c \tag{3.32}$$

### 3.4.3 GSs Constraints

During the participation in OR, the ramping up and down of both charging and discharging power allocated to OR within the allowed ramping period, $\mathbb{T}_{Rmp}^{OR}$, must not exceed the maximum ramp rate of the AA-CAES, $RR$, as follows:

$$\frac{|P_t^{OR,ch} - P_{t-1}^{OR,ch}|}{\mathbb{T}_{Rmp}^{OR}} \leq RR \quad \forall\, t \in \mathbb{T} \tag{3.33a}$$

$$\frac{|P_t^{OR,dch} - P_{t-1}^{OR,dch}|}{\mathbb{T}_{Rmp}^{OR}} \leq RR \quad \forall\, t \in \mathbb{T} \tag{3.33b}$$

To ensure that the AA-CAES fulfills its contractual obligations under the CMDR framework, a set of operational constraints is imposed in accordance with market rules and service requirements. The AA-CAES must store sufficient energy during the minimum preparation period $t_{prep,min}^{CMDR}$ to sustain the required discharge throughout the CMDR activation window. To ensure feasibility under this conservative scheduling, the following energy balance constraint is imposed during the component sizing stage:

$$\frac{S^c}{\eta^m \eta^c} \cdot t_{prep,min}^{CMDR} \geq S^{tr} \cdot \eta^g \eta^{tr} \cdot |\mathbb{T}_e^{CMDR}| \tag{3.34}$$

Where $t_{prep,min}^{CMDR}$ represents the smaller of the summer and winter preparation times, and $|\mathbb{T}_e^{CMDR}|$ denotes the number of time steps associated with a specific CMDR activation event.

To align with performance evaluation criteria in CMDR, the discharging power is restricted during the defined standard periods, enforced through the following constraint:

$$P_t^{EA,dch} \leq P^{STD} \quad \forall\, t \in \mathbb{T}^{STD} \tag{3.35}$$

During the CMDR activation window, the system is required to deliver power that closely follows the committed capacity $P^{CMDR}$, subject to a specified tolerance $\delta^{CMDR}$, while also ensuring exceeding the baseline power $P^{STD}$:

$$(1 - \delta^{CMDR}) \cdot (P^{CMDR} + P^{STD}) \leq P_t^{EA,dch} \leq (P^{CMDR} + P^{STD}) \quad \forall\, t \in \mathbb{T}^{CMDR} \tag{3.36}$$

The expression in (3.36) ensures that the discharge power during each activation period remains within the allowable deviation band around the committed capacity and remains above the baseline threshold, thereby guaranteeing compliance with CMDR performance requirements.

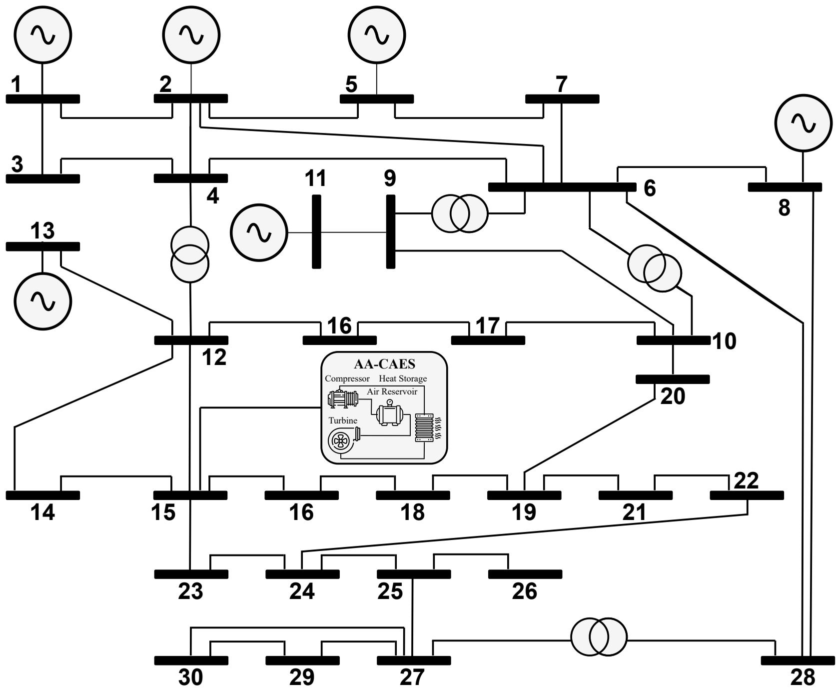


Figure 3.5: Single line diagram of IEEE 30-bus system under study.

### 3.4.4 Grid Constraints

The optimization model also considers the maximum power limits that the AA-CAES system can export ($P_{t,\,exp}^{b^*,\max}$) or import ($P_{t,\,imp}^{b^*,\max}$) to/from the grid at the point of connection, bus ($b^*$), as follows:

$$P_t^{ch} \leq P_{t,\,exp}^{b^*,\max} \quad \forall\, t \in \mathbb{T} \tag{3.37a}$$

$$P_t^{dch} \leq P_{t,\,imp}^{b^*,\max} \quad \forall\, t \in \mathbb{T} \tag{3.37b}$$

The export and import power limits are functions of the grid bus voltages, thermal line capacities, and active and reactive power flows. Therefore, two sub-optimization problems are solved to determine these limits: i) maximizing the power export at bus $b^*$, $P_{exp}^{b^*}$, and ii) maximizing the power import at bus $b^*$, $P_{imp}^{b^*}$ as provided in (3.38a) and (3.38b), respectively.

$$P_{t,\,exp}^{b^*,\max} = \max_{\mathbf{P_t},\mathbf{Q_t},\mathbf{V_t},\delta_\mathbf{t}} \; P_{t,\,exp}^{b^*} \quad \forall\, t \in \mathbb{T} \wedge\, b \in \mathbb{B} \tag{3.38a}$$

$$P_{t,\,imp}^{b^*,\max} = \max_{\mathbf{P_t},\mathbf{Q_t},\mathbf{V_t},\delta_\mathbf{t}} \; P_{t,\,imp}^{b^*} \quad \forall\, t \in \mathbb{T} \wedge\, b \in \mathbb{B} \tag{3.38b}$$

Each of these sub-optimization problems is subject to the grid constraints, including bus voltage $V_t^b$, thermal line capacity $S_t^b$, active power flow $P_t^b$, and reactive power flow $Q_t^b$, as defined in

(3.39), (3.40), (3.41), and (3.42), respectively.

$$\underline{V^b} \leq V_t^b \leq \overline{V^b} \quad \forall t \in \mathbb{T} \wedge b \in \mathbb{B} \tag{3.39}$$

$$S_t^b \leq \overline{S^b} \quad \forall t \in \mathbb{T} \wedge b \in \mathbb{B} \tag{3.40}$$

$$P_t^{b,g} = P_t^{b,d} + V_t^b \sum_{q=1}^{B} V_t^q Y^{b,q} Cos(\delta_t^b - \delta_t^q - \theta^{b,q}) \quad \forall t \in \mathbb{T} \wedge b, q \in \mathbb{B} \tag{3.41}$$

$$Q_t^{b,g} = Q_t^{b,d} + V_t^b \sum_{q=1}^{B} V_t^q Y^{b,q} Sin(\delta_t^b - \delta_t^q - \theta^{b,q}) \quad \forall t \in \mathbb{T} \wedge b, q \in \mathbb{B} \tag{3.42}$$

It is worth noting that the sub-optimization problems (3.38a) and (3.38b) are solved first to determine the grid power export and import limits at the connection bus $b^*$ (i.e., $P_{t,\text{exp}}^{b^*,\max}$ and $P_{t,\text{imp}}^{b^*,\max}$). These limits are subsequently imposed as fixed constraints, as given in (3.37a) and (3.37b), on the AA-CAES charging and discharging power, thereby capturing the overall impact of the grid.

This decomposition of the original optimization problem into a main problem (3.14) and two sub-optimization problems (3.38a) and (3.38b) enhances the flexibility of the framework and enables both grid operators and private investors to benefit from the proposed formulation. Grid operators typically have access to detailed power system data and can therefore solve the sub-optimization problems to determine the maximum export and import limits. These limits are then incorporated into the main optimization problem to evaluate the feasibility of AA-CAES in enhancing grid resiliency and participating in GSs markets. In contrast, private investors may rely on predetermined export and import limits based on agreements with the system operator. In such cases, they can directly solve the main optimization problem without the need to perform the sub-optimization stage.

## 3.5 Simulation Results

The effectiveness of the proposed optimization model was validated on the modified IEEE 30-bus system [90] shown in Fig. 3.5, where the AA-CAES is connected to bus 15. The component sizing was performed over a full-year dispatch horizon with a one-hour time step to ensure capturing the long- and seasonal-term storage capabilities along with the short-term one. The operational performance of the AA-CAES was evaluated for short-, long-, and seasonal-term storage by considering three representative scheduling horizons of one day, one week, and

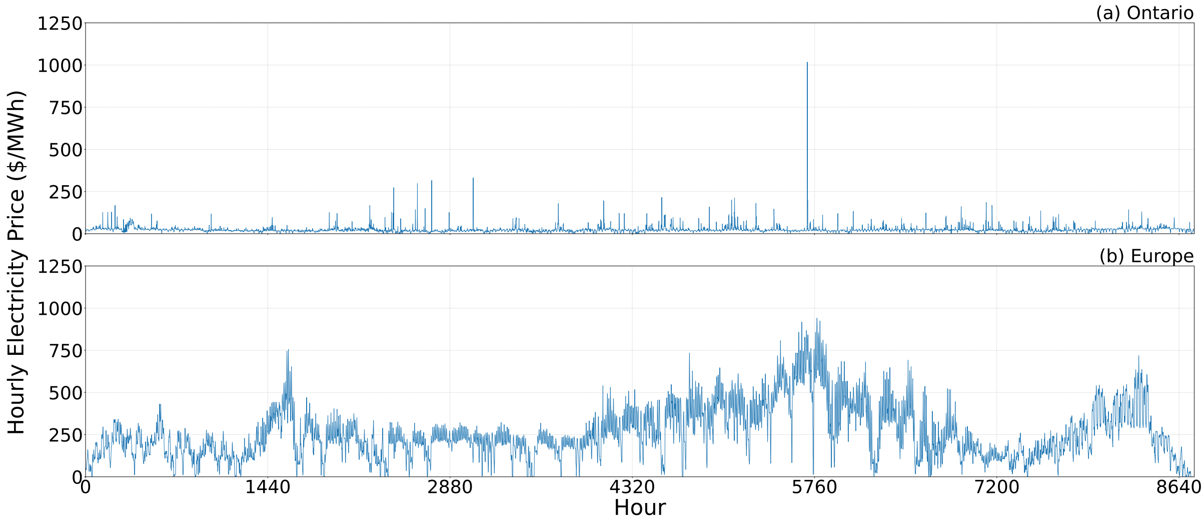


Figure 3.6: Hourly electricity prices: (a) Ontario, and (b) Europe.

one month, respectively. Based on the specified set $\mathbb{T}$, the scheduling horizon was defined dynamically, corresponding to an optimization window of $|\mathbb{T}|$ hours.

To capture the influence of diverse electricity pricing, three representative markets with distinct pricing schemes were analyzed: the provinces of Québec and Ontario in Canada, and the European market. Québec, supported by abundant hydroelectric resources, has a fixed and predictable tariff, enabling a stable flat-rate structure. The electricity system in Ontario relies on a diverse generation mix that includes nuclear, hydroelectric, natural gas, and renewable sources. Under the IESO, Ontario's hourly prices fluctuate in response to market conditions and grid demand, resulting in higher variability and less predictable costs compared to Québec. Extending the comparison beyond Canada, the European market exhibits even stronger variability in electricity prices. This volatility is primarily driven by the high penetration of renewable energy, extensive cross-border electricity trading, and pronounced sensitivity to natural gas prices [91]. The hourly real-time electricity prices and electrical demand data used in this study are obtained from Hydro-Québec [92], the IESO in Canada [93], and [94]. Fig. 3.6 presents the historical hourly electricity prices for Ontario and Europe during 2024, illustrating the high price variability in the European market compared to the relatively more stable structure observed in Ontario, while Québec maintains an even more stable flat-rate tariff of 30 \$/MWh. The corresponding demand data are extracted from publicly available datasets [95]. To represent electricity-price and demand uncertainty, the hourly electricity price and load series were modeled using hour-specific normal probability density functions and discretized into a finite

Table 3.1: Case studies of AA-CAES participation in GSs across markets.

| **GS** | **EA** | | | **EA+OR** | | | **EA+CMDR** | | | **EA+OR+CMDR** | | |
|---|---|---|---|---|---|---|---|---|---|---|---|---|
| **Case** | 1 | 2 | 3 | 4 | 5 | 6 | 7 | 8 | 9 | 10 | 11 | 12 |
| **Market** | QC | ON | EU | QC | ON | EU | QC | ON | EU | QC | ON | EU |

*Note: EU = Europe, ON = Ontario, QC = Québec.*

set of states. These state distributions were then sampled to generate 1000 Monte Carlo scenarios, with each scenario probability computed as the average of the corresponding hourly state probabilities [96].

In each of the three considered markets, four service-participation cases were examined, yielding a total of twelve case studies as summarized in Table 3.1. Specifically, cases 1–3 correspond to participation in EA, cases 4–6 to EA with OR, cases 7–9 to EA with CMDR, and cases 10–12 to EA with both OR and CMDR, evaluated across the three markets—Québec, Ontario, and Europe, respectively. The optimization framework is implemented in Python and solved using Gurobi solver, and simulations are conducted on an Apple M1 Pro workstation with 16 GB RAM.

### 3.5.1 Cases 1–3: AA-CAES Performs Only EA

Cases 1 to 3 consider the AA-CAES performing only EA across Québec, Ontario, and Europe, respectively. The sizes of the AA-CAES components obtained from the optimization model are reported in Table 3.2, where, in cases 1 and 2, the model decided not to allocate AA-CAES. By contrast, in case 3, the compressor and turbine subsystems' rated power, $S^c$ and $S^{tr}$, are found to be 64 MW and 63 MW, respectively, corresponding to rated air mass flow rates of 102 kg/s through the compressors and 167 kg/s through the turbines. Table 3.3 presents the annual economic performance as a detailed breakdown of the objective function components defined in (3.14), including $CapEx$, $OpEx$, $Rev^{EA}$, and the resulting net revenue across markets under both component sizing and operational scheduling horizons. As shown earlier, the Québec and Ontario markets exhibit relatively stable electricity price profiles, making EA performance economically infeasible as the limited arbitrage revenue fails to offset the CapEx and OpEx costs of AA-CAES. As such, there was no allocation of AA-CAES in these markets. In the European

Table 3.2: Optimal component sizing for all case studies.

| **Case** | **1** | **2** | **3** | **4** | **5** | **6** | **7** | **8** | **9** | **10** | **11** | **12** |
|---|---|---|---|---|---|---|---|---|---|---|---|---|
| $S^c$ (MW) | 64 | - | - | 64 | - | - | 23 | 24 | 64 | 23 | 24 | 64 |
| $m_r^c$ (kg/s) | 102 | - | - | 102 | - | - | 37 | 39 | 102 | 37 | 39 | 102 |
| $S^{tr}$ (MW) | 63 | - | - | 72 | - | - | 74 | 76 | 73 | 74 | 76 | 73 |
| $m_r^{tr}$ (kg/s) | 167 | - | - | 191 | - | - | 197 | 202 | 194 | 197 | 202 | 194 |

market, where price variability is substantially higher, EA performance becomes profitable, leading the optimization to allocate AA-CAES.

In case 3, the component sizing results show that both CapEx and OpEx are approximately 4 M$, while the $Rev^{EA}$ exceeds 12 M$, resulting in net revenue exceeding 4 M$, as illustrated in Table 3.3. However, a closer examination of the operational stage reveals that the effectiveness of arbitrage is highly dependent on the length of the scheduling horizon. Under a day-ahead scheduling horizon, the system is unable to make informed charging and discharging decisions due to limited foresight. This, in turn, results in significantly reduced $Rev^{EA}$, and consequently, a negative profit is achieved. In essence, the short horizon prevents the system from exploiting multi-day price variations, resulting in inefficient operation over time. By extending the scheduling horizon, the optimization results progressively converge toward those of the component sizing stage, with the weekly horizon yielding closer alignment and the monthly horizon showing an almost exact match, thereby demonstrating the viability of AA-CAES as a long- and seasonal-term storage technology.

Fig. 3.7 illustrates the electricity price profile and the resulting optimal operations under both day-ahead and weekly scheduling horizons for case 3 over a representative week drawn from the full-year simulation. As shown in Fig. 3.7(b), both horizons successfully capture low electricity price periods to charge the AA-CAES. However, the weekly horizon exhibits a broader charging strategy, leveraging extended foresight to store more energy during favorable price windows. This longer forecasting horizon also enables the weekly strategy to defer discharging to periods with higher electricity prices later in the week. By contrast, the day-ahead horizon, constrained by limited foresight, tends to utilize the stored energy more quickly, initiating discharging earlier in response to short-term price signals.

Table 3.3: Annual economic performance of EA participation across various markets and scheduling horizons.

| **Market (Case)** | **Cost/ Revenue** | **Sizing** | **Operational Scheduling** | | |
|---|---|---|---|---|---|
| | | | **Monthly** | **Weekly** | **Daily** |
| Québec (1) | - | - | - | - | - |
| Ontario (2) | - | - | - | - | - |
| Europe (3) | $CapEx$ (M\$) | 3.976 | 3.976 | 3.976 | 3.976 |
| | $OpEx$ (M\$) | 3.861 | 3.861 | 3.818 | 2.214 |
| | $Rev^{EA}$ (M\$) | 12.755 | 12.755 | 12.106 | 6.111 |
| | Net Revenue (M\$) | 4.917 | 4.917 | 4.311 | -0.07 |

Fig. 3.7(c) presents the corresponding air reservoir pressure profiles. The figure highlights the limited foresight associated with the day-ahead horizon, as well as the more strategic, multi-day utilization enabled by the weekly horizon. Notably, there are periods during which the day-ahead schedule results in neither charging nor discharging. This behavior can be attributed to electricity price fluctuations that are insufficient to justify operation. Specifically, even when minor price variations are present, the expected arbitrage revenue may not offset the round-trip energy losses inherent to AA-CAES components, making charging and discharging economically suboptimal.

These findings yield two key insights. First, long-duration ES technologies such as AA-CAES are economically viable for EA only in markets with high electricity price variability. Second, the AA-CAES system demonstrates greater economic viability over longer operational scheduling horizons (e.g., weekly or monthly), reflecting its enhanced economic feasibility as a long- and seasonal-term ES.

### 3.5.2 Cases 4–6: AA-CAES Performs EA and Participates in OR

Table 3.2 shows that in case 6, the inclusion of OR increases $S^{tr}$ to 73 MW, compared to 63 MW in case 3, thereby enabling the AA-CAES to respond to OR signals during periods of high OR prices. The corresponding rated air mass flow rate through the turbines increases from 167 kg/s to 191 kg/s. In contrast, the $S^{c}$ size remains fixed at 64 MW in both cases.

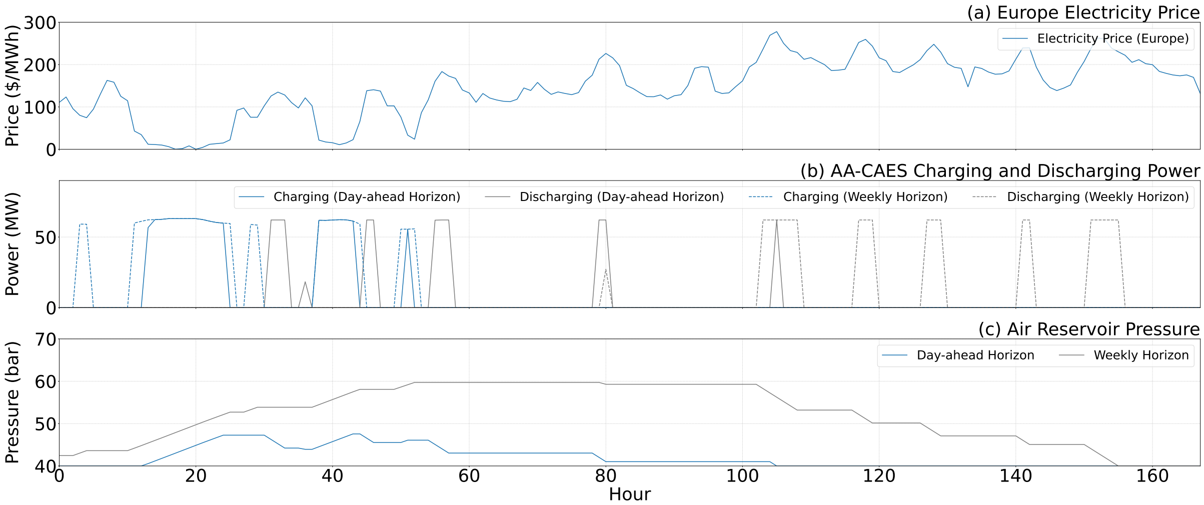


Figure 3.7: Optimal operational scheduling under both day-ahead and weekly scheduling horizons over a representative week in Europe for case 3: (a) Europe electricity price, (b) AA-CAES charging and discharging power, and (c) Air reservoir pressure.

As illustrated in Table 3.4, this increase in $S^{tr}$ leads to a higher $Rev^{EA}$, as it allows the AA-CAES to discharge at greater power. It also generates a modest $Rev^{OR}$ of approximately 0.5 M$. Although relatively small, this additional revenue stream justifies the investment, since the combined increase in CapEx and OpEx from case 3 to case 6 is lower than the sum of $Rev^{OR}$ and the extra revenue gained from the enhanced EA capability.

These findings yield a key insight: participation in OR increases the discharging capacity of the AA-CAES. This is economically beneficial from both the EA and OR perspectives, although the contribution to the net profit remains modest.

### 3.5.3 Cases 7–9: AA-CAES Performs EA and Participates in CMDR

Considering the dependence of CMDR on a predetermined committed capacity rather than fluctuations in electricity prices, participation is feasible in both Canadian and European markets, as shown in Table 3.2. Since EA is not profitable in the Canadian markets, $S^{c}$ is set much lower than $S^{tr}$ in cases 7 and 8, as charging primarily supports CMDR obligations. The discharge capacity is increased to maximize CMDR compensation. In case 9, $S^{tr}$ is further increased by 10 MW compared to the EA-only performance in case 3.

Fig. 3.8 illustrates the optimal operation of the AA-CAES in Ontario for case 8 under two

Table 3.4: Annual economic performance of EA and OR participation across various markets and scheduling horizons.

| **Market (Case)** | **Cost/ Revenue** | **Sizing** | **Operational Scheduling** | | |
|---|---|---|---|---|---|
| | | | **Monthly** | **Weekly** | **Daily** |
| Québec (4) | - | - | - | - | - |
| Ontario (5) | - | - | - | - | - |
| Europe (6) | $CapEx$ (M$) | 4.278 | 4.278 | 4.278 | 4.278 |
| | $OpEx$ (M$) | 4.112 | 3.900 | 3.869 | 2.414 |
| | $Rev^{EA}$ (M$) | 13.174 | 12.418 | 12.060 | 6.413 |
| | $Rev^{OR}$ (M$) | 0.585 | 0.563 | 0.549 | 0.433 |
| | Net Revenue (M$) | 5.368 | 4.802 | 4.461 | 0.153 |

consecutive CMDR events. As shown in Fig. 3.8(a), the availability window coincides with periods of elevated electricity prices. Fig. 3.8(b) demonstrates that the AA-CAES strategically charges prior to the availability window to ensure sufficient stored energy for activation. During the activation window, the system discharges at the committed level while maintaining output above the tolerance threshold in (3.36). In this case, the committed discharge capacity $P^{CMDR}$ was set equal to $S^{tr}$, with the baseline output $P^{STD}$ fixed at zero to maximize economic benefits, as in (3.21). Consequently, no discharging occurred prior to the availability window due to the zero-baseline condition.

The air reservoir pressure shown in Fig. 3.8(c) illustrates how the AA-CAES can handle the worst-case scenario by completing the required charging within the limited time of $t^{CMDR}_{prep,min}$, as specified in (3.34). Under the day-ahead horizon, the system starts at the minimum allowable pressure of 40 bar and completes charging within the minimum preparation period of 17 hours.

Fig. 3.9(a) presents a detailed breakdown of the components of the objective function under EA and CMDR. For cases 7, 8, and 9, the values of $P^{CMDR}$ are identical to the optimal $S^{tr}$ reported in Table 3.2, and their close values result in almost identical $Rev^{CMDR}$. However, the European market exhibits higher CapEx compared to the Canadian markets, owing to the larger $S^{c}$ required for EA. Consequently, $Rev^{EA}$ in Europe is much higher than in Canada, which in turn leads to higher OpEx due to more frequent charging and discharging. It is worth noting

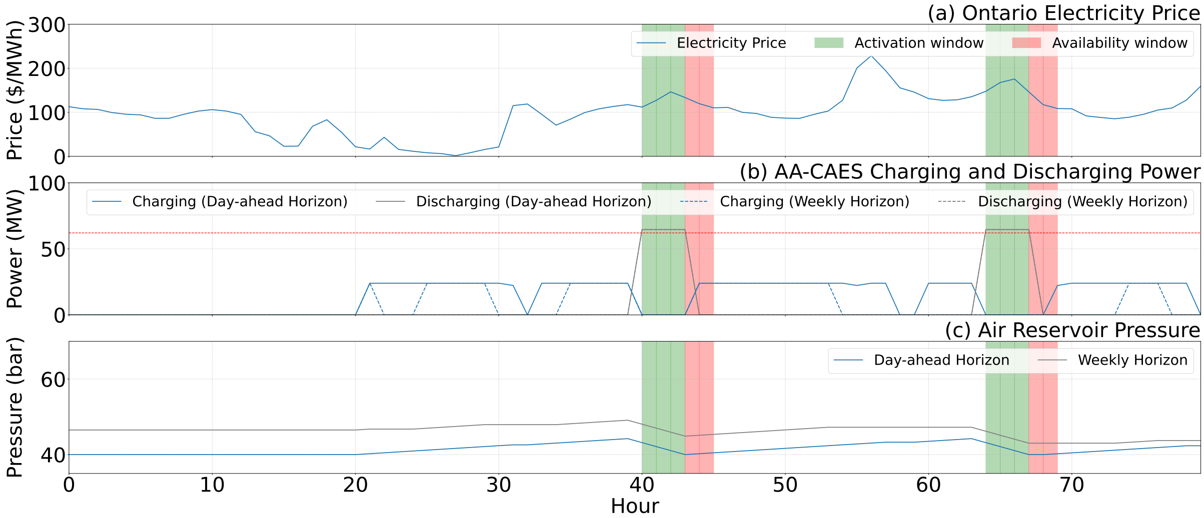


Figure 3.8: Optimal operation in Ontario for case 8 under two consecutive CMDR events (a) Ontario electricity price, (b) AA-CAES charging and discharging power, and (c) Air reservoir pressure.

that in the European market, $Rev^{EA}$ is lower than the case of participating in EA alone, due to the reduced operational flexibility resulting from the obligation to satisfy CMDR requirements. Overall, this results in greater net revenue in Europe. In contrast, $Rev^{EA}$ in the Canadian markets is very low and remains below both CapEx and OpEx, with most of the net revenue generated from CMDR. This observation is consistent with the findings discussed in Sections 3.5.1 and 3.5.2.

These findings yield three key insights. First, AA-CAES can engage in CMDR in both relatively stable-price markets (i.e., Québec and Ontario) and markets characterized by high price variability (i.e., Europe). Second, in markets characterized by high variability, AA-CAES seeks to maximize both charging and discharging capacities to leverage price fluctuations. By contrast, in stable-price markets, AA-CAES can enhance profitability by exploiting the difference between charging and discharging capacities, allocating a smaller capacity for charging and a larger capacity for discharging. This approach maximizes CMDR compensation while minimizing CapEx and OpEx. Third, the CMDR revenue is not a function of the operational scheduling horizon, indicating that engaging in CMDR is feasible for short-, long-, and seasonal-term operations. Hence, in relatively stable-price markets—where significant revenue from EA is not achievable and profitability mainly depends on CMDR revenue—it is recommended to operate the AA-CAES as a short-term storage system and adopt a daily scheduling horizon, since longer

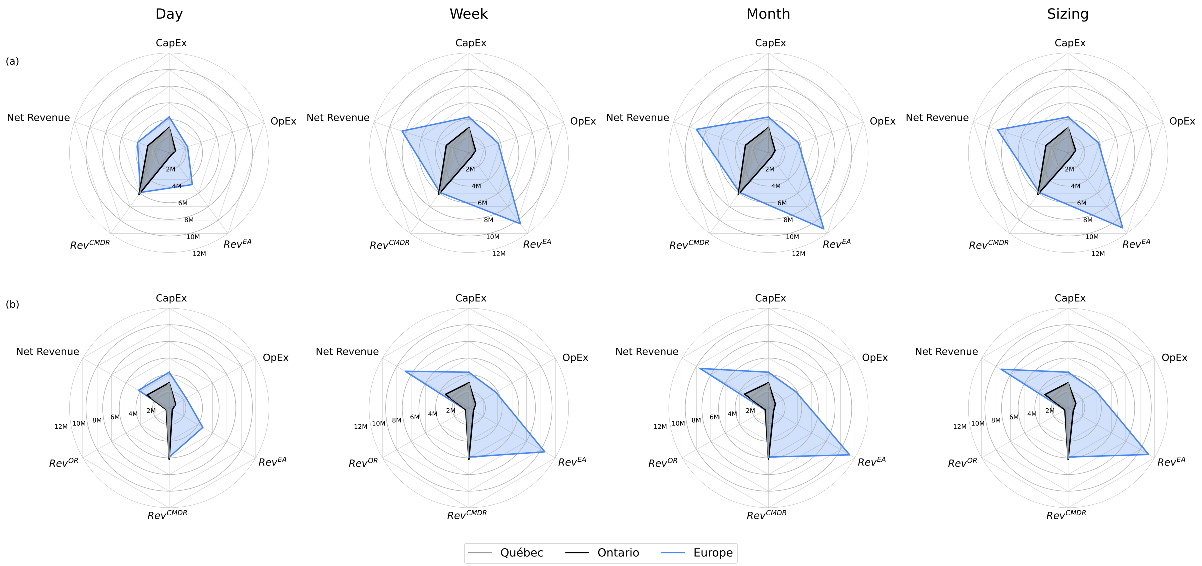


Figure 3.9: Annual economic performance across different markets under both component sizing and operational scheduling horizons (a) for EA with CMDR, and (b) for EA with CMDR and OR.

horizons do not enhance profitability.

### 3.5.4 Cases 10–12: AA-CAES Performs EA and Participates in OR and CMDR

In cases 10–12, the participation of AA-CAES in OR, along with EA and CMDR, yields negligible effects on the component sizing compared to cases 7–9, as given in Table 3.2. In terms of operational scheduling, OR provision in stable-price markets (i.e., Cases 10 and 11) yields modest revenue, unlike Cases 4 and 6, where the AA-CAES was not economically feasible for OR participation. This improvement is mainly attributed to the inclusion of CMDR in Cases 10 and 11, which generated sufficient additional revenue to cover the AA-CAES CapEx and OpEx, thereby enabling the required infrastructure for OR provision. In high-variability markets, performing EA provides the highest revenue, particularly for long- and seasonal-term operation; hence, the AA-CAES achieves nearly the same modest OR revenue in both Case 6—where it performs EA and participates in OR—and Case 12—where it performs EA and participates in both OR and CMDR. Further, comparing Fig. 3.9(b) with Fig. 3.9(a) reveals that AA-CAES participation in OR has only a minor impact on the net revenue compared to CMDR across all markets.

These findings yield a key insight: in stable-price markets, AA-CAES participation in OR must be combined with both EA and CMDR to be economically feasible, whereas in high-variability markets, OR provision can be economically viable when combined with either EA, CMDR, or both.

## 3.6 Chapter Summary

This chapter presents a novel optimization framework for the deployment of grid-connected AA-CAES considering participation in GSs. The framework is developed to optimize the component sizing of the AA-CAES and its short-term, long-term, and seasonal-term dispatch by employing various scheduling time horizons. The objective is to minimize CapEx and OpEx while maximizing net revenue from GSs, considering the thermodynamic characteristics of AA-CAES, the operational requirements of GSs provision, and the power grid operation limits. The proposed model is validated through multiple case studies of EA, OR, and CMDR across diverse electricity markets (i.e., Québec, Ontario, and Europe), each of which has a different electricity pricing scheme. Twelve case studies are conducted, exploring all GSs combinations and highlighting the influence of the electricity pricing schemes and the services' portfolios on optimal component sizing and operation of AA-CAES.

The results revealed that AA-CAES achieves economic viability for performing EA in markets with high price variability (i.e., Europe), especially for long- and seasonal-term operation. In contrast, it is unprofitable in markets with relatively stable prices (i.e., Québec and Ontario). Similarly, participation in OR alongside performing EA is economically feasible only in markets with high price variability; however, it increases discharging capacity, yielding slightly higher economic benefits than performing EA alone. Conversely, CMDR alongside performing EA proves effective for both fixed and variable electricity price markets, with significantly higher profitability in markets with high variability, mainly because of the additional profit achieved from performing EA in high variability markets. Additionally, the revenue of performing EA and OR participation increases proportionally with the scheduling horizon, reflecting the influence of storage duration—whether short-term, long-term, or seasonal-term. Yet, the revenue from CMDR is independent of the scheduling horizon due to CMDR regulations, which require the same capacity to be available on all days throughout the obligation period. Therefore, unlike performing EA and the participation in OR, longer scheduling horizons do not enhance CMDR revenue, indicating that this service is suitable for all storage durations.

Overall, the developed holistic framework can guide both system operators and stakeholders in assessing the suitability of AA-CAES across diverse electricity markets and in providing various GSs over different storage durations.

# Chapter 4

# Optimal Energy Resource Sizing of LEFs Participating in Capacity-Markets Based DR Considering Convex-Relaxed Market Constraints

## 4.1 Nomenclature

### 4.1.1 Sets

$\mathbb{T}_m$ Set of month $m$ time intervals.

$\mathbb{T}_e^{ADJ}$ Set of DR event $e$ adjustment window time intervals.

$\mathbb{T}^{DR}$ Set of DR activation windows time intervals.

$\mathbb{M}$ Set of the planning horizon months.

$N^c$, $N^{tr}$ Set of CAES compressors and turbines.

### 4.1.2 Indices

$t$ Time index.

$m$ Month index.

$e$ DR event index.

$w$ Historical day index.

$n^c$, $n^{tr}$ Indices of CAES compressors and turbines.

### 4.1.3 Parameters

$\Delta t$ Time step duration (hour).

$HEP_t$ Hourly energy price at time $t$ (\$/MWh).

$EA_m$ Energy Adjustment cost at month $m$ (\$/MWh).

$C_1$ Energy regulatory charge (\$/MWh).

$C_2, C_3$ Active/Reactive power delivery charge (\$/MW).

$C_4$ Monthly fixed billing charge (\$).

$PF_m$ Power factor of the LEF in month $m$ (%).

$N$, $W$ Number of highest loads hours and preceding days used in baseline calculation, respectively.

$\delta^{DR}$ Tolerance for demand reduction (%).

$AF_{min}$ Minimum allowable Adjustment Factor (AF) (%).

$AF_{max}$ Maximum allowable AF (%).

$C^s$, $O^s$ CapEx (\$/MW), OpEx (\$/MWh) of unit $s$.

$LT^s$ Lifetime for unit $s$ (years).

$C_m^{CHP}$ CHP monthly CapEx and OpEx (\$/month).

$C^{fuel}$ CHP fuel price (\$/MWh).

$\lambda^{PV}$ Curtailed PV power penalty factor (\$/MWh).

$\text{GHG}_t^{grid}$ Grid GHG emissions at time $t$ (ton/MWh).

$PL^{GHG}$ GHG penalty (\$/ton).

$\alpha_{GHG}^{CHP}$ GHG emission factor of the CHP (ton/MWh).

$C^{DR}$ DR clearing price (\$/MW/business-day).

$N_m^{BD}$ Number of business days in month $m$.

$D^{PV}$ PV drift factor (p.u).

$G_t$ Solar irradiation at time $t$ (kW/m$^2$).

$\alpha^{PV}$ PV alpha factor (1/°C).

$T_t^{PV}$ PV cell temperature at time $t$ (°C).

$T_t^{amb}$ Ambient temperature at time $t$ (°C).

$\alpha_{\min/\max}^{BS}$ Minimum/maximum BES state of charge (%).

$a_0$–$a_5$, $z$ BES degradation model parameters.

$RC$ Residual cost at the end of the BES lifetime.

$\eta_{Ch/Dch}^{BS}$ BES charge/discharge efficiency (%).

$\Delta ID$ BES calendar aging index.

$T_t^{BS}$ BES temperature at time $t$ (°C).

$K$ Boltzmann constant (J/K).

$D_f$ HES hydrogen tank dissipation factor (%/h).

$\rho_H^P$ HES ower-to-hydrogen factor (m$^3$/MWh).

$\eta^{EL}, \eta^{FC}$ HES electrolyzer and fuel cell efficiencies (%).

$\alpha_{\min}^{HT}$ Minimum HES tank state of charge (%).

$\alpha_{\max}^{HT}$ Maximum HES tank state of charge (%).

$\eta^m$, $\eta^g$ CAES motor and generator efficiencies (%).

$\eta^c$ CAES compressor efficiency (%).

$\eta^{tr}$ CAES turbine efficiency (%).

$C_p^a$, $C_p^w$ Specific heat capacity of air and water (J/kg·K).

$r_c$, $r_{tr}$ CAES compression and expansion ratio (p.u).

$\gamma$, $R$ Specific heat ratio, and gas constant (J/kg·K).

$T^r$, $V^r$ Air reservoir temperature and volume (K, m$^3$).

$p^r_{\min}$ CAES air reservoir minimum pressure (bar).

$p^r_{\max}$ CAES air reservoir maximum pressure (bar).

$T^{tr}_{icing}$ Turbine outlet temperature to prevent icing (K).

$P^{grid}_{max}$ Rated capacity of the LEF transformer (MW).

$P^{CHP}_{max}$ Rated capacity of the CHP (MW).

### 4.1.4 Variables

$P^{grid}_t$ Grid power imported at time $t$ (MW).

$P^{peak}_m$ Grid peak power in month $m$ (MW).

$C^{Bill}_m$ Electricity bill in month $m$ (\$).

$P^{STD}_t$ Standard baseline load at time $t$ (MW).

$P^{DR}_{Con}$ Contracted demand reduction (MW).

$AF_e$ DR event $e$ AF (p.u).

$P^{Act}_t$ Adjusted baseline load at time $t$ (MW).

$P^{DR}_t$ Delivered demand reduction at time $t$ (MW).

$S^s$ Optimal sizing decision for unit $s$ (MW).

$P^{CHP}_t$ Power output of the CHP at time t (MW).

$P_t^{PV,Crt}$ PV curtailment power at time $t$ (MW).

$P_t^{PV,M}$ PV maximum power at time $t$ (MW).

$P_t^{PV,U}$ PV utilized power at time $t$ (MW).

$C_t^{BS,cyc}$ BES cycling degradation cost at time $t$ (\$).

$C_t^{BS,cal}$ BES calendar degradation cost at time $t$ (\$).

$P_t^C, P_t^T$ CAES Compressors and turbines power at time $t$ (MW).

$P_t^{EL}$ HES electrolyzer power at time $t$ (MW).

$P_t^{FC}$ HES fuel cell power at time $t$ (MW).

$SoC_t^{BS}$ BES state of charge at time $t$ (MWh).

$P_t^{BS,Ch}$ BES charging power at time $t$ (MW).

$P_t^{BS,Dhg}$ BES discharging power at time $t$ (MW).

$SoC_t^{HT}$ HES tank state of charge at time $t$ (m$^3$).

$p_t^r$ CAES air reservoir pressure at time $t$ (bar).

$\dot{m}_t^c$, $\dot{m}_t^{tr}$ CAES Compressors and turbines air mass flow rates at time $t$ (kg/s).

$p_t^{in}$, $p_t^{de}$ CAES air reservoir pressure increase and decrease at time $t$ (bar).

$T_t^{n^c,in\backslash out}$ Inlet/Outlet air temperature of CAES $(n^c)^{th}$ compressor at time $t$ (K).

$T_t^{n^{tr},in\backslash out}$ Inlet/Outlet air temperature of CAES $\left(n^{tr}\right)^{th}$ turbine at time $t$ (K).

$\dot{m}_t^{HX_w^{n^c\backslash n^{tr}}}$ Water mass flow rate in CAES compressor-side/turbine-side HXs at time $t$ (kg/s).

$T_t^{HX_{w\backslash air}^{n^c\backslash n^{tr}}}$ Water/Air temperature of CAES compressor-side/turbine-side HXs at time $t$ (K).

## 4.2 Introduction

CMDR constitutes the dominant share of aggregated DR capacity, accounting for approximately 70-90% of total DR resources in modern power systems. Despite its critical role in system adequacy and peak load mitigation, CMDR participation, together with its complex baseline formulation, verification procedures, and regulatory rules, has been largely overlooked in the optimal sizing and management of large consumers. This chapter proposes an optimal energy resource planning and management framework for LEFs with onsite energy resources participating in CMDR programs. To address the strong nonlinearity of CMDR rules, a convex relaxation is developed that provides a conservative and reliable estimate of deliverable demand reduction while preserving global optimality. The framework co-optimizes the investment and operation of on-site energy resources, including CHP, PV, and both short and long terms ES technologies: battery, hydrogen, and compressed air. The proposed model integrates CMDR regulations with commercial electricity billing components, capturing key value streams such as capital expenditures, operating costs, EA, peak-demand charge reduction, and DR revenues. The framework accounts for real-time grid GHG emissions to incentivize load reductions that enhance system-wide decarbonization during carbon-intensive periods. The proposed framework is validated on real-world data from York University's Keele campus in Ontario, represented as an LEF with diverse energy loads and assets. The results underscore the critical role of coordinated planning and management of short and long term ES in maximizing arbitrage, reducing peak loads, and supporting reliable DR. The convex relaxation further enables computation times to drop from several hours to milliseconds while keeping the optimality gap below 0.1%.

The main contributions of this work are summarized as follows:

1. An optimal energy resource sizing and management framework is proposed for LEFs participating in the CMDR, explicitly accounting for commercial electricity bill, capacity-market rules, and grid GHG emissions.

2. A convex relaxation of CMDR constraints is introduced to enhance computational efficiency and scalability while guaranteeing global optimality.

3. A comprehensive modeling framework is developed to support multiple short and long terms ES systems in dynamic electricity markets where EA, facility peak reduction, and grid peaks are not aligned.

4. A real-world case study using operational data from York University's campus validates the proposed framework, demonstrating its effectiveness in quantifying both economic and environmental benefits of ES integration and enabling accurate and reliable planning for CMDR participation.

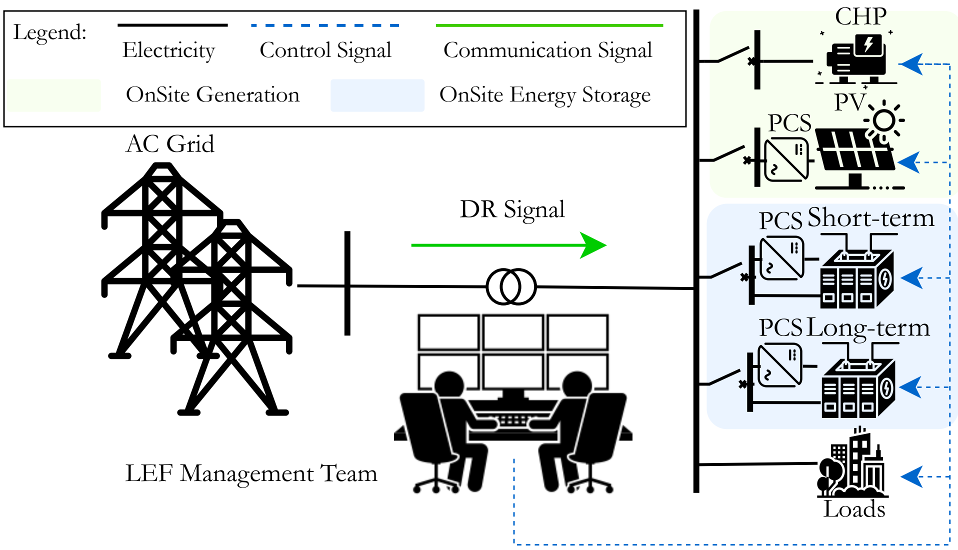


Figure 4.1: Schematic diagram of an LEF connected to the grid.

The remaining sections of this chapter are organized as follows. Section II describes the architect of LEFs, outlines the components of the commercial electricity bill of LEFs, reviews the regulatory rules governing the CMDR, and introduces the proposed convex-relaxation approach. Section 4.4 details the proposed optimal energy resource sizing and management framework. Section 4.5 presents the results together with a comprehensive discussion. Finally, Section 4.6 concludes the chapter and summarizes its main contributions.

## 4.3 Commercial Electricity Billing Structure and Convex Relaxation of DR Capacity-Market rules

This section presents an overview of the LEF structure, highlighting its main components as well as the associated commercial electricity billing. It also discusses the nonconvex market rules governing CMDR participation and introduces the proposed convex relaxation approach.

Fig. 4.1 shows the architecture of a LEF participating in CMDR. The facility contains (i) inherent electrical load and (ii) a portfolio of optional on-site energy resources that may be deployed when justified by economic, environmental, or market participation incentives. These resources differ in dispatch-ability and operational roles and may include CHP, PV generation, and ES technologies (e.g., BES, HES, and CAES storage). PV provides non-dispatchable renewable generation, CHP supplies both heat and electricity, and ES offers dispatchable flexibility.

All assets are assumed to be owned by the facility operator and installed on-site, with PV and ES interfaced to the grid through Power Conversion Systems (PCS). The facility may deploy a single technology or a hybrid combination of energy resources. An internal energy management function schedules resources to supply local demand, minimize operating costs, and commit reliable DR capacity to CMDR. Operational decisions must satisfy market requirements for capacity qualification, availability, and performance, while supporting peak-load reduction, emissions mitigation, and enhanced grid flexibility.

### 4.3.1 Commercial Electricity Billing Structure

The electricity billing structure for LEFs consists of three main components: electricity charges, regulatory charges, and delivery charges. Electricity charges reflect real-time energy costs (i.e., Hourly Electricity Price (HEP)), along with monthly EA. Regulatory charges represent the cost of operating and maintaining the main grid, which calculated using a fixed energy rate. Delivery charges account for the LEFs impact on the grid and it is determined by its peak active and apparent power demand. The mathematical formulation of the monthly electricity bill is provided in (4.1).

$$\begin{aligned} C_m^{Bill} = \sum_{t \in \mathbb{T}_m} (HEP_t + EA_m + C_1) \cdot P_t^{grid} \Delta t \\ +(C_2 + \frac{C_3}{PF_m}) P_m^{peak} + C_4 \end{aligned} \tag{4.1}$$

Electricity charges, together with regulatory charges, are calculated by multiplying the imported grid power $P_t^{grid}$ by the HEP, the EA, and the regulatory energy rate $C_1$. Delivery charges associated with active and reactive power demand are represented by $C_2$ and $C_3$, respectively, where the monthly peak demand is defined using (4.2).

$$P_m^{peak} = max\{P_t^{grid} : \ t \in \mathbb{T}_m\} \tag{4.2}$$

It is worth noting that $C_4$ in (4.1) represents a fixed monthly charge applied for each billing month.

### 4.3.2 Convex Relaxation of DR Capacity-Market Rules

The CMDR process begins with the obligation period, during which prospective participants submit their available demand reduction capacity in MW along with an offered price in \$/MW.

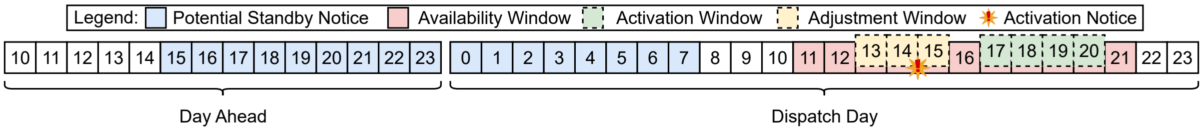


Figure 4.2: CMDR event key milestones and time windows.

Following this, the grid operator publishes the list of awarded providers and the corresponding clearing price. Selected providers are then required to deliver the committed demand reduction during DR activation events in compliance with established market rules and regulations.

Fig. 4.2 illustrates the key milestones and time windows associated with a DR event (e.g., the IESO market in Ontario). The process begins with the issuance of a standby notice by the PSO within a predefined period, typically on the day preceding the event or during the early morning of the event day, to inform participants of a potential activation. The DR activation may occur at any time within the availability window defined by market rules, corresponding to periods when grid peaks are expected. An activation notice is then issued with the required advance notification prior to the start of activation (i.e., at least two hour before activation). Once the DR event begins, it continues over a continuous activation window during which participants must sustain their committed demand reduction (i.e., 2-4 hours). To account for real-time variations in participants' load profiles on the activation day, an adjustment window is defined preceding the activation window, which is used to assess the actual delivered demand reduction. To assess the delivered demand reduction, the grid operator adopts a single-meter baseline approach, in which the demand reduction during a DR event is measured relative to a baseline load profile derived from historical consumption data. At each time instant $t$, the standard baseline is calculated as the average of the highest $N$ load measurements observed at the same time instant over the preceding $W$ days. The mathematical expression of the standard baseline load is given by (4.3).

$$
\begin{aligned}
&P_t^{STD} = \frac{\sum_{v=1}^{v=N} P_{t,v}^{grid}}{N}, \text{ S.t } P_{t,v}^{grid} > P_{t,v+1}^{grid} \\
&\forall\ P_{t,v}^{grid} \in \{P_{t-24\times w}^{gird} : w = 1, .., W\},\ \forall t \in \mathbb{T}^{ADJ} \cup \mathbb{T}^{DR}
\end{aligned}
\tag{4.3}
$$

Here, $P_{t,v}^{grid}$ is a vector containing the recorded load values at time $t$ over the past $W$ days, sorted in descending order.

To address demand uncertainty on the DR event day, an Adjustment Factor ($AF_e$) is determined as the ratio between the present energy consumption and the baseline consumption during the adjustment window, as described by (4.4).

$$AF_e = \frac{\sum_{t\in\mathbb{T}_e^{ADJ}} P_t^{grid} \cdot \Delta t}{\sum_{t\in\mathbb{T}_e^{ADJ}} P_t^{STD} \cdot \Delta t}, \text{ S.t } AF_{min} \leq AF_e \leq AF_{max} \tag{4.4}$$

The $AF_e$ is subsequently applied to scale the baseline load profile during the DR event. Accordingly, the actual baseline load is obtained by multiplying the standard baseline by the computed $AF_e$. The actual baseline is then used by the grid operator to assess whether the participant delivered the committed demand reduction during the DR events. The demand reduction is mathematically expressed by (4.5).

$$P_t^{DR} = P_t^{Act} - P_t^{grid}, \text{ where } P_t^{Act} = AF_e \cdot P_t^{STD}, \; \forall t \in \mathbb{T}^{DR} \tag{4.5}$$

This delivered reduction must adhere to the contracted demand reduction ($P_{Con}^{DR}$) with allowable tolerance ($\delta^{DR}$) as detailed in (4.6).

$$(1-\delta^{DR})P_{Con}^{DR} \leq P_t^{DR} \leq (1+\delta^{DR})P_{Con}^{DR}, \; \forall t \in \mathbb{T}^{DR} \tag{4.6}$$

From the preceding discussion, it is evident that the DR market rules are inherently non-convex, primarily due to the sorting operation of $P_{t,v}^{grid}$ and division operations embedded within the adjustment factor $AF_e$ calculation.

The proposed convex relaxation of the market rule is initially formulated by approximating the standard baseline load at time $t$ using the average of the all $W$ days historical load measurements recorded at the same time instant, defined by (4.7).

$$P_t^{STD} = \frac{\sum_{w=1}^{w=W} P_{t-24\times w}^{gird}}{W}, \; \forall t \in \mathbb{T}^{AD} \cup \mathbb{T}^{DR} \tag{4.7}$$

Under this formulation, the relaxed standard baseline forms a convex lower bound relative to the original non-convex baseline formulation. Accordingly, the demand reduction capacity estimated using this convex baseline remains conservative lower bound that participant can meet.

The $AF_e$ constraint is reformulated as a linear inequality on the total energy consumption within the adjustment window. By enforcing $AF_e$ to be greater than one and bounded by the maximum limit $AF_{\max}$, the actual baseline $P_t^{Act}$ is guaranteed to upper-bound the convex standard baseline $P_t^{STD}$. This condition is satisfied by constraining the energy consumption during the adjustment window to be no lower than the standard baseline, as defined in (4.8).

$$\sum_{t\in\mathbb{T}_e^{ADJ}} P_t^{STD} \leq \sum_{t\in\mathbb{T}_e^{ADJ}} P_t^{grid} \leq AF_{max} \sum_{t\in\mathbb{T}_e^{ADJ}} P_t^{STD} \tag{4.8}$$

The standard convex baseline is then replaced the actual baseline, ensuring that the calculated demand reduction represents a guaranteed lower bound. During the DR activation window, the delivered demand reduction is constrained to remain within the tolerance $\delta^{DR}$ of the contracted DR commitment, as specified in (4.9).

$$(1-\delta^{DR})P^{DR}_{Con} \leq P^{STD}_t - P^{gird}_t \leq (1+\delta^{DR})P^{DR}_{Con},\ \forall\, t \in \mathbb{T}^{DR} \tag{4.9}$$

## 4.4 The proposed Optimal Planning and Management Framework

This section presents the mathematical formulation of the proposed optimal sizing and management framework for LEFs participating in CMDR. It outlines the objective function, sizing and operational decision variables, and the associated constraints governing both short- and long-duration ES technologies.

The proposed framework aims to balance asset investment, operational resource management, and committed demand reduction for LEFs. It optimizes CapEx associated with PV sizing, ES system sizing, and corresponding PCS ratings (i.e., BES, HES, and CAES). From an operational perspective, the framework minimizes OpEx, including the electricity bill and the operating and maintenance costs of both existing assets (i.e., CHP) and newly invested resources (i.e., PV, BES, HES, and CAES), while also reducing environmental impacts by minimizing GHG emissions from grid imports and onsite CHP generation. In addition, the framework determines the optimal contracted demand reduction to maximize CMDR revenue while complying with it market rules described in Section 4.3. The objective function of the proposed framework is given in Eq. (4.10).

$$\text{Minimize}: \sum_{m\in\mathbb{M}} CapEx_m + OpEx_m + R^{DR}_m \tag{4.10}$$

The CapEx captures the levelized investment costs of PV, BES, and their associated PCSs, as well as the CAES compressor and turbine subsystems and the HES electrolyzer, fuel cell, and storage tank, defined by (4.11).

$$
\begin{aligned}
CapEx_m = \frac{1}{12}\Bigg( & \frac{C^{PV}S^{PV}}{LT^{PV}} + \frac{C^{PC}_{PV}S^{PC}_{PV}}{LT^{PC}_{PV}} + \frac{C^{BS}S^{BS}}{LT^{BS}} \\
& + \frac{C^{PC}_{BS}S^{PC}_{BS}}{LT^{PC}_{BS}} + \frac{C^{C}S^{C}}{LT^{C}} + \frac{C^{T}S^{T}}{LT^{T}} + \frac{C^{EL}S^{EL}}{LT^{EL}} \\
& + \frac{C^{FC}S^{FC}}{LT^{FC}} + \frac{C^{HT}S^{HT}}{LT^{HT}} \Bigg)
\end{aligned} \tag{4.11}
$$

The monthly OpEx includes the electricity bill, the operation and maintenance costs of the CHP, PV, and ES components, and the penalty associated with real-time GHG emissions from both the grid and the CHP.

$$
\begin{aligned}
OpEx_m = C^{Bill}_m + C^{CHP}_m + \sum_{t\in\mathbb{T}_m} \Bigg( & C^{fuel} \cdot P^{CHP}_t \\
& + \lambda^{PV} \cdot P^{PV,Crt}_t + O^{PV} \cdot P^{PV,U}_t + C^{BS,cyc}_t \\
& + C^{BS,cal}_t + O^{C} \cdot P^{C}_t + O^{T} \cdot P^{T}_t \\
& + O^{EL} \cdot P^{EL}_t + O^{FC} \cdot P^{FC}_t \\
& + PL^{GHG} \left( GHG^{grid}_t \cdot P^{grid}_t + \alpha^{CHP}_{GHG} P^{CHP}_t \right) \Bigg) \cdot \Delta t
\end{aligned} \tag{4.12}
$$

The monthly Payment from DR is given by (4.13).

$$
R^{DR}_m = C^{DR} \cdot N^{BD}_m \cdot P^{DR}_{Con} \tag{4.13}
$$

It is worth noting that, to comply with CMDR, the objective in (4.10) is subject to the market constraints defined in (4.7)–(4.9). Additionally, the objective function (4.10) is subject to the operational and capacity constraints discussed hereunder.

### 4.4.1 PV Constraints

The maximum PV power output is modeled using Eq.(4.14):

$$
P^{PV,M}_t = D^{PV}\frac{G_t}{G_o}\big(1-\alpha^{PV}(T^{PV}_t - T_o)\big)S^{PV}, \ \forall t \in \mathbb{T}_m \tag{4.14}
$$

where the PV cell temperature is calculated by (4.15) [73].

$$
T^{PV}_t = T^{amb}_t + \frac{G_o}{800}(T_o - 20), \ \forall t \in \mathbb{T}_m \tag{4.15}
$$

The PV power utilized by the LEFs is calculated after accounting for curtailment, as expressed in (5.8).

$$
P^{PV,U}_t = P^{PV,M}_t - P^{PV,Crt}_t, \ \forall t \in \mathbb{T}_m \tag{4.16}
$$

Finally, the PV utilized power is limited by the PCS rating, as defined by (4.17).

$$P_t^{PV,U} \leq S_{PV}^{PC},\ \forall t \in \mathbb{T}_m \tag{4.17}$$

### 4.4.2 BES Constraints

The BES is subject to the State-of-Charge (SoC) energy balance constraints defined by (4.18).

$$SoC_t^{BS} = SoC_{t-1}^{BS} + (\eta_{Ch}^{BS} \cdot P_t^{BS,Ch} - \frac{P_t^{BS,Dhg}}{\eta_{Dhg}^{BS}}) \cdot \Delta t,\ \forall t \in \mathbb{T}_m \tag{4.18}$$

The BES SoC is constrained by upper and lower limits to prevent excessive degradation, as defined in (4.19).

$$\alpha_{min}^{BS} S^{BS} \leq SoC_t^{BS} \leq \alpha_{max}^{BS} S^{BS},\ \forall t \in \mathbb{T}_m \tag{4.19}$$

Additionally, the BES charging and discharging powers are constrained by it is PCS rating as follow:

$$P_t^{BS,Ch}, P_t^{BS,Dhg} \leq S_{BS}^{PC},\ \forall t \in \mathbb{T}_m \tag{4.20}$$

Beside that, the BES charging and discharging operations are restricted to a single mode, as defined in (4.21).

$$P_t^{BS,Ch} \cdot P_t^{BS,Dhg} = 0,\ \forall t \in \mathbb{T}_m \tag{4.21}$$

Finally, the BES cycling and calendar degradation costs are mathematically expressed by (4.22) [73].

$$\begin{aligned} C_t^{BS,cyc} &= (C^{BS}(1-RC))\sqrt{\eta_{Ch}^{BS} \cdot \eta_{Dhg}^{BS}} \\ &\quad \frac{a_0}{[1-SoC_t^{BS}]^z} S^{BS}(1-SoC_t^{BS}),\ \forall t \in \mathbb{T}_m \end{aligned} \tag{4.22}$$

$$\begin{aligned} C_t^{BS,cal} &= (C^{BS}(1-RC))\Delta ID \cdot S^{BS} \\ &\cdot [a_1 e^{(\frac{-a_2+a_3(1-SoC_t^{BS})}{K(T_t^{BS}+273.15)}+a_4(1-SoC_t^{BS}))} - a_5],\ \forall t \in \mathbb{T}_m \end{aligned} \tag{4.23}$$

### 4.4.3 HES Constraints

Similar to the BES, the HES is subject to the SoC energy balance of the hydrogen tank (4.24), SoC operation limits (4.25), and electrolyzer and fuel cell rating limits (4.26) [94].

$$\begin{aligned} SoC_t^{HT} &= (1 - D_f)SoC_{t-1}^{HT} + \rho_H^P \bigg( \eta^{EL} \cdot P_t^{EL} \\ &\quad - \frac{P_t^{FC}}{\eta^{FC}} \bigg) \cdot \Delta t, \ \forall t \in \mathbb{T}_m \end{aligned} \tag{4.24}$$

$$\alpha_{min}^{HT} S^{HT} \leq SoC_t^{HT} \leq \alpha_{max}^{HT} S^{HT}, \ \forall t \in \mathbb{T}_m \tag{4.25}$$

$$P_t^{EL} \leq S^{EL}, P_t^{FC} \leq S^{FC}, \ \forall t \in \mathbb{T}_m \tag{4.26}$$

### 4.4.4 CAES Constraints

The CAES is modeled using advanced adiabatic technology, assuming ideal-gas air behavior, an isothermal reservoir, and adiabatic TES [84], [85]. The system consists of a motor, multi-stage compressors, an air reservoir, multi-stage turbines, a generator, HXs, and a TES unit. The compressors and turbines power is calculated using Eqs. (4.27)-(4.28).

$$P_t^C = \frac{1}{\eta^m \eta^c} C_p^a \sum_{n^c \in N^c} \left( r_c^{\frac{\gamma-1}{\gamma}} - 1 \right) T_t^{n^c,in} \cdot \dot{m}_t^c, \ \forall t \in \mathbb{T}_m \tag{4.27}$$

$$P_t^T = \eta^g \eta^{tr} C_p^a \sum_{n^{tr} \in N^{tr}} \left( 1 - r_{tr}^{\frac{1-\gamma}{\gamma}} \right) T_t^{n^{tr},in} \cdot \dot{m}_t^{tr}, \ \forall t \in \mathbb{T}_m \tag{4.28}$$

where the efficiencies of the compressors $\eta^c$ and turbines $\eta^{tr}$ are calculated using empirical correlations given by (4.29) [86].

$$\eta^c = 0.91 - \frac{r_c - 1}{300}, \quad \eta^{tr} = 0.90 - \frac{r_{tr} - 1}{250} \tag{4.29}$$

The compressors and turbines power are constrained by their rating using (4.30).

$$P_t^C \leq S^C, \quad P_t^T \leq S^T, \ \forall t \in \mathbb{T}_m \tag{4.30}$$

The outlet air temperatures of the $(n^c)^{th}$ compressor and the $\left(n^{tr}\right)^{th}$ turbine are defined by Eqs.(4.31)–(4.32) [19].

$$T_t^{n^c,out} = \left[ 1 + \frac{1}{\eta^c} \left( r_c^{\frac{\gamma-1}{\gamma}} - 1 \right) \right] T_t^{n^c,in}, \ \forall t \in \mathbb{T}_m \tag{4.31}$$

$$T_t^{n^{tr},out} = \left[ 1 - \left( 1 - r_{tr}^{\frac{1-\gamma}{\gamma}} \right) \eta^{tr} \right] T_t^{n^{tr},in}, \ \forall t \in \mathbb{T}_m \tag{4.32}$$

The turbine's mechanical reliability is ensured by constraining the outlet air temperature to remain above the icing threshold, as defined in (4.33).

$$T_t^{n^{tr},out} \geq T_{icing}^{tr}, \ \forall t \in \mathbb{T}_m \tag{4.33}$$

The heat exchange between the air and the heat storage medium on the compression side is governed by HX energy balance using (4.34) [21].

$$\begin{aligned} &= \dot{m}_t^c C_p^a (T_t^{n^c,out} - T_t^{HX_a^{n^c,out}}) = \\ &\dot{m}_t^{HX_w^{n^c}} C_p^w (T_t^{HX_w^{n^c,out}} - T_t^{HX_w^{n^c,in}}), \ \forall t \in \mathbb{T}_m \end{aligned} \tag{4.34}$$

Similarly, on the expansion side, the HX energy balance is defined by (4.35).

$$\begin{aligned} &\dot{m}_t^{tr} C_p^a (T_t^{n^{tr},in} - T_t^{HX_a^{n^{tr},in}}) = \\ &\dot{m}_t^{HX_w^{n^{tr}}} C_p^w (T_t^{HX_w^{n^{tr},out}} - T_t^{HX_w^{n^{tr},in}}), \ \forall t \in \mathbb{T}_m \end{aligned} \tag{4.35}$$

Assuming that the air-to-water mass flow rate ratio equals $C_p^w / C_p^a$, an adiabatic heat exchange with comparable temperature variation between the two fluids is achieved. Using Eqs. (4.34)–(4.35), the following temperature relationships hold [21].

$$T_t^{n^c,in} = T_t^{amb}, \qquad T_t^{n^{tr},in} = T_t^{n^c,out}, \ \forall t \in \mathbb{T}_m \tag{4.36}$$

The rate of pressure increase due to compressors injection is modeled by (4.37).

$$p_t^{in} = \frac{RT^r}{V^r} \dot{m}_t^c, \ \forall t \in \mathbb{T}_m \tag{4.37}$$

Similarly, the rate of pressure decrease due to turbines release is modeled by (4.38).

$$p_t^{de} = \frac{RT^r}{V^r} \dot{m}_t^{tr}, \ \forall t \in \mathbb{T}_m \tag{4.38}$$

Finally, the total reservoir pressure $p_t^r$ is updated using the corresponding increase and decrease rates, which represent the energy state at each time step [19], as expressed in (4.39).

$$p_t^r = p_{t-1}^r + (p_t^{in} - p_t^{de}) \cdot \Delta t, \ \forall t \in \mathbb{T}_m \tag{4.39}$$

Meanwhile, the air reservoir pressure is subject to the safe operation limits as defined in (4.40).

$$p_{min}^r \leq p_t^r \leq p_{max}^r, \ \forall t \in \mathbb{T}_m \tag{4.40}$$

### 4.4.5 LEF Power Balance Constraints

In order to ensure the supply of the LEF demand, the LEF is subject to the power balance equality constraint defined by (4.41).

$$\begin{aligned} & P_t^{grid} + P_t^{CHP} + P_t^{PV,U} + P_t^{BS,Ch} - P_t^{BS,Dhg} \\ & + P_t^{EL} - P_t^{FC} + P_t^{C} - P_t^{T} - P_t^{L} = 0, \ \forall t \in \mathbb{T}_m \end{aligned} \tag{4.41}$$

Finally, both grid power, LEF peak power, and CHP are limited by the the substation transformer rating, and CHP rating, respectively as shown in (4.42).

$$P_t^{grid}, P_m^{peak} \leq P_{max}^{grid}, \quad P_t^{CHP} \leq P_{max}^{CHP}, \ \forall t \in \mathbb{T}_m \tag{4.42}$$

## 4.5 Results and Discussion

This section evaluates the performance of the proposed optimal sizing and management framework incorporating a convex relaxation of capacity-market rules. It first demonstrates the convex relaxation in estimating a conservative lower bound on contracted demand reduction, ensuring global optimality while significantly reducing computational effort. It then assesses the financial and environmental impacts of integrating hybrid short and long terms ES systems and renewable generation, both with DR-enabled and no-DR participation, to identify optimal resource combinations.

The proposed framework is validated using real-world data from York University and the Ontario grid, including demand profiles, DR activation and testing signals, HEP and EA prices, and real-time grid GHG emissions. The dataset spans from May 2022 to May 2023 with a 1-hour time resolution. York University is supplied by the main grid through campus substations rated at 26 MVA and a local CHP plant with a total capacity of 10.4 MW, of which 38% serves electrical loads and 62% is allocated to thermal loads.

### 4.5.1 Impact of CMDR Rule Modeling and Convex Relaxation

Table 4.1 summarizes the performance of the proposed framework without CMDR market rules and with CMDR rules under both nonconvex and convex formulations. In the absence of market rules, a traditional two-meter configuration is assumed, following prior studies, where one meter measures actual demand and the other measures grid power [73]. Under this assumption,

Table 4.1: Impact of convex relaxation of DR capacity-market rules on optimality and computational performance

<table>
<tr><th colspan="2">Aspect</th><th>$P_{Con}^{DR}$ (MW)</th><th>Obj. (M$)</th><th>Gap (%)</th><th>Comp. Time</th></tr>
<tr><td>Without CMDR Rules</td><td>Two-meter</td><td>3.952</td><td>7.127</td><td>$\leq 0.01$</td><td>0.06 sec</td></tr>
<tr><td rowspan="2">With CMDR Rules</td><td>Non Convex</td><td>3.043</td><td>7.379</td><td>$\leq 0.01$</td><td>15-17 hrs</td></tr>
<tr><td>Convex</td><td>1.518</td><td>7.482</td><td>1.39</td><td>0.11 sec</td></tr>
</table>

the contracted DR reduction is overestimated at 3.9 MW, as the calculation implicitly attributes available CHP generation to demand reduction by assuming full CHP utilization during DR activation periods. However, applying this value under CMDR rules results in an infeasible solution, indicating that such overestimation exposes participants to penalty risks and potential forfeiture of DR revenue. This outcome arises because historical CHP utilization influences the achievable demand reduction in future events and must be explicitly considered in the management framework.

When CMDR rules are enforced, the contracted DR reduction is significantly lower because the formulation explicitly incorporates historical baseline calculations. Under these conditions, the nonconvex formulation yields a contracted reduction of 3 MW, while the convex formulation results in 1.5 MW. This difference arises for two main reasons. First, existing market rules, represented by the nonconvex formulation, may be exploited by increasing the AF, for example by temporarily reducing CHP operation during the adjustment window and restoring it during the activation window, which inflates the actual baseline used for DR evaluation. In contrast, this behavior does not occur under the convex-relaxation formulation, as the actual baseline is replaced by the standard baseline, eliminating the possibility of artificially inflating demand reduction. By anchoring the evaluation to the standard baseline, the convex formulation provides a more conservative and reliable estimate of contracted DR capacity and prevents exploitation of CMDR market rules. Second, the proposed convex relaxation provides a guaranteed lower bound on achievable demand reduction, ensuring that the committed capacity can be delivered

Table 4.2: Financial and Environmental Improvements Due to BES, HES, and CAES Installations

| Metric | Base Case | BES | | | | HES | | | | CAES | | | |
|---|---|---|---|---|---|---|---|---|---|---|---|---|---|
| | | Scenario 1 | | Scenario 2 | | Scenario 1 | | Scenario 2 | | Scenario 1 | | Scenario 2 | |
| | | No-DR | DR-Enabled | No-DR | DR-Enabled | No-DR | DR-Enabled | No-DR | DR-Enabled | No-DR | DR-Enabled | No-DR | DR-Enabled |
| Total Energy (GWh) | 66.67 | 67.19 | 67.40 | 67.28 | 67.48 | 67.19 | 67.53 | 67.38 | 67.78 | 67.36 | 67.46 | 67.42 | 67.51 |
| Average Peak Load (MW) | 7.42 | 5.93 | 6.24 | 5.75 | 6.08 | 5.82 | 5.97 | 5.59 | 5.78 | 4.59 | 4.91 | 4.54 | 4.90 |
| Total Electric Bills (M$) | 4.79 | 4.39 | 4.58 | 4.34 | 4.51 | 4.52 | 4.73 | 4.48 | 4.66 | 4.19 | 4.33 | 4.18 | 4.33 |
| Total Cost (M$) | 7.50 | 7.34 | 7.13 | 7.34 | 7.12 | 7.40 | 7.25 | 7.41 | 7.24 | 7.12 | 6.93 | 7.13 | 6.92 |
| Levelized CapEx (M$) | - | 0.17 | 0.17 | 0.21 | 0.21 | 0.15 | 0.15 | 0.19 | 0.19 | 0.05 | 0.05 | 0.06 | 0.06 |
| Cost Saving (M$) | - | 0.16 | 0.36 | 0.15 | 0.38 | 0.11 | 0.25 | 0.10 | 0.27 | 0.38 | 0.58 | 0.38 | 0.58 |
| Total GHG Emissions (ton) | 14158.2 | 14326.5 | 14081.02 | 14383.92 | 14170.38 | 14240.74 | 13813.06 | 14279.48 | 13957.42 | 14561.23 | 14310.24 | 14583.07 | 14279 |

under worst-case operating conditions.

From the computational perspective, the nonconvex formulation requires 15–17 hours to converge, whereas the convex formulation converges in 0.11 s. This substantial reduction in the computation time results from eliminating sorting and division operations in Eqs. (4.3)-(4.4) and replacing them with convex linear equality and inequality constraints, which enables faster convergence to a globally optimal solution. This fast computational performance enables the facility operator to evaluate multiple sizing and management scenarios, such as different resource configurations and clearing prices within the limited obligation period during which CMDR offers must be submitted. From an objective value perspective, the convex relaxation exhibits a 1.39% gap relative to the nonconvex formulation, primarily because artificial demand reduction inflates DR payments without providing actual reductions. When this behavior is eliminated by accounting for true demand reduction, the gap decreases to less than 0.1%, demonstrating the effectiveness of the convex formulation in providing a near-optimal solution to the original nonconvex problem.

### 4.5.2 Financial and Environmental Impacts of ES and Renewable Generation

To evaluate the financial and environmental impacts of integrating different energy resources at the York campus under CMDR participation, five case studies are analyzed across two scenario sets. The studies examine short-term ES (BES), long-term ES (HES and CAES), and hybrid ES technologies combined with PV generation. In both scenario sets, results are evaluated for two operating modes: when the facility is not DR-enabled and when it is DR-enabled. In the first scenario set, optimal sizing of energy resources is performed without considering CMDR participation, while the second scenario set incorporates the facility's participation in the CMDR during the optimal sizing process.

#### 4.5.2.1 BES Installation

When the DR participation is not considered in the optimal resource sizing phase of the facility, the BES is sized at 11.51 MWh with a 2.39 MW PCS, enabling a contracted demand reduction of 3.45 MW when the facility switches to the DR-enabled mode. When DR participation is taken into account as an additional revenue stream during the energy resource planning phase, the BES size increases to 14.87 MWh with a 2.66 MW PCS, allowing a contracted reduction of 3.72 MW. The increase in the BES and PCS sizes is driven by higher expected profits due to the increased demand reduction and associated DR payments. However, these additional profits depend on consistent DR offers and sustained profitability over the BES lifetime. Table 4.2 summarizes the financial and environmental metrics when individual ES resources (BES, HES, and CAES) are deployed compared to the base case without energy resources. As shown in the table, BES installation increases total facility energy consumption compared to the base case due to round-trip efficiency losses incurred during charging and discharging. However, the facility peak load is reduced by an average of 1.33 MW in Scenario 1 and 1.5 MW in Scenario 2, resulting in significant economic benefits through reduced delivery charges and(EA revenues. A consistent observation across all BES cases is that the facility average peak load increases when it operates in the DR-enabled mode. This occurs because BES resources serve both facility peak reduction (to lower delivery charges) and committed DR obligations, and since facility peaks and grid peaks are not coincident a trade-off emerges between the two objective terms.

Overall, the BES reduced electricity costs by \$210–450K over the 13-month study period. In Scenario 1, cost savings increased from \$160K without DR participation to \$360K with DR participation. In Scenario 2, the higher BES investment resulted in \$150K savings in case of no-DR contract, which increased to \$380K under DR-enabled. The table also shows that BES had a minimal impact on the GHG emissions, with variations ranging about $\pm 2\%$ of the base case. This limited change is primarily due to the campus's reliance on low-cost CHP cogeneration and the relatively low GHG emissions cost.

#### 4.5.2.2 HES Installation

In Scenario 1, the optimal sizing of the HES electrolyzer and fuel cell were found to be 0.19 MW and 2.21 MW, respectively, with a hydrogen storage tank of 13,453.564 $m^3$, enabling a CMDR capacity of 2.77 MW. In Scenario 2, these sizes increased to 0.39 MW and 2.44 MW for the electrolyzer and fuel cell, respectively, with the tank volume rising to 18,762.4643 $m^3$, achieving a CMDR capacity of 2.96 MW. The higher ratings reflect the increased CMDR capacity possible under DR-enabled planning. The electrolyzer rating remains lower than the fuel cell, emphasizing its role in long-duration energy storage and short-period discharge to support facility peak reduction and meet CMDR commitments. As shown in Table 4.2, HES installation increases total energy consumption compared to the base case and BES, especially under DR-enabled condition. This is primarily due to the lower round-trip efficiency of HES, resulting in higher energy losses. However, peak load is reduced by an average of 1.52 MW in Scenario 1 and 1.73 MW in Scenario 2, significantly lowering delivery charges. These results highlight the long-duration capability of HES to store energy and deliver high power over short periods.

Despite significant peak-load reductions, the total electricity bill in the case of HES deployment remains higher than BES due to its limited arbitrage capability compared to short-term technologies. In Scenario 1, HES achieved \$110K in cost savings, increasing to \$250K with DR-enabled. In Scenario 2, the slightly higher HES investment yielded \$100K savings under no-DR, rising to \$270K when DR-enabled was included. Although HES investment costs are lower than BES, the resulting cost savings are also smaller. Combined with the smaller CMDR capacity, these results indicate that HES investment is primarily motivated by peak-load shaving and thus delivery-charge reduction, rather than EA or CMDR participation. Due to it is high energy loss, extra energy cost can offset CMDR incentives. Environmentally, HES provides greater GHG-emission reductions than BES, particularly with DR-enabled which shifts consumption away from grid peak-demand periods typically supplied by gas-fired generation.

#### 4.5.2.3 CAES Installation

CAES exhibits behavior similar to HES, with increased discharging capacity and reduced charging capacity. Without DR participation in optimal planning, and with an air reservoir of 24,000 $m^3$, the compressor and turbine were rated at 1.02 MW and 3.74 MW, achieving a CMDR capacity of 3.07 MW. In case of DR-enabled, the reservoir volume remained the same, while the rated powers increased to 1.11 MW and 4.31 MW, raising the CMDR capacity to

Table 4.3: Financial and Environmental Impacts of Aggregated ES Installations With and Without PV

| Metric | Base Case | BES, HES, and CAES | | | | BES, HES, CAES, and PV | | | |
|---|---|---|---|---|---|---|---|---|---|
| | | Scenario 1 | | Scenario 2 | | Scenario 1 | | Scenario 2 | |
| | | No-DR | DR-Enabled | No-DR | DR-Enabled | No-DR | DR-Enabled | No-DR | DR-Enabled |
| Total Energy (GWh) | 66.67 | 67.43 | 67.53 | 67.54 | 67.67 | 60.32 | 60.33 | 60.50 | 60.52 |
| Average Peak Load (MW) | 7.42 | 4.50 | 4.86 | 4.38 | 4.81 | 3.61 | 4.05 | 3.59 | 4.04 |
| Total Electric Bills (M$) | 4.80 | 4.16 | 4.28 | 4.11 | 4.24 | 3.21 | 3.43 | 3.20 | 3.42 |
| Total Cost (M$) | 7.50 | 7.12 | 6.92 | 7.13 | 6.91 | 6.91 | 6.77 | 6.91 | 6.77 |
| Levelized CapEx (M$) | - | 0.08 | 0.08 | 0.12 | 0.12 | 0.77 | 0.77 | 0.78 | 0.78 |
| Cost Saving (M$) | - | 0.38 | 0.59 | 0.38 | 0.59 | 0.60 | 0.73 | 0.60 | 0.73 |
| Total GHG Emissions (tons) | 14158.20 | 14599.81 | 14415.23 | 14639.71 | 14508.94 | 14192.08 | 13747.70 | 14237.23 | 13815.12 |

3.24 MW.

As shown in Table 4.2, CAES delivers significant financial benefits while affecting total energy consumption and emissions. Although more efficient than HES, CAES consumes more energy due to larger compressor and turbine ratings. Its high turbine capacity enabled average peak-load reductions of 2.17 MW in Scenario 1 and 2.20 MW in Scenario 2, leading to substantial delivery-charge savings and overall bill reductions of \$470K–\$620K over the study period. Combined with low installed energy-capacity costs and long system lifetime, total savings reached \$380K, increasing to \$580K with DR participation. These results highlight that investment in long-duration ES technologies, such as HES and CAES, is primarily driven by peak-load and delivery-charge reduction, which can also enhance CMDR revenues. CAES slightly increases GHG emissions due to higher energy throughput compared to HES and lower efficiency relative to BES.

#### 4.5.2.4 BES, HES, and CAES Installation

The case studies highlight that short-term BES excels at EA but its high energy cost (\$/MWh) limits its use for sustained DR reduction. In contrast, long-term HES and CAES are effective for maintaining high DR reductions over extended periods, but low round-trip efficiency limits EA. Therefore, an optimal combination of short- and long-term ES can maximize cost savings from arbitrage, peak-demand reduction, and capacity-market DR payments.

With aggregated ES installations (BES, HES, and CAES), the planning results allocate no HES capacity, indicating BES and CAES are the preferred combination due to CAES's higher round-trip efficiency and lower energy cost. Without DR participation, BES is sized at 2.24 MWh with 0.41 MW PCS, while CAES (24,000 $m^3$ air reservoir) has compressor and turbine ratings of 0.98 MW and 3.46 MW, respectively, achieving a contracted DR reduction of 3.12 MW. With DR participation, BES increases to 5 MWh and 1.01 MW PCS, while CAES capacities slightly decrease to 0.91 MW and 3.43 MW, raising the contracted DR reduction to 3.34 MW. Compared to standalone BES, its size decreases, focusing on EA, while CAES provides peak-load reduction and meets DR commitments. Table 4.3 summarizes the financial and environmental impacts, showing that CAES dominates the high-power DR contribution, with BES providing complementary short-duration flexibility. These results align with the standalone CAES trends in Table 4.2.

#### 4.5.2.5 BES, HES, CAES, and PV Installation

With PV integration, the aggregated planning again allocates no HES capacity, confirming BES and CAES as the preferred storage combination. In Scenario 1, BES is 2.65 MWh with 0.61 MW PCS, and PV is 4.50 MW with 5 MW PCS, while CAES has compressor and turbine ratings of 0.81 MW and 3.81 MW, achieving a CMDR capacity of 2.78 MW. In Scenario 2, BES increases to 3.75 MWh with 0.80 MW PCS, PV slightly decreases to 4.41 MW (PCS unchanged), and CAES capacities change minimally: compressor 0.82 MW, turbine 3.77 MW. The larger BES emphasizes short-duration flexibility for PV excess utilization, while CAES continues to support peak-load mitigation. The CMDR capacity rises slightly to 2.82 MW but remains below the non-PV aggregated case, as reduced grid reliance limits achievable demand reduction. PV integration substantially reduces total energy consumption compared to the base case and other scenarios by decreasing reliance on grid electricity. This lowers the average monthly peak load and electricity bill, leading to significant cost savings. However, these benefits require a higher upfront investment for the added PV capacity. Environmentally, PV reduces GHG emissions, though the impact is limited since CHP cogeneration still dominates overall emissions.

Figure 4.3 illustrates the energy management system performance in Scenario 2 when participating in a CMDR program over a 5-day period. The first graph presents the power analysis, including load, grid, CHP, and PV generation. The second graph shows the real-time HEP, GHG emissions, and the grid and CHP energy price, which explains the energy management system's decision-making process. The third graph shows the BES SoC management, ensuring

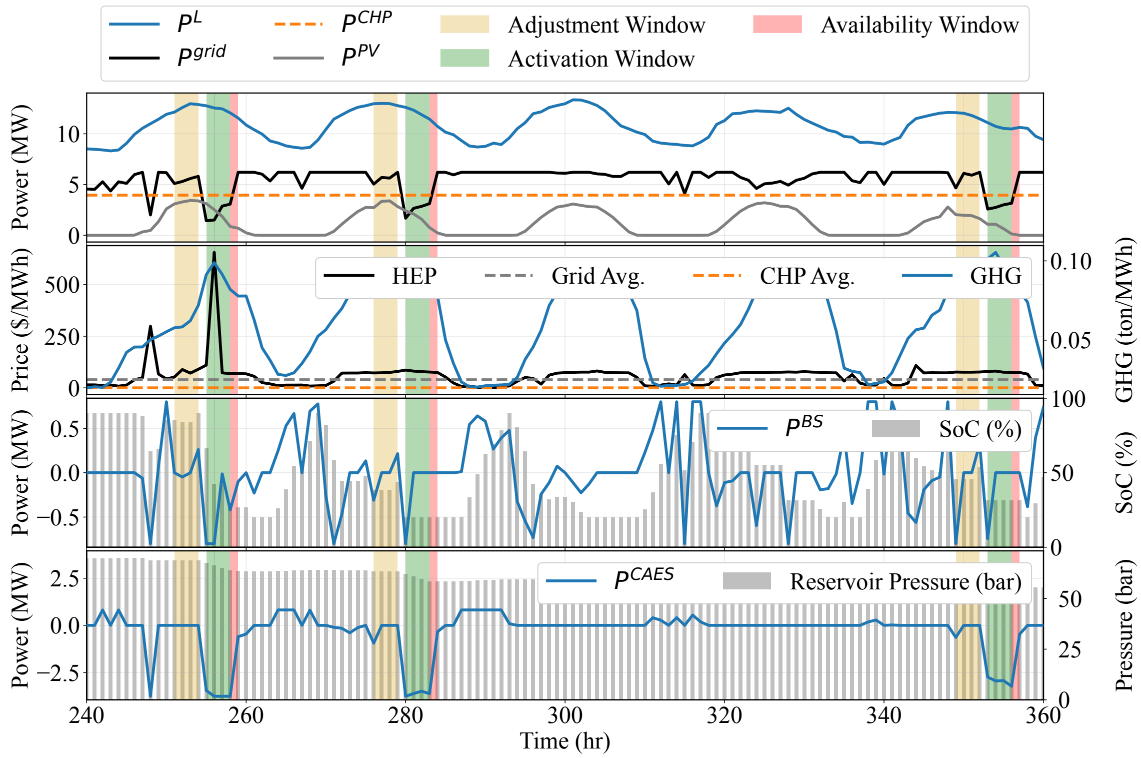


Figure 4.3: Optimal Management performance of the proposed framework during DR events.

safe operation within the 20% to 90% range and avoiding excessive charging and discharging. The last graph shows the CAES management by maintaining the air reservoir pressure between 40 and 70 bar. It is evident that the middle of the day coincides with high demand, PV generation, HEP, and GHG emissions, and the DR events activation also occurs during this period. The CHP operates for most of the time since it is energy cost is about one-third of the grid energy cost. Overall, the energy management system balances financial and environmental priorities by leveraging the synergistic capability of the short-term BES and long-term CAES. The BES typically charges when the HEP is low and discharges when prices are high (i.e., compared to average grid price), leveraging EA, while it also discharges during periods of high grid GHG emissions and high demand to reduce environmental impact and help reduce the overall peak load. The BES contributes to CMDR participation by charging during the adjustment window to increase grid power consumption or discharging during the event to decrease grid consumption. The CAES provides the significant power required during DR activation, leveraging its sustained energy and high discharge capability, and it also charges during periods of low HEP, low GHG emissions, and low demand.

## 4.6 Chapter Summary

This chapter introduces a novel framework for the optimal sizing and management of LEFs, simultaneously optimizing financial performance and environmental impact, while considering CMDR participation. The framework incorporates commercial electricity billing, DR capacity-market rules, and real-time grid GHG emissions to mitigate peak-demand periods dominated by gas-fired generation. A key contribution is the convex relaxation of CMDR rules, which reduces computation time from 17 h to 0.11 s while maintaining global optimality with an optimality gap below 0.1% and ensuring regulatory compliance. Validation with real-world data from York University's campus demonstrates the framework's effectiveness. Case studies assess the financial and environmental impacts of short-term BES, long-term HES and CAES, and hybrid ES technologies co-located with PV generation. Results highlight the complementary roles of short- and long-term ES in meeting LEF operational requirements, achieving substantial cost savings with minimal GHG emission changes. These benefits arise from charging ES during low-cost, low-emission periods and discharging during peak-demand hours, while responding to DR signals to maximize CMDR capacity and overall system performance.

# Chapter 5

# Tri–stage Optimization Framework for Optimal Clustering of PDSs Into Sustainable Microgrids

## 5.1 Introduction

Decentralized sustainable microgrids are emerging as a promising approach for addressing the increasing complexity of modern power systems while ensuring reliable and efficient operation. A fundamental driver of this transition is the partitioning of distribution networks into self-sufficient microgrids supported by the effective integration of DERs and ES systems, enabling improved power flow management and enhanced voltage stability. In this regard, this chapter proposes a tri-stage optimization framework designed to segment power distribution systems into multiple self-sustaining microgrids while maintaining optimal network performance. In the first stage, the distribution grid is partitioned into microgrid clusters based on electrical distance metrics and bus correlation analysis. The second stage focuses on the optimal sizing and operational management of DERs and ES systems within each identified microgrid to ensure energy self-sufficiency and minimize GHG emissions. In the third stage, an optimal resource allocation strategy is implemented, where the resources determined in the previous stage are optimally placed within the distribution network to achieve optimal power flow, reduce system losses, and maintain voltage stability under worst-case operating conditions. The proposed framework is validated using the IEEE 33-bus test system. Simulation results demonstrate

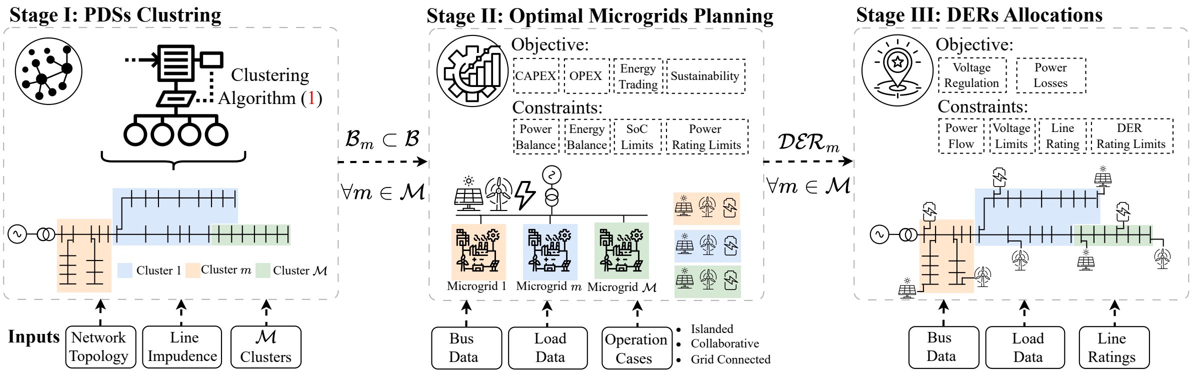


Figure 5.1: The proposed tri-stage framework for PDSs clustering and planning.

its effectiveness in multi-microgrid classification, coordinated planning, and resource allocation, highlighting its superiority in enhancing system performance and resilience.

The main contributions of the proposed framework can be summarized as follows:

1. The development of an electrically grounded hierarchical clustering approach that accurately partitions PDSs into sustainable and collaborative microgrids;
2. A comprehensive co-optimization of DER planning and microgrid clustering that supports both predefined and expandable resource capacities for long-term sustainability;
3. An integrated resource allocation strategy within clustered microgrids, including both active and reactive power resources, to improve voltage regulation and reduce system losses;
4. The provision of a flexible operational structure that enables cooperative, grid-connected, and fully islanded modes of operation among microgrids;

The remainder of this chapter is organized as follows. Section 5.2 presents the proposed tri-stage framework and details the associated mathematical formulation. Section 5.3 describes the studied system and provides the case studies along with the corresponding results and discussions. Finally, Section 5.3 concludes the chapter.

## 5.2 The Proposed Tri-Stage Optimization Framework

This section presents the mathematical formulation of the proposed tri-stage optimization framework, which includes PDS microgrid clustering, optimal DER resource planning for the clustered microgrids, and the optimal allocation of DERs and reactive power components across the PDS in successive stages. Fig. 5.1 illustrates the overall tri-stage process of the proposed framework, comprising: 1) microgrid clustering formulation, 2) optimal DER planning under different operational scenarios, and 3) coordinated allocation of DERs within the PDS along with reactive power resources to enhance voltage regulation and minimize network losses.

### 5.2.1 Stage I: PDS Clustering Algorithm

The relationships among buses in a PDS are governed not only by their physical topology but also by their underlying electrical characteristics, which are inherently reflected in the electrical distance between buses. Although the concept of electrical distance has been employed in various power system applications, its utilization for network structural analysis and clustering remains relatively limited. In Stage I of the proposed framework, the electrical distance between any two buses $i$ and $j$, defined based on the impedance of the distribution line connecting them, is used as the primary metric for assigning buses to the same cluster. Accordingly, the pairwise electrical distance between Bus $i$ and Bus $j$ is computed using (5.1).

$$d_{ij} = \left|Z_{ij}\right| = \sqrt{R_{ij}^2 + X_{ij}^2}, \ \forall i, j \in N \tag{5.1}$$

Here, $R_{ij}$ and $X_{ij}$ denote the per-unit resistance and reactance of the line connecting Buses $i$ and $j$, respectively, while the square matrix $\mathbf{D} \in \mathbb{R}^{N \times N}$ represents the electrical proximity among the PDS $N$ buses. For non-adjacent buses, a sufficiently large constant value is assigned to capture weak or indirect electrical coupling. The diagonal elements of $\mathbf{D}$ are set to zero, indicating zero electrical distance of each bus from itself.

Initially, each bus is treated as an individual cluster, resulting in a total of $N$ clusters. The *average linkage* electrical distance between two clusters, denoted as groups $A$ and $B$, is then defined according to (5.2).

$$d(A, B) = \frac{1}{|A|\,|B|} \sum_{i \in A} \sum_{j \in B} d_{ij} \tag{5.2}$$

Clusters are then iteratively merged using the *average linkage* criterion, where, at each iteration, the pair of clusters with the minimum distance $d(A, B)$ is combined, thereby progressively reducing the total number of clusters. This hierarchical merging process continues until a predefined number of clusters $\mathcal{M}$ is obtained [57]. The selection of the optimal number of clusters $\mathcal{M}$ is guided by domain-specific requirements and analysis of the clustering dendrogram,

**Algorithm 1** Hierarchical Agglomerative Clustering for PDS Partitioning

**Input:** Distribution network topology, line parameters $(R_{ij}, X_{ij})$, and target number of clusters $\mathcal{M}$.

**Output:** Partitioning of $N$ buses into $\mathcal{M}$ sustainable microgrid clusters.

**Initialize Distance Matrix:**
**for** each pair of buses $(i, j)$ **do**
  **if** bus $i$ and $j$ are directly connected **then**
    Compute $d_{ij} = \sqrt{R_{ij}^2 + X_{ij}^2}$
  **else if** $i = j$ **then**
    Set $d_{ij} = 0$
  **else**
    Set $d_{ij} = \infty$
  **end if**
**end for**
**Initial Clustering:** Assign each bus $i$ to its own cluster $C_i = \{i : \forall i \in N\}$.
**Iterative Merging:**
**while** number of clusters $> \mathcal{M}$ **do**
  Calculate inter-cluster distances for all pairs $(A, B)$ using average linkage:
  $d(A, B) = \frac{1}{|A||B|} \sum_{i \in A} \sum_{j \in B} d_{ij}$
  Find the pair of clusters $(A^*, B^*)$ that minimizes $d(A, B)$
  Merge $A^*$ and $B^*$ into a single cluster: $C_{new} = A^* \cup B^*$
  Update the set of clusters by replacing $A^*$ and $B^*$ with $C_{new}$
**end while**
**return** Final set of $\mathcal{M}$ microgrid clusters.

ensuring that each resulting microgrid exhibits strong internal electrical coherence and feasible operational boundaries. Algorithm 1 highlights the clustering steps of the PDSs.

### 5.2.2 Stage II: Optimal Planning of Microgrids DERs

The first Stage I provides the set of microgrids $\mathcal{M}$ and the corresponding set of buses assigned to each microgrid $m$ (i.e., $\mathcal{B}_m \subseteq \mathcal{B},\ \forall m \in \mathcal{M}$). Subsequently, Stage II is employed to determine the optimal sizing of DER components, including distributed generation and ESs, for each clustered microgrid. In this chapter, PV and wind turbines are used as distributed generation and the BES is used as ES to improve the microgrids flexibility.

The objective function is formulated to minimize the DER investment and operational costs for each microgrid $m$ across three distinct operational modes: a fully islanded mode with no collaboration, a local cooperation mode among microgrids without external utility support, and a full coordination mode between the microgrids and the main grid. Depending on the operating mode, the microgrids can rely on the installed DERs, power imported from the main grid, or power exchanged with adjacent microgrids within the PDS.

The planning decision variables include the optimal capacities $S_m^{\{.\}}$ and corresponding PCS ratings $PC_m^{\{.\}}$ for the DER units (PV, wind, and BES). The operational decision variables represent the system states across various scenarios and time steps; these include the power imported from the main grid $P_{m,t,s}^{grid}$, the power exchanged between microgrid $m$ and adjacent microgrids $P_{m,t,s}^{\mu g}$, and the power utilized $P_{m,t,s}^{\{.\},U}$ or curtailed $P_{m,t,s}^{\{.\},Cr}$ from PV and wind generation. Furthermore, these variables encompass the charging $P_{m,t,s}^{\mathrm{Ch}}$ and discharging $P_{m,t,s}^{\mathrm{Dch}}$ power of the BES, in addition to its SoC $\mathrm{SoC}_{m,t,s}$.

#### 5.2.2.1 Objective Function

The objective function is formulated to balance asset investment and energy cost. It optimizes CapEx associated with PV, wind, and BES sizing, and corresponding PCS ratings. From an operational perspective, the objective function minimizes OpEx, including the cost of energy procurement and energy trading among microgrids as well as with the main grid. The objective function is given in (5.3).

$$\min : \sum_{m \in \mathcal{M}} CAPEX_m + \sum_{m \in \mathcal{M}} \sum_{s \in \mathcal{S}} \mathbb{P}(s) \cdot OPEX_{m,s} \tag{5.3}$$

Here, $CAPEX_m$ denotes the investment cost of DERs for microgrid $m$, while the term $\sum_{s \in \mathcal{S}} \mathbb{P}(s) \cdot OPEX_{m,s}$ represents the expected OpEx, where uncertainties in DER generation and microgrid demand are captured through a set of discrete operational scenarios $s$, each characterized by a probability of occurrence $\mathbb{P}(s)$.

The $CAPEX$ represents the upfront investment costs for PV, wind, BES, and PCS units, which are normalized into hourly equivalents and summed over the optimization horizon specified in equation (5.4).

$$CAPEX_m = \frac{\sum_{t\in\mathcal{T}} \Delta t}{8760}\Bigg[\frac{C^{\mathrm{PV}}\, S_m^{\mathrm{PV}} + C_{Uni}^{PC}\, PC_m^{\mathrm{PV}}}{\tau^{\mathrm{PV}}} + \frac{C^{\mathrm{W}}\, S_m^{\mathrm{W}} + C_{Uni}^{PC}\, PC_m^{\mathrm{W}}}{\tau^{\mathrm{W}}} + \\ \frac{C^{\mathrm{BSS}}\, S_m^{\mathrm{BSS}} + C_{Bi}^{PC}\, PC_m^{\mathrm{BSS}}}{\tau^{\mathrm{BSS}}}\Bigg] \tag{5.4}$$

The planning decision variables for microgrid $m$ include the capacity $S_m^{\{.\}}$ and the associated PCS rating $PC_m^{\{.\}}$ (in kW or kWh) for the PV, wind, and BES units. In this formulation, $C^{\{.\}}$ and $\tau^{\{.\}}$ represent the unit investment cost (in \$/kW or \$/kWh) and the expected lifetime of each component in years.

The $OPEX$ accounts for the cost of energy imported from the main grid and the bidirectional energy exchange between microgrid $m$ and adjacent microgrids, as formulated in (5.5)

$$OPEX_{m,s} = \sum_{t\in\mathcal{T}}\left(E^{grid}\cdot P_{m,t,s}^{grid} + E^{\mu g}\cdot\ P_{m,t,s}^{\mu g}\right)\Delta t \tag{5.5}$$

The operational decision variables for microgrid $m$ include the power imported from the main grid $P_{m,t,s}^{grid}$ and the power exchanged with adjacent microgrids $P_{m,t,s}^{\mu g}$ (in kW). A positive value for $P_{m,t,s}^{\mu g}$ indicates power received by microgrid $m$ and a negative value indicates power supplied to neighboring microgrids. In this formulation, $E^{grid}$ and $E^{\mu g}$ represent the unit energy costs (in \$/kWh) for main grid purchases and inter-microgrid exchanges, respectively.

#### 5.2.2.2 Constraints

To ensure demand satisfaction for each microgrid, the objective function is constrained by the power balance condition at the microgrid level, as formulated in (5.6).

$$P_{m,t,s}^{grid} + P_{m,t,s}^{\mu g} + P_{m,t,s}^{PV,U} + P_{m,t,s}^{W,U} + P_{m,t,s}^{Dch} - P_{m,t,s}^{Ch} = \sum_{b\in\mathcal{B}_m} P_b^L, \forall t\in\mathcal{T}\wedge m\in\mathcal{M}\wedge s\in\mathcal{S} \tag{5.6}$$

where the operational variables $P_{m,t,s}^{\{.\},U}$ and $P_{m,t,s}^{\{.\},Cr}$ denote the distributed generation utilized and curtailed power (kW), respectively, while $P_{m,t,s}^{ch}$ and $P_{m,t,s}^{Dch}$ represent the BES charging and discharging power (kW). The term $\sum_{b\in\mathcal{B}_m} P_b^L$ corresponds to the aggregated load demand of microgrid $m$ across all buses assigned to it.

The power exchanged between microgrids must also satisfy a balance condition, ensuring that any power imported or exported by a microgrid is compensated by corresponding exports or imports from other microgrids, as defined in (5.7).

$$\sum_{m\in\mathcal{M}} P^{\mu g}_{m,t,s} = 0, \forall t \in \mathcal{T} \wedge m \in \mathcal{M} \wedge s \in \mathcal{S} \tag{5.7}$$

The utilized and curtailed PV and wind power are limited to the maximum generation available from the installed capacities by constraints (5.8) and (5.9), respectively:

$$P^{PV,U}_{m,t,s} + P^{PV,Cr}_{m,t,s} = S^{PV}_{m} \cdot P^{PV|1MW}_{t,s}, \forall t \in \mathcal{T} \wedge m \in \mathcal{M} \wedge s \in \mathcal{S} \tag{5.8}$$

$$P^{W,U}_{m,t,s} + P^{W,Cr}_{m,t,s} = S^{W}_{m} \cdot P^{W|1MW}_{t,s}, \forall t \in \mathcal{T} \wedge m \in \mathcal{M} \wedge s \in \mathcal{S} \tag{5.9}$$

Where $P^{\{\cdot\}|1\text{MW}}_{t,s}$ denotes the maximum power output per 1 MW of distributed generation under time $t$ and scenario $s$.

The BES SoC is constrained by the energy balance, such that any change in $SoC_{m,t,s}$ corresponds precisely to the energy charged into or discharged from the BES at each time step. The BES energy balance is formally expressed in (5.10).

$$\mathrm{SoC}_{m,t+1,s} = \mathrm{SoC}_{m,t,s} + \left(\eta^{\mathrm{PCS}}\, P^{\mathrm{Ch}}_{m,t,s} - P^{\mathrm{Dch}}_{m,t,s}/\eta^{\mathrm{PCS}}\right) \Delta t,\ \forall t \in \mathcal{T} \wedge m \in \mathcal{M} \wedge s \in \mathcal{S} \tag{5.10}$$

$$\underline{\alpha}\, S^{\mathrm{BSS}}_{m} \leq \mathrm{SoC}_{m,t,s} \leq \overline{\alpha}\, S^{\mathrm{BSS}}_{m},\ \forall t \in \mathcal{T} \wedge m \in \mathcal{M} \wedge s \in \mathcal{S} \tag{5.11}$$

Here, $\eta^{\mathrm{PCS}}$ denotes the efficiency of the PCS, while $\underline{\alpha}$ and $\overline{\alpha}$ represent the lower and upper bounds of the SoC, respectively, to prevent excessive BES degradation. Additionally, the BES charging and discharging powers are constrained to prevent simultaneous charging and discharging, as specified in (5.12).

$$P^{\mathrm{Ch}}_{m,t,s} \times P^{\mathrm{Dch}}_{m,t,s} = 0,\ \forall t \in \mathcal{T} \wedge m \in \mathcal{M} \wedge s \in \mathcal{S} \tag{5.12}$$

To ensure that the coordinated power dispatch from DERs remains within the limits of their respective PCS converter ratings, the operational power decision variables are constrained by the corresponding PCS capacities as follows:

$$0 \leq P^{PV,U}_{m,t,s} \leq PC^{PV}_{m},\ \forall t \in \mathcal{T} \wedge m \in \mathcal{M} \wedge s \in \mathcal{S} \tag{5.13}$$

$$0 \leq P^{W,U}_{m,t,s} \leq PC^{W}_{m},\ \forall t \in \mathcal{T} \wedge m \in \mathcal{M} \wedge s \in \mathcal{S} \tag{5.14}$$

$$0 \leq P^{Ch}_{m,t,s}, P^{Dch}_{m,t,s} \leq PC^{BSS}_{m},\ \forall t \in \mathcal{T} \wedge m \in \mathcal{M} \wedge s \in \mathcal{S} \tag{5.15}$$

The planning decision variables are subject to upper bounds to ensure feasible component sizing as follows:

$$0 \leq S^{\{\cdot\}}_{m} \leq \overline{S}^{\{\cdot\}}_{m},\ \forall m \in \mathcal{M} \tag{5.16}$$

$$0 \leq PC^{\{\cdot\}}_{m} \leq \overline{PC}^{\{\cdot\}}_{m},\ \forall m \in \mathcal{M} \tag{5.17}$$

Where $\overline{S}_m^{\{.\}}$ and $\overline{PC}_m^{\{.\}}$ denote the maximum allowable capacity and PCS rating for each respective component (PV, wind, and BES) within microgrid $m$.

Finally, two additional constraints are introduced to enable flexible adjustment of the optimization framework under different operational scenarios, including grid-connected, cooperative, and fully islanded microgrid operation. To enforce islanded operation from the main grid, constraint (5.18) is incorporated to prohibit energy import from the main grid. Under this condition, microgrids are allowed to operate cooperatively through energy exchange among themselves. For fully isolated operation, constraint (5.19) is further included to prevent any import or export of energy between microgrids, thereby ensuring completely independent operation.

$$P_{m,t,s}^{grid} = 0,\ \forall t \in \mathcal{T} \wedge m \in \mathcal{M} \wedge s \in \mathcal{S}, \quad \text{(Prevents main grid contribution.)} \tag{5.18}$$

$$P_{m,t,s}^{\mu g} = 0,\ \forall t \in \mathcal{T} \wedge m \in \mathcal{M} \wedge s \in \mathcal{S}, \quad \text{(Prevents microgrids energy exchange.)} \tag{5.19}$$

### 5.2.3 Stage III: DERs and Reactive Power Resources Allocations

Stage II determines the optimal sizing of the DERs within each microgrid under different operation scenarios to address the uncertainties in both generation and demand, focusing mainly on active power. Subsequently, Stage III determines the optimal placement and allocation of the DERs within each microgrid, as well as the required reactive power resources (i.e., shunt capacitors) to meet the reactive power demand. During this stage, the optimization is designed for two main objectives: 1) reactive power demand fulfillment, and 2) improving the microgrids' operation, represented by voltage regulation and PDS power losses. Under this configuration, the planning decision variables of Stage III are the allocated capacity of wind ($S_b^W, PC_b^W$), PV ($PC_b^{PV}, S_b^{PV}$), BES ($S_b^{\text{BSS}}, PC_b^{\text{BSS}}$), and the reactive power resources ($S_b^Q$) for each bus within each microgrid. On the other hand, the management decision variables include the PDS state variables ($|V_{b,t}|\angle\delta_{b,t}$) and active and reactive power coordination from the DERs and reactive power resources ($P_{b,t}^{W,U}, P_{b,t}^{PV,U}, P_{b,t}^{Ch}, P_{b,t}^{Dch}, Q_{b,t}^{Var}$).

#### 5.2.3.1 Objective Function

In this stage, the objective is designed to reduce the CapEx of the reactive power resources, i.e., one-time investment cost, and to enhance the PDS operation represented by improving the voltage regulation and minimizing overall PDS power losses. The multi-objective function of

Stage III is defined by (5.20).

$$\min : w_1 P_{loss} + w_2 \Delta V + w_3 CAPEX^{Var} \tag{5.20}$$

$$P_{loss} = \sum_{t \in \mathcal{T}} \left( \sum_{b \in \mathcal{B}} \sum_{b' \in \mathcal{B}} |V_{b,t}||V_{b',t}||Y_{bb'}| Cos\big(\delta_{b,t} - \delta_{b',t} - \theta_{bb'}\big) \right) \tag{5.21}$$

$$\Delta V = \sum_{t \in \mathcal{T}} \left( \sum_{b \in \mathcal{B}} |1^{p.u} - |V_{b,t}|| \right) \tag{5.22}$$

$$CAPEX^{Var} = \frac{\sum_{t \in \mathcal{T}} \Delta t}{8760} \left( \frac{C^{\mathrm{Var}} \sum_{b \in \mathcal{B}} S_b^Q}{\tau^{\mathrm{Q}}} \right) \tag{5.23}$$

Here, $w_{1,2,3}$ are weighting coefficients that regulate the trade-off among the multiple objective components. Equation (5.21) quantifies the network power losses as a function of the bus voltage magnitudes $|V_{b,t}|$, voltage angles $\delta_{b,t}$, and the elements of the admittance matrix $|Y_{bb'}|\angle\theta_{bb'}$ between interconnected buses. Equation (5.22) represents the voltage deviation of all buses from the nominal value of 1 p.u. Finally, (5.23) models the CapEx associated with reactive power components, where $S_b^Q$ denotes the reactive power resource allocated at bus $b$. This term stands for the CapEx alone, where reactive power OpEx is accounted for within the energy cost provided by the PDS operator; i.e., the energy cost of the main grid accounts for the reactive power needed by the consumers.

The weighting coefficients are calculated to normalize the three objectives into the same operational range. This is achieved by calculating the ratio between the lower bounds of each objective, as defined in (5.24).

$$w_1 = \frac{\underline{CAPEX^{Var}}}{\underline{P_{loss}}}, w_2 = \frac{\underline{CAPEX^{Var}}}{\underline{\Delta V}}, w_3 = 1 \tag{5.24}$$

Here, $\underline{CAPEX^{Var}}$ represents the lower bound of the reactive resources CapEx when all other objectives are ignored (i.e., $w_1 = w_2 = 0$). Similarly, $\underline{P_{loss}}$ represents the lower bound of the PDS power loss when the other objectives are ignored, and $\underline{\Delta V}$ represents the lower bound of the PDS voltage regulation.

#### 5.2.3.2 Constraints

To ensure power flow balance, these objectives are subject to the power flow constraints defined in (5.25)–(5.27).

$$\underline{V_b} \leq V_{b,t} \leq \overline{V_b},\ \forall t \in \mathcal{T} \wedge \forall b \in \mathcal{B} \tag{5.25}$$

$$P_{b,t}^{PV,U} + P_{b,t}^{W,U} + P_{b,t}^{Dch} - P_{b,t}^{Ch} - P_{b,t}^{D} = |V_{b,t}| \sum_{b' \in \mathcal{B}} |V_{b',t}||Y_{bb'}|Cos\big(\delta_{b,t} - \delta_{b',t} - \theta_{bb'}\big),\ \forall t \in \mathcal{T} \wedge \forall b \in \mathcal{B} \tag{5.26}$$

$$Q_{b,t}^{Var} - Q_{b,t}^{D} = |V_{b,t}| \sum_{b' \in \mathcal{B}} |V_{b',t}| \cdot |Y_{bb'}|Sin\big(\delta_{b,t} - \delta_{b',t} - \theta_{bb'}\big),\ \forall t \in \mathcal{T} \wedge \forall b \in \mathcal{B} \tag{5.27}$$

Where $\underline{V_b}$ and $\overline{V_b}$ denote the lower and upper voltage magnitude limits at bus $b$, respectively. The term $P_{b,t}^{\{.\},U}$ represents the utilized distributed generation power at bus $b$, while $P_{b,t}^{Ch}$ and $P_{b,t}^{Dch}$ denote the BES charging and discharging power at the same bus. Furthermore, $P_{b,t}^{D}$ and $Q_{b,t}^{D}$ correspond to the active and reactive power demand, respectively, and $Q_{b,t}^{Var}$ represents the reactive power injected by the VAR resources at bus $b$.

In this stage, each bus is assumed to be capable of hosting on-site DERs, including wind, PV, and BES units. However, the injected power from these on-site resources is constrained by their corresponding installed capacities, as defined in (5.30)–(5.33).

$$P_{b,t}^{PV,U} + P_{b,t}^{PV,Cr} = S_b^{PV} \cdot P_t^{PV_{|1MW}},\ \forall t \in \mathcal{T} \wedge \forall b \in \mathcal{B} \tag{5.28}$$

$$P_{b,t}^{W,U} + P_{b,t}^{W,Cr} = S_b^{W} \cdot P_t^{W_{|1MW}},\ \forall t \in \mathcal{T} \wedge \forall b \in \mathcal{B} \tag{5.29}$$

$$0 \leq P_{b,t}^{PV,U} \leq PC_b^{PV},\ \forall t \in \mathcal{T} \wedge \forall b \in \mathcal{B} \tag{5.30}$$

$$0 \leq P_{b,t}^{W,U} \leq PC_b^{W},\ \forall t \in \mathcal{T} \wedge \forall b \in \mathcal{B} \tag{5.31}$$

$$0 \leq P_{b,t}^{Ch}, P_{b,t}^{Dch} \leq PC_b^{BSS},\ \forall t \in \mathcal{T} \wedge \forall b \in \mathcal{B} \tag{5.32}$$

$$-S_b^{Q} \leq Q_{b,t}^{Var} \leq S_b^{Q},\ \forall t \in \mathcal{T} \wedge \forall b \in \mathcal{B} \tag{5.33}$$

Here, $S_b^{PV}$ and $S_b^{W}$ denote the allocated PV and wind capacities at bus $b$, respectively, while $PC_b^{BSS}$ represents the allocated BES PCS rating at that bus. The energy storage system at bus $b$ is further constrained by the energy balance equation (5.34), the upper and lower SoC bounds defined in (5.35), and the constraint preventing simultaneous charging and discharging as specified in (5.36).

$$\mathrm{SoC}_{b,t+1} = \mathrm{SoC}_{b,t} + \big(\eta^{\mathrm{PCS}}\, P_{b,t}^{\mathrm{Ch}} - P_{b,t}^{\mathrm{Dch}}/\eta^{\mathrm{PCS}}\big)\, \Delta t,\ \forall t \in \mathcal{T} \wedge b \in \mathcal{B} \tag{5.34}$$

$$\underline{\alpha}\, S_b^{\mathrm{BSS}} \leq \mathrm{SoC}_{b,t} \leq \overline{\alpha}\, S_b^{\mathrm{BSS}},\ \forall t \in \mathcal{T} \wedge b \in \mathcal{B} \tag{5.35}$$

$$P_{b,t}^{Ch} \times P_{b,t}^{Dch} = 0,\ \forall t \in \mathcal{T} \wedge b \in \mathcal{B} \tag{5.36}$$

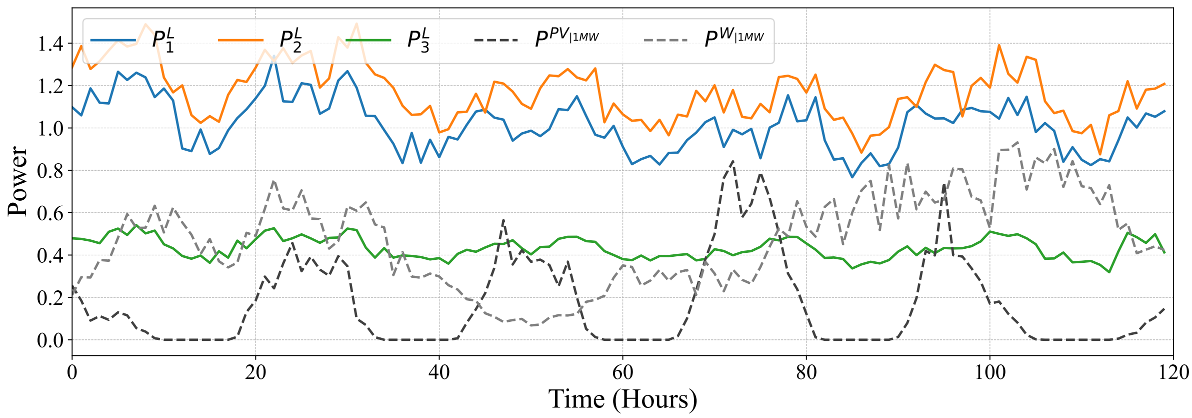


Figure 5.2: Microgrid loads and maximum power output per 1 MW of distributed generation over five representative days.

Finally, to ensure consistency between the optimal design determined in Stage II and the allocation process in Stage III, the capacities assigned within each microgrid are constrained to comply with the previously estimated optimal values under different operational scenarios. This is achieved by bounding the allocated capacities in this stage within predefined upper and lower limits, as specified in (5.37)–(5.42).

$$S_m^{PV} \leq \sum_{b \in \mathcal{B}_m} S_b^{PV} \leq (1 + \Delta S) S_m^{PV}, \ \forall m \in \mathcal{M} \tag{5.37}$$

$$S_m^{W} \leq \sum_{b \in \mathcal{B}_m} S_b^{W} \leq (1 + \Delta S) S_m^{W}, \ \forall m \in \mathcal{M} \tag{5.38}$$

$$S_m^{BSS} \leq \sum_{b \in \mathcal{B}_m} S_b^{BSS} \leq (1 + \Delta S) S_m^{BSS}, \ \forall m \in \mathcal{M} \tag{5.39}$$

$$PC_m^{PV} \leq \sum_{b \in \mathcal{B}_m} PC_b^{PV} \leq (1 + \Delta S) PC_m^{PV}, \ \forall m \in \mathcal{M} \tag{5.40}$$

$$PC_m^{W} \leq \sum_{b \in \mathcal{B}_m} PC_b^{W} \leq (1 + \Delta S) PC_m^{W}, \ \forall m \in \mathcal{M} \tag{5.41}$$

$$PC_m^{BSS} \leq \sum_{b \in \mathcal{B}_m} PC_b^{BSS} \leq (1 + \Delta S) PC_m^{BSS}, \ \forall m \in \mathcal{M} \tag{5.42}$$

The term $(1+\Delta S)$ is introduced to permit an increase in the total design capacity by a percentage $\Delta S$ in order to compensate for the PDS line losses. The value of $\Delta S$ is estimated to represent the worst-case power loss in the system, which is calculated by assuming no DERs are installed and PDSs rely on the main power grid alone. It is worth noting that while Stage II is solved for multiple scenarios $\mathcal{S}$ to account for DERs and demand uncertainty, Stage III is solved under the worst-case operational scenario due to the strong nonlinearity of the power flow equations.

Table 5.1: Simulation Parameters used in the optimization.

| | | |
|---|---|---|
| | **PV** | |
| $C^{\text{PV}} = 2,500,000\,\$/\text{MW}$ | $\overline{S}^{\text{PV}} = 1000\,\text{MW}$ | $\tau^{\text{PV}} = 20\,(\text{years})$ |
| $C^{\text{PCS,PV}} = 470,000\,\$/\text{MW}$ | $\overline{PC}^{\text{PV}} = 1000\,\text{MW}$ | $\tau^{\text{PCS,PV}} = 20\,(\text{years})$ |
| | **Wind** | |
| $C^{\text{W}} = 1,800,000\,\$/\text{MW}$ | $\overline{S}^{\text{W}} = 1000\,\text{MW}$ | $\tau^{\text{W}} = 20\,(\text{years})$ |
| $C^{\text{PCS,W}} = 470,000\,\$/\text{MW}$ | $\overline{PC}^{\text{W}} = 1000\,\text{MW}$ | $\tau^{\text{PCS,W}} = 20\,(\text{years})$ |
| | **BES** | |
| $\eta_{\text{ch}} = 0.92$ | $\eta_{\text{dch}} = 0.92$ | $\underline{\alpha} = 0.20$ |
| $\overline{\alpha} = 0.90$ | $\overline{S}^{\text{BES}} = 8000\,\text{MWh}$ | $\tau^{\text{BES}} = 20\,(\text{years})$ |
| $C^{\text{BES}} = 200,000\,\$/\text{MWh}$ | $\eta^{\text{PCS}} = 0.90$ | $\overline{PC}^{\text{BES}} = 1000\,\text{MW}$ |
| $C^{\text{PCS,BES}} = 470,000\,\$/\text{MW}$ | $\tau^{\text{PCS,BES}} = 20\,(\text{years})$ | |
| | **Objective Parameters** | |
| $E^{\text{grid}} = 180\,\$/\text{MWh}$ | $\overline{P}^{\text{grid}} = 100\,\text{MW}$ | $\Delta t = 1\,(\text{hour})$ |
| $\mathcal{S} = 1\,(\text{scenario})$ | $\mathcal{M} = 3\,(\text{microgrids})$ | $\Delta S = 5\%$ |
| $E^{\mu g} = 120\,\$/\text{MWh}$ | | |

In order to account for the geographical limitations of installing wind turbines, constraint (5.43) is used to ensure that wind turbines are installed at the suitable buses.

$$S^W b = 0,\ \forall b \in \mathcal{B}m \setminus \mathcal{B}_m^W \wedge \forall m \in \mathcal{M} \tag{5.43}$$

Here, $\mathcal{B}_m^W$ represents the set of buses within microgrid $m$ where wind turbines can be installed, while the term $\mathcal{B}_m \setminus \mathcal{B}_m^W$ denotes the remaining buses within microgrid $m$

## 5.3 Simulation Results

This section evaluates the performance of the proposed tri-stage optimization framework, validated on the IEEE 33-bus test system. The analysis begins by demonstrating the clustering algorithm's flexibility and interpretability, utilizing distribution line impedances to decentralize the system into electrically coherent microgrids. Following this decentralization, the framework

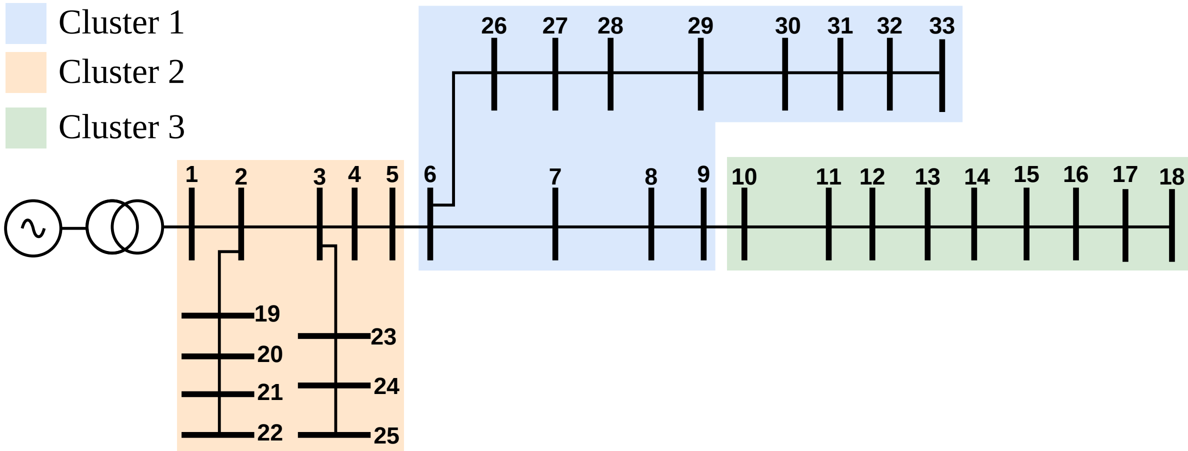


Figure 5.3: Single line diagram of IEEE 33-bus system under study and network partitioning.

addresses the coordinated planning of multi-microgrid systems. Utilizing historical load and renewable generation data from the Ontario electricity market [94], the model determines the optimal sizing of PV, wind, and BES units by evaluating the aggregated bus loads within each microgrid cluster alongside the maximum power output per 1 MW of distributed generation. As illustrated in Fig. 5.2, these profiles represent the microgrid loads and the maximum power output per 1 MW of distributed generation over five representative days. This sizing process is conducted across three distinct operational scenarios: Case 1, a fully islanded mode with no collaboration; Case 2, a local cooperation mode among microgrids without external utility support; and Case 3, which incorporates full coordination between the microgrids and the main grid. Table 5.1 summarizes the simulation parameters for the optimization.

In the final stage an optimal resource allocation strategy is implemented to finalize the system design. In this stage, the resources determined in the previous sizing phase are optimally placed within the distribution network. This step is designed to achieve optimal power flow, minimize system losses, and maintain voltage stability under worst-case operating conditions. The simulation framework was developed in Python and utilized the Gurobi optimizer to solve the models for Stages II and III on an Apple workstation equipped with an M1 Pro processor and 16 GB of RAM. The solver was configured with an aggressive level two presolve and a MIPFocus of one to prioritize the rapid discovery of high-quality feasible solutions. To address the non-convex formulation, a level one cutting plane strategy was employed with a relative optimality gap (MIPGap) of 3.5 percent. This configuration guarantees that the final incumbent solution is within a 3.5 percent relative difference from the best possible objective bound. Additionally,

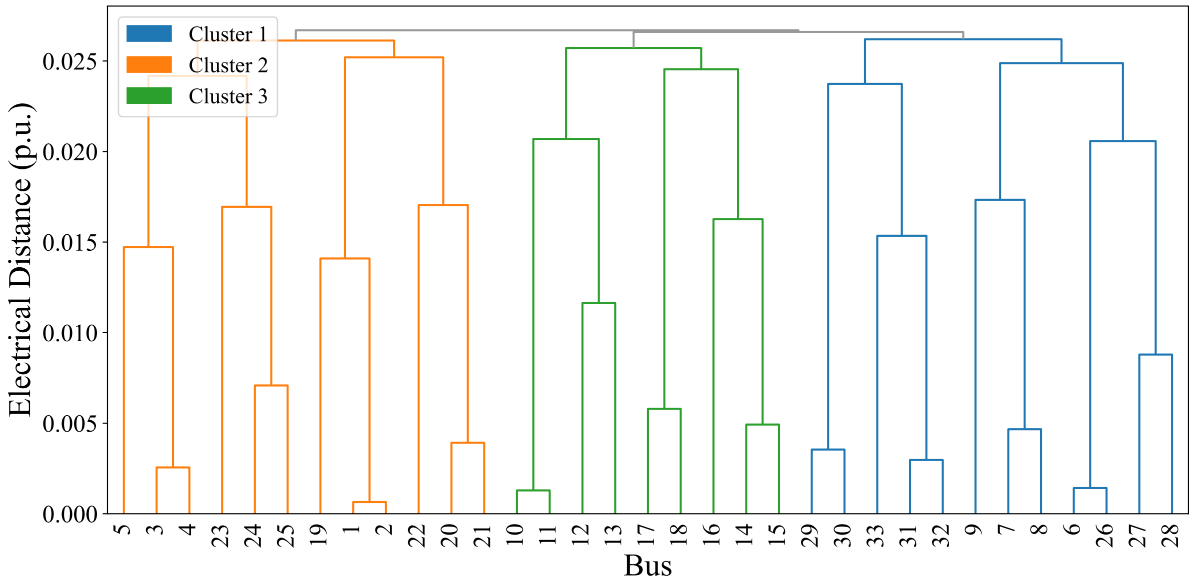


Figure 5.4: Hierarchical agglomerative clustering dendrogram for the IEEE 33-bus system.

a primal feasibility tolerance of 0.01 was implemented to ensure the solver yields high-precision results within a practical timeframe.

### 5.3.1 Microgrid Clustering

The clustering Stage I begins by specifying the target number of microgrid clusters, which is set to $\mathcal{M} = 3$ for the IEEE 33-bus test system. This selection demonstrates the flexibility of the proposed method in determining $\mathcal{M}$ based on system characteristics. Fig. 5.4 presents the clustering dendrogram, illustrating how different buses are progressively merged into the same cluster according to their electrical distance. The grouping of buses and the resulting clustered microgrids for the IEEE 33-bus system are shown in Fig. 5.3, indicating that electrically adjacent buses are assigned to the same microgrid. Furthermore, power flow analysis under full-load conditions confirms that the clustering algorithm effectively captures the network's electrical structure through line impedance characteristics. As depicted in Fig. 5.5, transitions between clusters correspond to noticeable variations in voltage magnitude while maintaining compliance with operational limits.

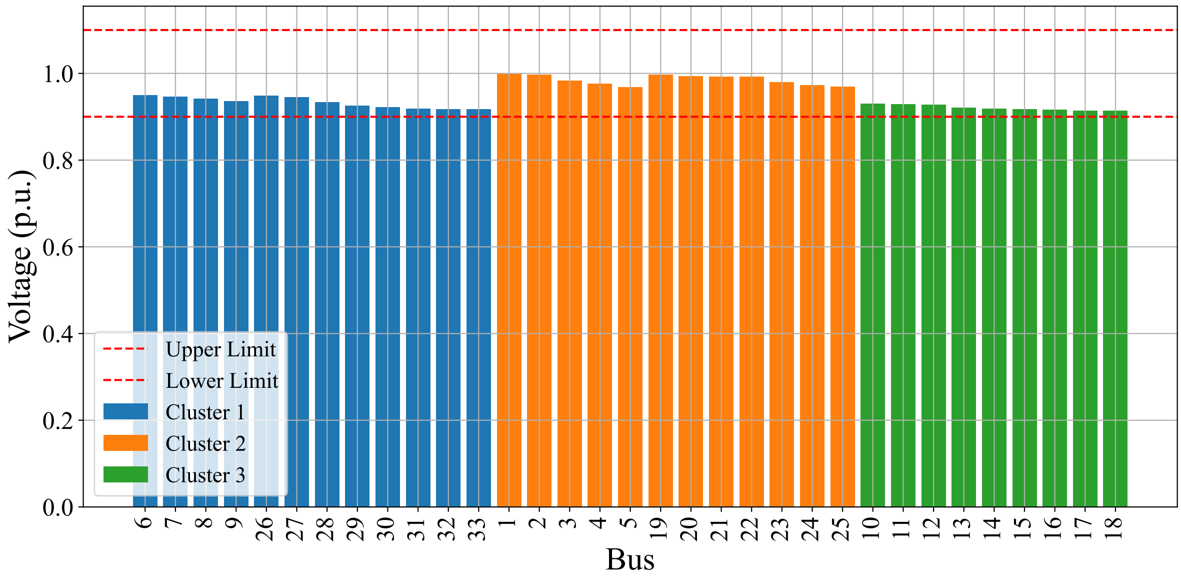


Figure 5.5: Voltage magnitude profile of the IEEE 33-bus system.

### 5.3.2 Optimal Planning of Clustered Microgrid DERs

In Stage II, following the clustering process, representative load profiles are constructed by aggregating the buses within each microgrid and averaging the renewable generation profiles at the bus level. These aggregated profiles are then incorporated into the optimization model over a one-year planning horizon with hourly resolution $\Delta t = 1hr$.

To capture stochastic behavior, scenario-based variations are generated for the demand $P_b^L$, solar generation profiles $P_{t,s}^{PV|_{1MW}}$, and wind generation profiles $P_{t,s}^{W|_{1MW}}$. These variations are created independently for each microgrid $m \in \mathcal{M}$ and scenario $s \in \mathcal{S}$. Each parameter is obtained by perturbing its base profile at time $t \in \mathcal{T}$ using a Gaussian distribution centered around the nominal value. The probability density function of this distribution is defined as:

$$f(x) = \frac{1}{\sigma\sqrt{2\pi}} e^{-\frac{1}{2}\left(\frac{x-\mu}{\sigma}\right)^2} \tag{5.44}$$

where $x$ denotes the generated stochastic variable, $\mu$ represents the mean (base) value, and $\sigma$ denotes the standard deviation. For the demand profile, a standard deviation of $5\% \times P_b^L$ is applied, with sampled values clipped to the interval $[0.8P_b^L, 1.2P_b^L]$. Similarly, both $P_{t,s}^{PV|_{1MW}}$ and $P_{t,s}^{W|_{1MW}}$ are generated using a standard deviation equal to 10% of their respective base values, and are restricted to the range [0.7, 1.3] times the nominal profile. This independent sampling approach captures the localized spatial and temporal variability of both load demand

Table 5.2: Optimal sizing for each microgrid and the system aggregate across three operational cases.

| Microgrid | Case | Sizing | | | | | |
|---|---|---|---|---|---|---|---|
| | | $S^{\mathrm{PV}}$ (MW) | $PC^{\mathrm{PV}}$ (MW) | $S^{\mathrm{W}}$ (MW) | $PC^{\mathrm{W}}$ (MW) | $S^{\mathrm{BES}}$ (MWh) | $PC^{\mathrm{BES}}$ (MW) |
| **1** | 1 | 1.3 | 0.65 | 8.9 | 1.74 | 93.58 | 1.32 |
| | 2 | 1.67 | 0.81 | 7.89 | 1.74 | 103.66 | 1.85 |
| | 3 | - | - | 3.05 | 1.03 | - | - |
| **2** | 1 | 0.6 | 0.35 | 15.1 | 2.19 | 72.89 | 1.37 |
| | 2 | 0.77 | 0.43 | 13.39 | 2.19 | 80.74 | 1.92 |
| | 3 | - | - | 3.05 | 1.03 | 0.29 | 0.05 |
| **3** | 1 | 0.44 | 0.22 | 4.18 | 0.81 | 36.75 | 0.52 |
| | 2 | 0.56 | 0.27 | 3.7 | 0.81 | 40.7 | 0.72 |
| | 3 | - | - | 3.05 | 1.03 | 7.57 | 0.68 |
| **Aggregate** | 1 | 2.34 | 1.22 | 28.18 | 4.74 | 203.22 | 3.21 |
| | 2 | 3 | 1.51 | 24.98 | 4.74 | 225.1 | 4.49 |
| | 3 | - | - | 9.15 | 3.09 | 7.86 | 0.73 |

and renewable generation across the system.

The optimal capacity sizing results for both the individual microgrids and the aggregated system are summarized in Table 5.2. As observed, the required asset capacities vary across the different operational cases. In Case 1, independent islanded operation necessitates the highest generation capacity, as each microgrid must independently hedge against stochastic variations to reliably satisfy its local demand. In Case 2, the introduction of collaboration strategy enables microgrids to share resources and exchange power. This cooperation reduces the required renewable generation capacity; however, it necessitates the highest storage capacity to facilitate energy exchange and enhance operational flexibility among the interconnected microgrids. he operational behavior of Case 2 over 10 representative days is illustrated in Fig. 5.6. The subplots present the individual microgrid power profiles, including load profiles, utilized PV and wind power, and BES charge/discharge cycles with their corresponding SoC trajectories, alongside the aggregated system power profiles. The figure highlights the synergistic performance among the microgrids, particularly during periods when renewable generation exceeds demand.

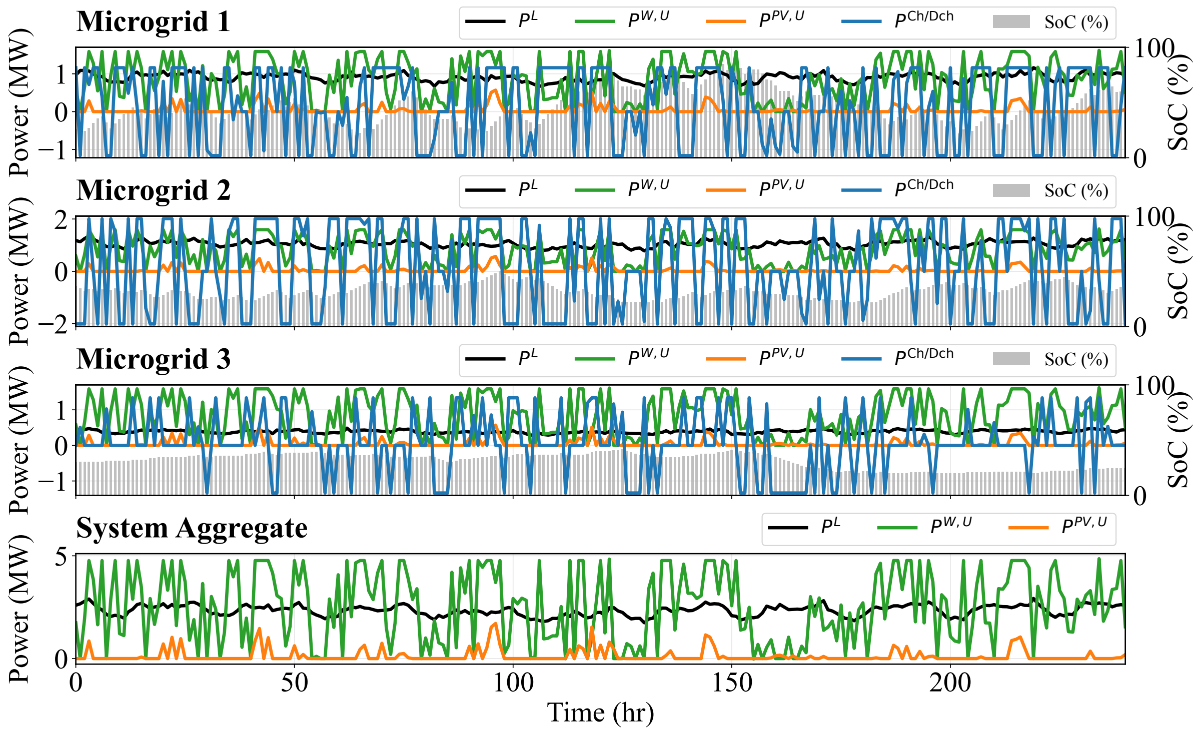


Figure 5.6: Operational results for Case 2 over 10 representative days. Individual microgrid power profiles and SoC alongside aggregated system power profiles.

In Case 3, both the generation and storage capacity requirements decrease significantly with the integration of the main utility grid. The availability of the main grid as an effectively unlimited energy buffer substantially reduces the need for large local renewable generation and storage capacities, resulting in the most capacity-efficient configuration among the considered scenarios.

The optimal capacity sizing results for both the individual microgrids and the aggregated system are summarized in Table 5.2. As observed, the required asset capacities vary across the different operational cases. In Case 1, independent islanded operation necessitates the highest generation capacity, as each microgrid must independently hedge against stochastic variations to reliably satisfy its local demand. In Case 2, the introduction of collaboration strategy enables microgrids to share resources and exchange power. This cooperation reduces the required renewable generation capacity; however, it necessitates the highest storage capacity to facilitate energy exchange and enhance operational flexibility among the interconnected microgrids. The operational behavior of Case 2 over 10 representative days is illustrated in Fig. 5.6. The subplots present the individual microgrid power profiles and corresponding SoC trajectories, along with the aggregated system power profiles. These results highlight the coordinated operation of the

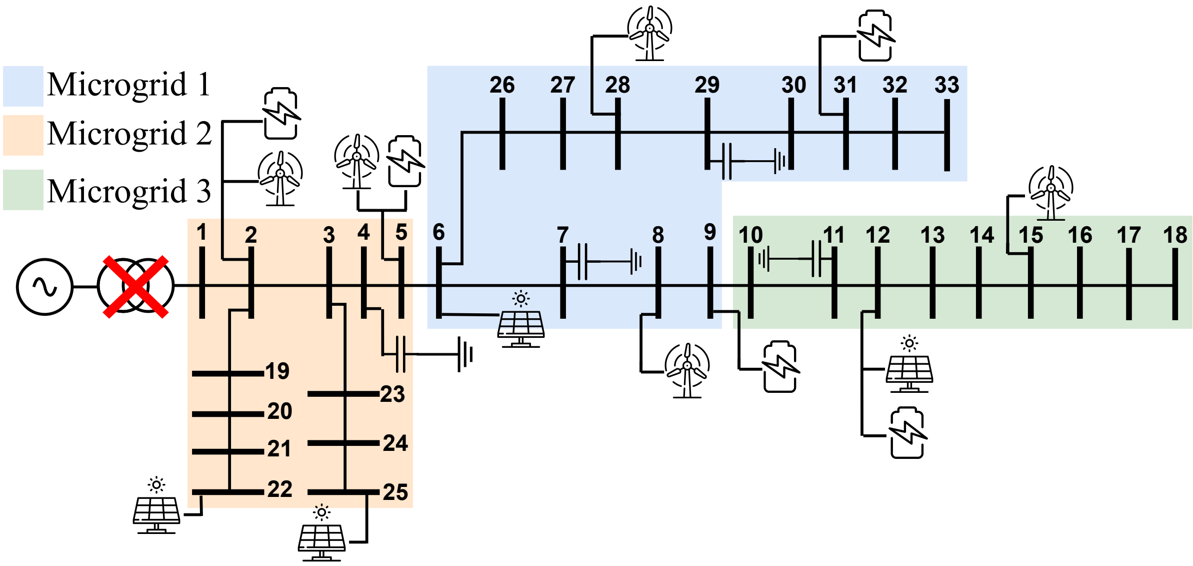


Figure 5.7: DERs and reactive power resources allocations within the clustered microgrids under collaborative operation of Case 2.

networked microgrids, where the BES charges during periods of excess renewable generation and discharges when generation is insufficient to meet demand. Notably, Microgrid 2 possesses the largest storage capacity and functions as the primary energy buffer within the system. Consequently, it undergoes fewer charge-discharge cycles compared to Microgrids 1 and 3, while providing substantial discharge support during intervals of zero wind or solar generation. In Case 3, both the generation and storage capacity requirements decrease significantly with the integration of the main utility grid. The availability of the main grid as an effectively unlimited energy buffer substantially reduces the need for large local renewable generation and storage capacities, resulting in the most capacity-efficient configuration among the considered scenarios.

Furthermore, the results highlight distinct technology preferences. Across all three operational cases, wind generation is consistently preferred over solar PV. This preference is driven by wind's lower relative cost and its potential for continuous generation throughout the day, which aligns better with self-sufficiency goals compared to solar power, which is strictly limited to certain daylight hours. Additionally, the required BES capacity is larger than the wind capacity across all cases, a necessity to adequately compensate for periods of increased demand or decreased renewable generation.

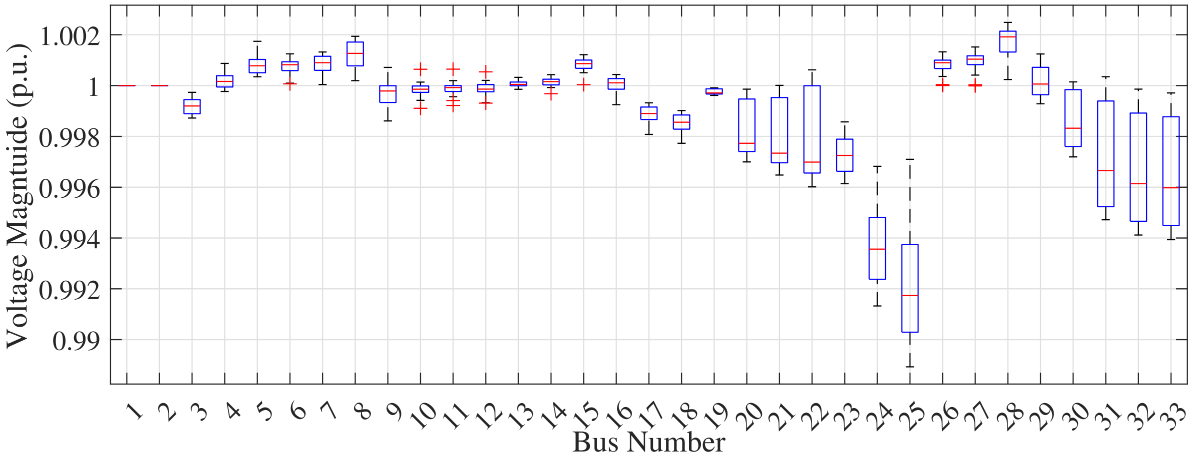


Figure 5.8: Voltage variation of the IEEE 33-bus test system after DER and reactive power resources allocation.

### 5.3.3 Optimal Resources Allocation

In Stage III, the DERs and reactive power resources are optimally allocated within the clustered microgrids of the PDS using the capacity values obtained from Stage II, with the objective of minimizing system losses and improving voltage regulation. In this stage, the allocation is performed based on Case 2, where the main grid does not provide support and the microgrids operate in a decentralized cooperative manner to ensure smooth and reliable PDS operation.

Figure 5.7 illustrates the optimal locations of the DERs, including PV, wind, and BES units within each microgrid, in addition to the placement of reactive power resources. Table 5.3 summarizes the corresponding resource capacities and their associated PCS ratings. A clear pattern emerges in the optimal allocation results, where buses located at the beginning and end of distribution branches are frequently selected. This selection is primarily driven by the need to mitigate voltage drops that become more pronounced along longer feeder sections. By placing generation resources at these critical points, voltage profiles are effectively improved. Furthermore, reactive power resources are predominantly installed near the middle locations of PDS branches within each microgrid. This placement enables a more effective distribution of reactive power support, reducing line currents by compensating reactive components locally. Consequently, this leads to lower system losses and enhanced voltage regulation performance. In most allocation scenarios, BES units are installed either at the same bus as wind or PV generation units or at adjacent buses. This strategy facilitates direct charging from locally

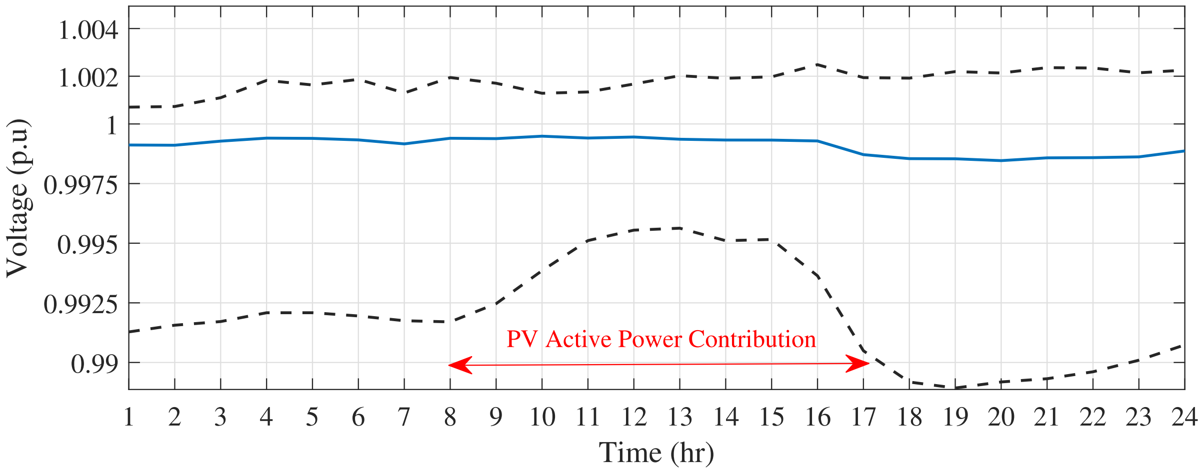


Figure 5.9: Bus voltage change over simulation period showing the maximum, minimum and mean voltage of the buses.

generated renewable power and minimizes additional transmission losses that would otherwise occur if energy were transferred across longer feeder distances.

Figure 5.8 illustrates the operating voltage range of the IEEE 30-bus system at each bus, demonstrating a clear improvement, with all voltage magnitudes maintained within $\pm 1\%$ of the nominal value. Buses located at the ends of feeders exhibit a wider voltage variation range, whereas buses equipped with installed DERs show enhanced voltage regulation due to their capability to provide localized voltage support through DERs. Buses 20–25 exhibit the highest variation range, primarily due to the presence of PV resources at the end of the feeder. During nighttime hours, when PV active power generation is unavailable, the reduced local support results in a larger voltage drop, causing the voltage magnitude to decrease to approximately 0.99 p.u. Nevertheless, this performance remains significantly improved compared to the case without DERs, where voltages at the end of feeders can drop to nearly 0.9 p.u.

This behavior is further confirmed by the time-series voltage analysis shown in Fig. 5.9, which presents the maximum, minimum, and mean voltage values across all buses. As indicated, the average voltage consistently remains close to 1 p.u. The minimum voltage profile reflects the contribution of PV generation, increasing during periods when PV output supports the PDS and clustered microgrids. Conversely, during high-demand periods with low solar irradiation (e.g., 17:00–21:00), the minimum voltage decreases, indicating relatively weaker voltage regulation. Despite these variations, the voltage across all scenarios remains within approximately 0.99–1.002 p.u., highlighting the effectiveness of the proposed framework in enhancing overall PDS

Table 5.3: Optimal DER and Reactive Power Resources Locations.

| Resource Type | Microgrid | Buses | Size (MW/MWh/MVar) | PCS (MW) |
|---|---|---|---|---|
| PV | 1 | [22, 25] | [0.93, 0.74] | [0.74, 0.36] |
| | 2 | [6] | [0.77] | [0.43] |
| | 3 | [12] | [0.56] | [0.27] |
| Wind | 1 | [2, 5] | [5.3, 2.59] | [1.17, 0.57] |
| | 2 | [8, 28] | [5.18, 8.21] | [0.85, 1.34] |
| | 3 | [15] | [3.7] | [0.81] |
| BES | 1 | [2, 5] | [69.7, 33.96] | [1.19, 0.66] |
| | 2 | [9, 31] | [40, 40.74] | [0.95, 0.97] |
| | 3 | [12] | [40.7] | [0.72] |
| $Q^{Var}$ | 1 | [4] | [0.9] | – |
| | 2 | [29, 7] | [0.55, 0.45] | – |
| | 3 | [11] | [1.1] | – |

voltage regulation under islanded yet collaboratively operated microgrids.

## 5.4 Chapter Summary

This chapter presented a comprehensive tri-stage optimization framework for coordinated microgrid clustering, optimal DER planning, and network-level resource allocation within PDSs. The first stage introduced an electrical-distance-based clustering approach that effectively partitions the PDS into coherent microgrids while preserving the inherent electrical structure of the network. The second stage formulated a stochastic capacity planning model that determines optimal DER sizing under multiple operational scenarios, capturing load and renewable uncertainties. The third stage allocated DERs and reactive power resources across the clustered PDS with the objective of minimizing system losses and improving voltage regulation.

The results demonstrated that operational strategies significantly influence the required generation and storage capacities. Independent islanded operation requires the highest installed capacity to ensure local reliability, whereas cooperative microgrid operation reduces generation requirements at the expense of increased storage flexibility. Full integration with the main grid leads to the most capacity-efficient configuration. Furthermore, the optimal allocation results confirmed that strategic placement of DERs and reactive power resources enhances voltage stability, reduces feeder losses, and maintains voltage magnitudes within tight operational limits, even under stochastic and islanded conditions.

While the proposed hierarchical clustering algorithm utilizes the default, static physical impedance of distribution lines to establish the fixed, resilient boundaries necessary for long-term microgrid capacity planning, active distribution networks also exhibit dynamic electrical coupling and frequently undergo topological reconfigurations due to fault isolation or routine switching. To advance Stage I of the framework, future work will explore adapting the clustering approach for short-term, operational microgrid formation by redefining the initial distance matrix. Instead of relying solely on an intact network's static line parameters, the distance metric could be dynamically updated to reflect post-fault impedance changes, or initialized using dynamic bus-to-bus sensitivity matrices, such as Jacobian-based voltage-to-power sensitivities, derived from real-time power flow states, or by analyzing historical locational marginal pricing correlations to group nodes with similar economic behaviors. This approach would allow the clustering framework to capture time-varying network stress, topological shifts, and market dynamics, complementing the long-term structural baseline established in this study. Furthermore, to build upon the optimal planning developed in Stage II, expanding the model to large-scale real distribution networks and considering market-based coordination mechanisms between microgrids and utility operators also represent promising research directions.

# Chapter 6

# Conclusions and Future Work

## 6.1 Contribution Summary

The global transition towards deep decarbonization and the widespread integration of renewable energy introduce unprecedented operational complexities within modern power systems. Managing these dynamics necessitates massive flexibility across both transmission and distribution networks, which can be achieved through ES and decentralized microgrid architectures. Despite the rapid advancement of these technologies, significant barriers remain in their effective integration into the power grid, including the complex modeling of emerging technologies, stringent market regulations, and the lack of electrically informed decentralization strategies.

This thesis presented comprehensive optimization frameworks designed to address these critical gaps by investigating operations across the transmission, consumer, and distribution levels. Specifically, the core contributions at each level are:

- **At the transmission level:** The research developed a holistic techno economic framework for the optimal sizing and multi horizon scheduling of grid connected AA-CAES. This approach incorporates detailed thermodynamic modeling to maximize the techno economic viability of multi service participation, specifically EA, OR, and CMDR, across diverse electricity pricing schemes.
- **At the consumer level:** An optimal energy resource sizing and management framework was introduced for LEFs participating in CMDR. This framework features a novel convex relaxation of dynamic baseline evaluation rules to overcome severe computational

complexities, reducing computation time from several hours to fractions of a second while ensuring global optimality with an optimality gap below 0.1%.

- **At the distribution level:** The study established a tri stage framework that systematically decentralizes PDSs into self sustaining microgrids. This was achieved through hierarchical agglomerative clustering based on electrical line impedance, followed by the stochastic planning and subsequent allocation strategy of DERs and reactive power resources to significantly enhance voltage regulation and reduce system losses.

## 6.2 Conclusion

The proposed frameworks provide robust, computationally tractable solutions to maximize the economic and operational benefits of ES and decentralized microgrids in modern power systems. The primary conclusions drawn from this research are as follows:

- **Optimal Deployment of AA-CAES:** Quantitative analysis demonstrates that the economic viability and optimal component sizing of AA-CAES heavily depend on the operational scheduling horizon and regional electricity pricing schemes. While AA-CAES is economically viable for EA and OR primarily in high-variability markets like Europe, it remains highly profitable for CMDR participation across both stable and variable markets. Crucially, the target market and service portfolio directly dictate the physical system sizing. In markets with high price variability, the optimization maximizes both compressor and turbine capacities to fully leverage price fluctuations for EA. Conversely, in stable-price markets such as Québec and Ontario, EA is financially infeasible; thus, the system optimally reduces the compressor size to minimize CapEx while simultaneously maximizing the turbine capacity to capitalize on CMDR compensation. Furthermore, participation in OR specifically drives an increase in turbine capacity to respond effectively to high-priced OR signals. Ultimately, the integration of detailed thermodynamic constraints ensures that these market-driven sizing and multi-horizon scheduling solutions remain technically feasible and economically optimal.

- **Optimal Sizing and Management of LEFs:** The introduction of a novel convex relaxation for dynamic CMDR baseline evaluation rules drastically improves computational tractability, reducing computation times from up to 17 hours to merely 0.11 seconds while ensuring global optimality with a gap below 0.1%. By anchoring evaluations to a standard baseline, this convex formulation eliminates the risk of artificial demand reduction and ensures participants can reliably meet their commitments. To evaluate physical asset deployment, the framework analyzed five specific case studies comparing short-term (BES), long-term (HES, CAES), and hybrid storage combinations, both with and without DR-enabled planning. The findings reveal that while standalone BES excels at short-term arbitrage, its high energy cost limits sustained DR provision. Conversely, HES and CAES effectively sustain extended DR reductions and peak shaving, but their lower round-trip efficiencies limit EA profitability. Consequently, the optimal aggregated configuration pairs BES with CAES, entirely displacing HES due to CAES's superior efficiency and lower costs. This hybrid synergy maximizes overall facility cost savings by utilizing BES for short-duration arbitrage and PV excess utilization, while relying on CAES to reliably deliver high-power CMDR commitments and mitigate facility peak loads.

- **Optimal Clustering and Planning of PDSs:** Decentralizing PDSs through the proposed tri-stage framework effectively bridges network topology with stochastic asset planning and spatial allocation. In the first stage, electrically informed, impedance-based hierarchical clustering successfully captures the true structural characteristics of the grid, partitioning it into coherent microgrids. In the second stage, stochastic planning evaluations reveal how distinct management strategies dictate physical capacity requirements. Specifically, operating microgrids as independent islanded entities demands the highest installed generation capacity to ensure local reliability. Conversely, enabling cooperative microgrid operation reduces total generation requirements but necessitates the highest storage capacities to buffer inter-microgrid energy exchanges. Ultimately, full integration with the main utility grid yields the most capacity-efficient configuration. Finally, the third stage's coordinated allocation strategy strategically places these optimized active DERs at the ends of distribution branches to effectively mitigate severe voltage drops, while positioning reactive power resources near the middle of feeders to minimize system losses. This integrated spatial and operational approach successfully maintains network voltage magnitudes within a strict operational range of 0.99 to 1.002 p.u., ensuring resilient performance regardless of the operational mode.

## 6.3 Limitations

While the optimization frameworks developed in this thesis provide robust and computationally tractable solutions for integrating ES and decentralized microgrids, certain limitations should be acknowledged:

- **Reliance on Historical Data:** The techno-economic framework for the optimal deployment of grid-connected AA-CAES and the energy resource sizing and management model for LEFs participating in CMDR rely fundamentally on historical data. Specifically, these models utilize historical load profiles, renewable generation data, and real-time hourly electricity prices to determine optimal component sizing and operational scheduling. This methodology inherently assumes that historical patterns are indicative of future behavior. Consequently, it does not explicitly account for projected exponential increases in electricity demand driven by deep sector electrification, nor does it capture potential unprecedented variations in future electricity market prices caused by an evolving and highly stochastic generation mix. As power grids continue to transform, these unmodeled future variations could impact the long-term techno-economic optimality of the determined capacities.
- **Static Network Modeling for Decentralization:** Regarding the decentralization of PDSs, the proposed hierarchical clustering algorithm utilizes the default, static physical impedance of distribution lines to establish the fixed, resilient boundaries necessary for long-term microgrid capacity planning. However, active distribution networks also exhibit dynamic electrical coupling and frequently undergo topological reconfigurations due to fault isolation or routine switching. The current framework establishes a long-term structural baseline but does not inherently capture short-term, time-varying network stresses or topological shifts.

## 6.4 Future Work

Building upon the methodologies and optimization frameworks developed in this thesis, several promising avenues for future research can be pursued:

- **Expansion of GS Portfolios:** For the techno economic framework regarding the optimal sizing and scheduling of grid connected AA-CAES, the current assumption limits participation to specific services like EA, OR, and CMDR. However, despite taking into consideration the most commonly used and influencing GSs, the framework can be extended to include and evaluate other GSs.

- **Integration of Emerging Storage Technologies:** For the optimal energy resource sizing and management framework for LEFs, the scope is currently limited by its reliance on specific modeled systems like BES, HES, and CAES. Because of this limitation, different ESs can also be added to the framework as new technologies are continuously developed.

- **Dynamic Clustering for Operational Microgrid Formation:** For the tri stage optimization framework for optimal clustering of power distribution systems into sustainable microgrids, to advance the first stage of the distribution network framework, future work will explore adapting the clustering approach for short-term, operational microgrid formation by redefining the initial distance matrix. Instead of relying solely on an intact network's static line parameters, the distance metric could be dynamically updated to reflect post-fault impedance changes. Alternatively, it could be initialized using dynamic bus-to-bus sensitivity matrices—such as Jacobian-based voltage-to-power sensitivities derived from real-time power flow states—or by analyzing historical locational marginal pricing correlations to group nodes with similar economic behaviors. This approach would allow the clustering framework to capture time-varying network stress, topological shifts, and market dynamics, complementing the long-term structural baseline established in this thesis.

- **Utility Scale Microgrid Management:** For the tri stage optimization framework for optimal clustering of power distribution systems into sustainable microgrids, the multi microgrid management approach can be utilized as a foundation for broader utility scale applications. By integrating market based coordination mechanisms between microgrids and utility operators, and expanding the model to large scale real distribution networks, this framework can be evolved to manage an entire utility grid consisting of interconnected microgrids.

# List of Publications

[1] Yahia N. Ahmed, Ahmed Abd Elaziz Elsayed, and Hany E. Farag, “Optimal Energy Resource Sizing of Large Load Facilities Participating in Capacity Markets Based Demand Response Considering Convex-Relaxed Market Constraints”, submitted for possible publication in IEEE Transactions on Energy Markets, Policy and Regulation

[2] Yahia N. Ahmed, Abdallah F. El-Hamalawy, and Hany E. Farag, “Optimal Deployment of Advanced Adiabatic Compressed Air Energy Storage for Ancillary Service Provision in Diverse Electricity Markets”, submitted for possible publication in Journal of Energy Storage

[3] Yahia N. Ahmed, Ahmed Abd Elaziz Elsayed, and Hany E. Farag, “Tri-stage Optimization Framework for Optimal Clustering of Power Distribution Systems Into Sustainable Microgrids”, in Energies

[4] Yahia N. Ahmed and Hany E. Farag, “Clustering-Based Stochastic Optimization of PV-Battery Sizing for Self-Sufficient Multi-Grid Systems”, IEEE Canada Electrical Power and Energy Conference (EPEC 2025), 15-17 October 2025, Waterloo, Ontario, Canada

# References


[1] International Energy Agency, "Global energy review 2025," IEA, Paris, Tech. Rep., 2025, licence: CC BY 4.0. [Online]. Available: https://www.iea.org/reports/global-energy-review-2025

[2] Ember, "Global electricity review 2025," Ember, Tech. Rep., April 2025, lead authors: Euan Graham and Nicolas Fulghum. Licence: CC BY-SA 4.0.

[3] International Energy Agency, "Electricity 2026," IEA, Paris, Tech. Rep., 2026, licence: CC BY 4.0. [Online]. Available: https://www.iea.org/reports/electricity-2026

[4] E. Ejuh Che, K. Roland Abeng, C. D. Iweh, G. J. Tsekouras, and A. Fopah-Lele, "The impact of integrating variable renewable energy sources into grid-connected power systems: Challenges, mitigation strategies, and prospects," *Energies*, vol. 18, no. 3, 2025. [Online]. Available: https://www.mdpi.com/1996-1073/18/3/689

[5] D. A. Elalfy, E. Gouda, M. F. Kotb, V. Bureš, and B. E. Sedhom, "Comprehensive review of energy storage systems technologies, objectives, challenges, and future trends," *Energy Strategy Reviews*, vol. 54, p. 101482, 2024. [Online]. Available: https://www.sciencedirect.com/science/article/pii/S2211467X24001895

[6] U.S. Department of Energy, "Grid energy storage," U.S. Department of Energy, Report, Dec. 2013.

[7] C. Opathella, A. Elkasrawy, A. A. Mohamed, and B. Venkatesh, "A novel capacity market model with energy storage," *IEEE Transactions on Smart Grid*, vol. 10, no. 5, pp. 5283–5293, 2019.

[8] J. J. Cuenca, M. Vanin, M. U. Hashmi, A. Koirala, H. Ergun, and B. P. Hayes, "Event-informed identification and allocation of distribution network planning candidates with influence scores and binary linear programming," *IEEE Transactions on Power Systems*, vol. 40, no. 1, pp. 492–504, 2025.

[9] K. H. Mohd Azmi, N. A. Mohamed Radzi, N. A. Azhar, F. S. Samidi, I. Thaqifah Zulkifli, and A. M. Zainal, "Active electric distribution network: Applications, challenges, and opportunities," *IEEE Access*, vol. 10, pp. 134 655–134 689, 2022.

[10] O. Aina, "Energy storage systems technologies, evolution and applications," *Energy and Power Engineering*, vol. 16, pp. 97–119, 2024. [Online]. Available: https://doi.org/10.4236/epe.2024.162005

[11] X. Zhang, S. P. Jenne, and J. Wang, "Dispatch of high-performance compressed air energy storage in distribution networks," in *2024 IEEE PES Innovative Smart Grid Technologies Europe (ISGT EUROPE)*, 2024, pp. 1–5.

[12] W. He, M. Dooner, M. King, D. Li, S. Guo, and J. Wang, "Techno-economic analysis of bulk-scale compressed air energy storage in power system decarbonisation," *Applied Energy*, vol. 282, p. 116097, 2021.

[13] Z. Tong, Z. Cheng, and S. Tong, "A review on the development of compressed air energy storage in china: Technical and economic challenges to commercialization," *Renewable and Sustainable Energy Reviews*, vol. 135, p. 110178, 2021.

[14] H. Khani, M. R. Dadash Zadeh, and A. H. Hajimiragha, "Transmission congestion relief using privately owned large-scale energy storage systems in a competitive electricity market," *IEEE Transactions on Power Systems*, vol. 31, no. 2, pp. 1449–1458, 2016.

[15] E. Drury, P. Denholm, and R. Sioshansi, "The value of compressed air energy storage in energy and reserve markets," *Energy*, vol. 36, no. 8, pp. 4959–4973, 2011.

[16] R. Khatami, K. Oikonomou, and M. Parvania, "Look-ahead optimal participation of compressed air energy storage in day-ahead and real-time markets," *IEEE Transactions on Sustainable Energy*, vol. 11, no. 2, pp. 682–692, 2020.

[17] J. Zhang, K.-J. Li, M. Wang, W.-J. Lee, and H. Gao, "A bi-level program for the planning of an islanded microgrid including caes," in *2015 IEEE Industry Applications Society Annual Meeting*, 2015, pp. 1–8.

[18] Y. Song, W. Wei, B. Wang, S. Huang, and S. Mei, "Real-time self-scheduling of jintan aa-caes plant in energy and reactive power markets," *Journal of Energy Storage*, vol. 89, p. 111622, 2024.

[19] Y. Li, S. Miao, B. Yin, J. Han, S. Zhang, J. Wang, and X. Luo, "Combined heat and power dispatch considering advanced adiabatic compressed air energy storage for wind power accommodation," *Energy Conversion and Management*, vol. 200, p. 112091, 2019.

[20] Z. Li, L. Chen, D. Liu, T. Zheng, B. Gao, and S. Mei, "Optimal capacity allocation of advanced adiabatic compressed air energy storage systems considering energy arbitrage," in *2019 Tsinghua International Doctoral Forum*, 2019, pp. 1–7.

[21] X. Zhang, S. P. Jenne, Y. Ding, J. Spencer, W. He, and J. Wang, "A wind power curtailment mitigation strategy via co-location and co-operation of compressed air energy storage with wind power generation," *Electric Power Systems Research*, vol. 241, p. 111318, 2025.

[22] J. Mouli-Castillo, M. Wilkinson, D. Mignard, C. McDermott, R. S. Haszeldine, and Z. K. Shipton, "Inter-seasonal compressed-air energy storage using saline aquifers," *Nature Energy*, vol. 4, no. 2, pp. 131–139, 2019.

[23] H. Kim, J. Rutqvist, D. Ryu, B. Choi, C. Sunwoo, and W.-K. Song, "Exploring the concept of compressed air energy storage (caes) in lined rock caverns at shallow depth: A modeling study of air tightness and energy balance," *Applied Energy*, vol. 92, no. 0, pp. 653–667, 2012.

[24] Y. Tian, T. Zhang, Z. Zhou, X. Zhang, Z. Wang, R. Chi, Z. Dong, Y. Lai, and X. Xue, "Comprehensive economic analysis of adiabatic compressed air energy storage system based on electricity spot market policy," *Journal of Energy Storage*, vol. 103, p. 114333, 2024.

[25] S. M. Azzam, T. Elshabrawy, and M. Ashour, "A bi-level framework for supply and demand side energy management in an islanded microgrid," *IEEE Trans. Ind. Inform.*, vol. 19, no. 1, pp. 220–231, 2023.

[26] New York Independent System Operator, "Nyiso 2024 annual report on demand response programs," 2024, accessed: 2025-12-04. [Online]. Available: https://www.nyiso.com/documents/20142/49931415/NYISO-2024-Annual-Report-on-Demand-Response-Programs.pdf

[27] Independent Electricity System Operator. (2024, Dec.) Ieso secures more megawatts at lower price in 2024 capacity auction. Accessed: 2025-12-04. [Online]. Available: https://www.ieso.ca/Sector-Participants/IESO-News/2024/12/IESO-Secures-More-Megawatts-at-Lower-Price-in-2024-Capacity-Auction

[28] IESO. (2025, Dec.) 2025-2027 electricity demand side management program plan released. Accessed: 2026-01-02. [Online]. Available: https://www.ieso.ca/Sector-Participants/IESO-News/2025/01/2025-2027-Electricity-Demand-Side-Management-Program-Plan-Released-0131

[29] R. Bhakar, S. Yamujala, A. Singh, and C. P. Barala, "Demand response obligations: A new regulatory tool," in *2024 IEEE Power Energy Society General Meeting (PESGM)*, 2024, pp. 1–5.

[30] M. Yu, S. H. Hong, and J. B. Kim, "Incentive-based demand response approach for aggregated demand side participation," in *2016 IEEE International Conference on Smart Grid Communications (SmartGridComm)*, 2016, pp. 51–56.

[31] X. He, N. Keyaerts, I. Azevedo, L. Meeus, L. Hancher, and J.-M. Glachant, "How to engage consumers in demand response: A contract perspective," *Util. Policy*, vol. 27, pp. 108–122, 2013.

[32] M. Vahedipour-Dahraie, H. Rashidizadeh-Kermani, M. Parente, M. Shafie-Khah, and P. Siano, "Investigating the impact of external demand response flexibility on the market power of strategic virtual power plant," *IEEE Access*, vol. 10, pp. 84 960–84 969, 2022.

[33] J. Ryu and J. Kim, "Virtual power plant operation strategy under uncertainty with demand response resources in electricity markets," *IEEE Access*, vol. 10, pp. 62 763–62 771, 2022.

[34] N. Alamir, S. Kamel, T. F. Megahed, M. Hori, and S. M. Abdelkader, "Developing hybrid demand response technique for energy management in microgrid based on pelican optimization algorithm," *Electr. Power Syst. Res.*, vol. 214, p. 108905, 2023.

[35] S. Parvizi, M. Montazeri, and H. Kebriaei, "Contract-based demand response mechanism for commercial and industrial customers," *IEEE Trans. Autom. Sci. Eng.*, vol. 22, pp. 3135–3146, 2025.

[36] H. Liang and J. Ma, "Data-driven resource planning for virtual power plant integrating demand response customer selection and storage," *IEEE Trans. Ind. Inform.*, vol. 18, no. 3, pp. 1833–1844, 2022.

[37] D. Liu, Z. Qin, H. Hua, Y. Ding, and J. Cao, "Incremental incentive mechanism design for diversified consumers in demand response," *Appl. Energy*, vol. 329, p. 120240, 2023.

[38] Independent Electricity System Operator. (2025) Capacity auction. Accessed: 2025-12-06. [Online]. Available: https://www.ieso.ca/en/Sector-Participants/Market-Operations/Markets-and-Related-Programs/Capacity-Auction

[39] New York Independent System Operator. (2025) Installed capacity market. Accessed: 2025-12-06. [Online]. Available: https://www.nyiso.com/installed-capacity-market

[40] California Independent System Operator. (2025) Demand response. Accessed: 2025-12-06. [Online]. Available: https://www.caiso.com/generation-transmission/load/demand-response

[41] D. Said, "A survey on information communication technologies in modern demand-side management for smart grids: Challenges, solutions, and opportunities," *IEEE Eng. Manag. Rev.*, vol. 51, no. 1, pp. 76–107, 2023.

[42] G. Kansal and R. Tiwari, "A comprehensive and preferential analysis of demand response programs considering demand uncertainty," *IEEE Trans. Ind. Appl.*, vol. 60, no. 4, pp. 5542–5551, 2024.

[43] Independent Electricity System Operator. (2025) Capacity auction enhancements. Accessed: 2025-12-04. [Online]. Available: https://www.ieso.ca/Sector-Participants/Engagement-Initiatives/Engagements/Capacity-Auction-Enhancements

[44] A. Emrani and A. Berrada, "A comprehensive review on techno-economic assessment of hybrid energy storage systems integrated with renewable energy," *J. Energy Storage*, vol. 84, p. 111010, 2024.

[45] N. A. Komba, C. Haisong, B. B. Liwoko, and G. C. Mwakipunda, "A comprehensive review on compressed air energy storage in geological formation: Experiments, simulations, and field applications," *Journal of Energy Storage*, vol. 114, p. 115795, 2025.

[46] B. N. Alhasnawi, B. H. Jasim, B. E. Sedhom, E. Hossain, and J. M. Guerrero, "A new decentralized control strategy of microgrids in the internet of energy paradigm," *Energies*, vol. 14, no. 8, p. 2183, 2021.

[47] C. A. Cortes, S. F. Contreras, and M. Shahidehpour, "Microgrid topology planning for enhancing the reliability of active distribution networks," *IEEE Transactions on Smart Grid*, vol. 9, no. 6, pp. 6369–6377, 2017.

[48] W. Yuan, J. Wang, F. Qiu, C. Chen, C. Kang, and B. Zeng, "Robust optimization-based resilient distribution network planning against natural disasters," *IEEE Transactions on Smart Grid*, vol. 7, no. 6, pp. 2817–2826, 2016.

[49] S. Habib, A. Ahmarinejad, and Y. Jia, “A stochastic model for microgrids planning considering smart prosumers, electric vehicles and energy storages,” *Journal of Energy Storage*, vol. 70, p. 107962, 2023.

[50] Y. Zhao, J. Lin, Y. Song, and Y. Xu, “A robust microgrid formation strategy for resilience enhancement of hydrogen penetrated active distribution networks,” *IEEE Transactions on Power Systems*, vol. 39, no. 2, pp. 2735–2748, 2023.

[51] K. Pang, C. Wang, N. D. Hatziargyriou, and F. Wen, “Microgrid formation and real-time scheduling of active distribution networks considering source-load stochasticity,” *IEEE Transactions on Power Systems*, vol. 39, no. 2, pp. 2801–2813, 2023.

[52] J. Ge, Y. Luo, J. Zhang, Y. Cao, and Z. Li, “A clustering algorithm based on intelligent distribution network,” in *2022 4th International Conference on Frontiers Technology of Information and Computer (ICFTIC)*, 2022, pp. 914–918.

[53] H. Zhang, W. Liu, S. Sun, P. Yu, and C. Cui, “Microgrid cluster division and optimal allocation method considering cooperative increment,” in *2023 International Conference on Power Energy Systems and Applications (ICoPESA)*, 2023, pp. 561–570.

[54] I. Jayawardene, P. Herath, and G. K. Venayagamoorthy, “A graph theory-based clustering method for power system networks,” in *2021 IEEE International Conference on Power Energy Systems and Applications (ICoPESA)*, 2021, pp. 1–6.

[55] Y. Chai, L. Guo, C. Wang, Z. Zhao, X. Du, and J. Pan, “Network partition and voltage coordination control for distribution networks with high penetration of distributed pv units,” *IEEE Transactions on Power Systems*, vol. PP, pp. 1–1, 03 2018.

[56] R. J. Sánchez-García, M. Fennelly, S. Norris, N. Wright, G. Niblo, J. Brodzki, and J. W. Bialek, “Hierarchical spectral clustering of power grids,” *IEEE Transactions on Power Systems*, vol. 29, no. 5, pp. 2229–2237, 2014.

[57] Y. N. Ahmed and E. Z. Hany Farag, “Clustering-based stochastic optimization of pv-battery sizing for self-sufficient multi-microgrid systems,” in *2025 IEEE Electrical Power and Energy Conference (EPEC)*, 2025, pp. 348–353.

[58] A. A. Khan, A. F. Minai, R. K. Pachauri, and H. Malik, “Optimal sizing, control, and management strategies for hybrid renewable energy systems: A comprehensive review,” *Energies*, vol. 15, no. 17, p. 6249, 2022.

[59] C. Gu, Y. Liu, J. Wang, Q. Li, and L. Wu, “Carbon-oriented planning of distributed generation and energy storage assets in power distribution network with hydrogen-based microgrids,” *IEEE Transactions on Sustainable Energy*, vol. 14, no. 2, pp. 790–802, 2022.

[60] E. G. Vera, C. A. Cañizares, M. Pirnia, T. P. Guedes, and J. D. M. Trujillo, “Two-stage stochastic optimization model for multi-microgrid planning,” *IEEE Transactions on Smart Grid*, vol. 14, no. 3, pp. 1723–1735, 2022.

[61] M. H. Atazadegan, E. Rokrok, and M. Doostizadeh, “A cooperative generation expansion planning of microgrids to improve the resiliency of active distribution networks,” *Ieee Access*, vol. 12, pp. 192 230–192 249, 2024.

[62] A. Maknouninejad and Z. Qu, "Realizing unified microgrid voltage profile and loss minimization: A cooperative distributed optimization and control approach," *IEEE Transactions on Smart Grid*, vol. 5, no. 4, pp. 1621–1630, 2014.

[63] X. Li and G. Jones, "Optimal sizing, location, and assignment of photovoltaic distributed generators with an energy storage system for islanded microgrids," *Energies*, vol. 15, no. 18, p. 6630, 2022.

[64] S. Koohi-Fayegh and M. Rosen, "A review of energy storage types, applications and recent developments," *Journal of Energy Storage*, vol. 27, p. 101047, 2020. [Online]. Available: https://www.sciencedirect.com/science/article/pii/S2352152X19306012

[65] B. Indrajith, K. Gunawardane, M. Alamgir Hossain, L. Li, R. Nicholson, and R. Zamora, "Hydrogen-integrated microgrids: A comprehensive review of hydrogen technologies and energy management strategies," *IEEE Access*, vol. 13, pp. 178 625–178 651, 2025.

[66] S. Rehman, L. M. Al-Hadhrami, and M. M. Alam, "Pumped hydro energy storage system: A technological review," *Renewable and Sustainable Energy Reviews*, vol. 44, pp. 586–598, 2015. [Online]. Available: https://www.sciencedirect.com/science/article/pii/S1364032115000106

[67] E. Barbour, I. G. Wilson, J. Radcliffe, Y. Ding, and Y. Li, "A review of pumped hydro energy storage development in significant international electricity markets," *Renewable and Sustainable Energy Reviews*, vol. 61, pp. 421–432, 2016. [Online]. Available: https://www.sciencedirect.com/science/article/pii/S1364032116300363

[68] M. Budt, D. Wolf, R. Span, and J. Yan, "A review on compressed air energy storage: Basic principles, past milestones and recent developments," *Applied Energy*, vol. 170, pp. 250–268, 2016. [Online]. Available: https://www.sciencedirect.com/science/article/pii/S0306261916302641

[69] G. Venkataramani, P. Parankusam, V. Ramalingam, and J. Wang, "A review on compressed air energy storage – a pathway for smart grid and polygeneration," *Renewable and Sustainable Energy Reviews*, vol. 62, pp. 895–907, 2016. [Online]. Available: https://www.sciencedirect.com/science/article/pii/S1364032116301125

[70] Q. Zhou, D. Du, C. Lu, Q. He, and W. Liu, "A review of thermal energy storage in compressed air energy storage system," *Energy*, vol. 188, p. 115993, 2019. [Online]. Available: https://www.sciencedirect.com/science/article/pii/S0360544219316871

[71] P. Roos and A. Haselbacher, "Analytical modeling of advanced adiabatic compressed air energy storage: Literature review and new models," *Renewable and Sustainable Energy Reviews*, vol. 163, p. 112464, 2022. [Online]. Available: https://www.sciencedirect.com/science/article/pii/S1364032122003690

[72] X. Zhang, Z. Gao, B. Zhou, H. Guo, Y. Xu, Y. Ding, and H. Chen, "Advanced compressed air energy storage systems: Fundamentals and applications," *Engineering*, vol. 34, pp. 246–269, 2024. [Online]. Available: https://www.sciencedirect.com/science/article/pii/S2095809924000559

[73] A. Abd Elaziz Elsayed, S. Saxena, and H. Essa Zidan Farag, "Optimal design of a planning and contracting framework to enable vehicle to building and grid services via demand response," *IEEE Trans. Transp. Electrif.*, vol. 11, no. 3, pp. 7542–7556, 2025.

[74] L. Pérez-Lombard, J. Ortiz, and C. Pout, "A review on buildings energy consumption information," *Energy and Buildings*, vol. 40, no. 3, pp. 394–398, 2008.

[75] A. Dubey and S. Santoso, "Electric vehicle charging on residential distribution systems: Impacts and mitigations," *IEEE Access*, vol. 3, pp. 1871–1893, 2015.

[76] K. Wang, Y. Huang, Y. Liu, T. Huang, and S. Zang, "A review of optimization scheduling for active distribution networks with high-penetration distributed generation access," *Energies*, vol. 18, no. 15, p. 4119, 2025.

[77] M. Abbasi, E. Abbasi, L. Li, R. P. Aguilera, D. Lu, and F. Wang, "Review on the microgrid concept, structures, components, communication systems, and control methods," *Energies*, vol. 16, no. 1, p. 484, 2023.

[78] A. A. Rathod and S. Balaji, "Modified harris hawks optimization for the 3E feasibility assessment of a hybrid renewable energy system," *Scientific Reports*, vol. 14, no. 1, p. 20127, 2024. [Online]. Available: https://doi.org/10.1038/s41598-024-70663-5

[79] T. K. Das and D. Kundu, "Feasibility and sensitivity analysis of a self-sustainable hybrid system: A case study of a mountainous region in bangladesh," *Energy Conversion and Management: X*, vol. 20, p. 100411, 2023. [Online]. Available: https://www.sciencedirect.com/science/article/pii/S2590174523000673

[80] X. Luo and W. Shi, "Optimal regulation of flexible loads in rural residential buildings considering mobile batteries: A case study in Shaanxi Province," *Building Simulation*, vol. 17, no. 7, pp. 1065–1083, 2024. [Online]. Available: https://doi.org/10.1007/s12273-024-1121-x

[81] F. Agha Kassab, R. Rodriguez, B. Celik, F. Locment, and M. Sechilariu, "A comprehensive review of sizing and energy management strategies for optimal planning of microgrids with pv and other renewable integration," *Applied Sciences*, vol. 14, no. 22, p. 10479, 2024.

[82] J. Qiao, Y. Mi, J. Shen, C. Lu, P. Cai, S. Ma, and P. Wang, "Optimization schedule strategy of active distribution network based on microgrid group and shared energy storage," *Applied Energy*, vol. 377, p. 124681, 2025.

[83] Z. Liang, C. Chung, Q. Wang, H. Chen, H. Yang, and C. Wu, "Fortifying renewable-dominant hybrid microgrids: A bi-directional converter based interconnection planning approach," *Engineering*, vol. 51, pp. 130–143, 2025. [Online]. Available: https://www.sciencedirect.com/science/article/pii/S2095809925001717

[84] Z. Han and S. Guo, "Investigation of operation strategy of combined cooling, heating and power (cchp) system based on advanced adiabatic compressed air energy storage," *Energy*, vol. 160, pp. 290–308, 2018.

[85] R. Jiang, F. G. F. Qin, B. Chen, X. Yang, H. Yin, and Y. Xu, "Thermodynamic performance analysis, assessment and comparison of an advanced trigenerative compressed air energy storage system under different operation strategies," *Energy*, vol. 186, p. 115862, 2019.

[86] N. M. Jubeh and Y. S. Najjar, "Green solution for power generation by adoption of adiabatic caes system," *Appl. Therm. Eng.*, vol. 44, pp. 85–89, 2012.

[87] IESO, "Markets and related programs," 2024, [Online]. Available: https://www.ieso.ca/Sector-Participants/Market-Operations/Markets-and-Related-Programs/Ancillary-Services-Market.

[88] M. Mersch, P. Sapin, A. V. Olympios, Y. Ding, N. Mac Dowell, and C. N. Markides, "A unified framework for the thermo-economic optimisation of compressed-air energy storage systems with solid and liquid thermal stores," *Energy Conversion and Management*, vol. 287, p. 117061, 2023.

[89] M. Mehrtash, F. Capitanescu, P. K. Heiselberg, T. Gibon, and A. Bertrand, "An enhanced optimal pv and battery sizing model for zero energy buildings considering environmental impacts," *IEEE Transactions on Industry Applications*, vol. 56, no. 6, pp. 6846–6856, 2020.

[90] A. F. El-Hamalawy, H. E. Z. Farag, and A. Asif, "Optimal design and technology selection for electrolyzer hydrogen plants considering hydrogen supply and provision of grid services," *IEEE Transactions on Sustainable Energy*, vol. 16, no. 4, pp. 2327–2343, 2025.

[91] S. Cevik and Y. Zhao, "Shocked: Electricity price volatility spillovers in europe," International Monetary Fund, IMF Working Paper WP/25/7, January 2025. [Online]. Available: https://www.imf.org/en/Publications/WP/Issues/2025/01/07/Shocked-Electricity-Price-Volatility-Spillovers-in-Europe-558963

[92] Hydro-Québec, "Electricity rates," PDF document, 2025, accessed: 2025-09-18, URL: https://www.hydroquebec.com/data/documents-donnees/pdf/electricity-rates.pdf.

[93] Independent Electricity System Operator (IESO), "Power Data," https://www.ieso.ca/en/Power-Data/, 2024.

[94] H. Khani, A. A. E. Elsayed, H. E. Z. Farag, and M. Mohamed, "Adaptive feasibility area estimation to enhance cybersecurity of electrolysis-based hydrogen refueling stations integrated with power distribution systems," *IEEE Transactions on Intelligent Transportation Systems*, pp. 1–17, 2025.

[95] François Raucent, "Europe Power Consumption," https://www.kaggle.com/datasets/francoisraucent/western-europe-power-consumption.

[96] A. F. El-Hamalawy, H. E. Farag, and A. Asif, "Optimal design of grid-connected green hydrogen plants considering electrolysis internal parameters and battery energy storage systems," *Energy Conversion and Management*, vol. 302, p. 118127, 2024. [Online]. Available: https://www.sciencedirect.com/science/article/pii/S0196890424000682